MULTI-BLOCK COMPUTATIONS AND TURBULENCE MODELING FOR TURBOMACHINERY FLOWS

By

JIAN LIU

A DISSERTATION PRESENTED TO THE GRADUATE SCHOOL OF
THE UNIVERSITY OF FLORIDA IN PARTIAL FULFILLMENT
OF THE REQUIREMENTS FOR THE DEGREE OF
DOCTOR OF PHILOSOPHY

UNIVERSITY OF FLORIDA

1996

ACKNOWLEDGEMENTS

I would like to express my deepest appreciation to my advisor, Professor Wei Shyy, for his advice, encouragement, friendship and constant support. I have benefitted substantially from his experience, knowledge and philosophy, both professionally and personally. Without his enthusiasm and commitment to this challenging project, my exploration in this work could not have been accomplished.

I would also like to sincerely thank my committee members, Professors Chen-Chi Hsu, Ulrich H. Kurzweg, Bernard M. Leadon and Kermit N. Sigmon for their teaching, support and encouragement throughout my time at the University of Florida.

Very special thanks are given to all my colleagues in the CFD group, especially, Jeffrey Wright, Madhukar Rao, S.S. Thakur, Richard Smith, H.S. Udaykumar, Venkata Krishnamurty, Shin-Jye Liang, and Edwin Blosch, for their direct and indirect contributions I am grateful and for their genuine friendship I enjoy. I would also like to thank my colleagues Guobao Guo and Guang-Wu Chen for their help in many aspects.

Last but not least, I am deeply indebted to my wife, Jie, for her understanding, encouragement and support in both my academic pursuits and life in general.

TABLE OF CONTENTS

pages

ACKNOWLEDGEMENTS ii

ABSTRACT vi

CHAPTERS

1 INTRODUCTION 1

2 PRESSURE-BASED METHOD FOR THE NAVIER-STOKES EQUATIONS 5

2.1 Governing Equations 5
2.2 Discretization of the Momentum Equations 6
2.2.1 First-Order Upwind Scheme 9
2.2.2 Central Difference Scheme 10
2.2.3 Second-Order Upwind Scheme 11
2.3 Discretization of the Pressure Correction Equation 12
2.4 Physical Boundary Conditions 14
2.4.1 Boundary Conditions for the Momentum Equations 14
2.4.2 Boundary Conditions for the Pressure Correction Equation ... 15
2.5 The Solution Procedure 16
2.6 Concluding Remarks 17

3 MULTI-BLOCK METHOD FOR THE NAVIER-STOKES EQUATIONS 18

3.1 Background 18
3.2 Notation of Multi-Block Grids 21
3.3 Analysis of Model Equations 21
3.3.1 1-D Poisson Equation 21
3.3.2 2-D Poisson Equation 25
3.3.3 1-D Convection-Diffusion Equation 27
3.4 Analysis of the Naiver-Stokes Equations 28
3.5 Multi-Block Interface Treatments for the Navier-Stokes Equations .. 30
3.5.1 Multi-Block Grid Arrangement 30
3.5.2 Interface Treatment for the Momentum Equations 31

3.5.3 Interface Treatment for the Pressure Correction Equation 34
3.5.4 Interface Treatment for Mass Flux 39
3.6 Solution Methods 42
3.7 Solution Strategy for the Navier-Stokes Equations on Multi-Block Grids 43
3.7.1 Solution Procedure for Single Block Computations 43
3.7.2 Solution Procedure for Multi-Block Computations 44
3.7.3 Convergence Criterion 45
3.8 Concluding Remarks 46

4 DATA STRUCTURES 48

4.1 General Interface Organization 48
4.2 Interpolation 48
4.2.1 Grid Vertex Based Interpolation 49
4.2.2 Grid Face Center Based Interpolation 52
4.3 Interpolation with Local Conservative Correction 54
4.3.1 Grid Cell Split 55
4.3.2 Flux Interpolation 58
4.3.3 Local Flux Correction 59
4.4 Concluding Remarks 61

5 ASSESSMENT OF THE INTERFACE TREATMENTS 63

5.1 Assessments of Conservative Treatments in the N-N Boundary Condition for the Pressure Correction Equation 63
5.2 Comparison of Two Different Interface Conditions for the Pressure Correction Equation 75
5.3 Simulations of the Hydraulic Turbine Distributor Flows 79
5.3.1 Case A: 5 Blades 79
5.3.2 Case B: 4 Blades 81
5.4 Concluding Remarks 85

6 TWO-EQUATION TURBULENCE MODELING WITH NON-EQUILIBRIUM EFFECT 88

6.1 Background 88
6.2 Turbulent Transport Equations 92
6.2.1 Reynolds-Stress Transport Equation 92
6.2.2 K-ε Transport Equations 93
6.3 Implementation of the K-ε Model for 2-D Flow 95
6.3.1 Boundary Conditions and Wall Treatment 96

6.3.2 Implementation of the Wall Shear Stress in Momentum Equations 99
6.3.3 Implementation of the K-ε Equations near Wall Boundaries ... 102
6.4 Turbulence Modeling for Non-Equilibrium Flows 104
6.5 Case Studies 107
6.5.1 Backward Facing Step Flow 107
6.5.2 Hill Flow Inside a Channel 111
6.5.3 3-D Diffuser Flow 121
6.6 Concluding Remarks 122

7 TWO-EQUATION TURBULENCE MODELING WITH ROTATIONAL EFFECT 129

7.1 Background 129
7.2 The Momentum and Turbulent Transport Equations 131
7.3 Theoretical Analyses 134
7.3.1 Displaced Particle Analysis 134
7.3.2 Simplified Reynolds-Stress Analysis 137
7.4 The Model with Rotational Effect 140
7.5 Assessment of the Modified Model 142
7.5.1 Rotating Channel Flow 142
7.5.2 Rotating Backward Facing Step Flow 147
7.5.3 Flow Simulation in A Torque Converter 162
7.6 Concluding Remarks 164

8 SUMMARY AND SUGGESTIONS FOR FUTURE WORK 168

REFERENCE 171

BIOGRAPHICAL SKETCH 178

Abstract of Dissertation Presented to the Graduate School
of the University of Florida in Partial Fulfillment of the
Requirements for the Degree of Doctor of Philosophy

MULTI-BLOCK COMPUTATIONS AND TURBULENCE MODELING
FOR TURBOMACHINERY FLOWS

By

Jian Liu

May 1996

Chairperson: Wei Shyy
Major Department: Aerospace Engineering, Mechanics and Engineering Science

Turbomachinery flows are encountered in many industrial devices. To successfully analyze the flow behavior, both numerical treatments regarding gridding techniques in complex geometries, and physical modeling regarding rotating turbulence closures, need to be developed. In this work, a pressure-based multi-block grid method for solving incompressible viscous flows in complex geometries is presented. The method employs a finite volume approach and a staggered grid, and solves the governing equations in a sequential manner. Issues regarding discontinuous grid interface treatment for solving the Navier-Stokes equations in multi-block domain are investigated. For the momentum equations, the dependent variables between blocks can be directly interpolated. For the pressure correction equation, it is found that with the local conservative interface mass flux treatment with certain degree of accuracy, both the Neumann-Neumann and Neumann-Dirichlet boundary conditions can yield satisfactory solutions.

The closure issues of the K-ε two-equation turbulence model are discussed. Specifically, the original and non-equilibrium K-ε models are compared. It is observed that the equilibrium condition between production and dissipation of the turbulent kinetic energy, which is the basis of the original K-ε model, is not satisfied in general. The non-equilibrium K-ε model, where the ε-equation is modified to account for the imbalance between the production and dissipation terms, in essence introduces an extra time scale in the model, and appears to produce better predictions for complex flows.

The K-ε turbulence model with rotational effect is also investigated. The analysis shows that in the context of the K- and ε-equations, the rotation affects the turbulent quantities only indirectly through the Reynolds-stress terms. This indirect rotational effect is not accounted for, in the original K-ε model. The analysis also clearly identifies the effect of the system rotation interacting with structure of turbulence and the primary nondimensional parameter. The rotational effect is modeled through the modification of the source term in the ε-equation. The numerical and modeling techniques are used to solve two- and three-dimensional turbomachinery flow problems.

CHAPTER 1
INTRODUCTION

With the rapid advance of numerical methods and computer technologies, computational fluid dynamics (CFD) is becoming an important tool in analyzing fluid physics and in engineering design. However, for many flow problems involving complex physics and geometries, such as turbomachinery flows, grid generation becomes a major issue. Basically two different approaches have been developed: (1) unstructured grid, and (2) multi-block structured grid. Each of two methods has its advantages and disadvantages.

With unstructured grids, the flow domain is typically discretized with an array of grid cells which have an irregular connectivity. Usually the grid is composed of a single cell type, typically either triangular or quadrilateral (in two dimensions) and tetrahedral (in three dimensions). Unstructured grids are very flexible in discretizing complex geometries. With the development of computational geometry and data structure, discretization of even the most complex geometries can be handled in an efficient way (Löhner and Parikh 1988, Morgan et al. 1991, Braaten and Connell 1996, Kallinderis et al. 1996). In addition, unstructured grids are well suited for solution adaptive methods involving local grid refinement without introducing grid discontinuity. However, unstructured grids have some disadvantages. In terms of computer memory and computational efficiency, due to the lack of inherent order of grid nodes, the flow solvers with unstructured grids may occupy more computer memory compared to the solvers with structured grids. The same problem also makes it difficult for the flow solver to be efficiently paralleled to enhance the computational efficiency. Regarding solution accuracy, unstructured grid methods pose another challenge for flow problems containing thin layers, such as boundary layers. The ability to accurately control the aspect ratio and directionality of the grid cells, without increasing too many grid

cells, need to be resolved before unstructured grids can be efficiently used to solve practical viscous flow problems.

On the other hand, structured grids, which have the usual ordering of the grid cells, generally require less computer memory and can employ linear equation solver efficiently. Structured grids can also better accommodate directional preference such as thin layers. For complex flows, it is often difficult to generate a satisfactory, single structured grid to cover the entire flow domain. In addition, for problems of multiple length scales, a single structured grid has difficulties to resolve all flow features with a reasonable number of grid points. All these make the multi-block structured grid very attractive. The multi-block structured grid can alleviate those difficulties because (1) it can reduce the topological complexity of a single structured grid system by employing several blocks of grid, permitting each individual grid block to be generated independently so that both geometry and resolution in the boundary region can be treated more satisfactorily; (2) grid lines need not to be continuous across grid interfaces, and local grid refinement and adaptive redistribution can be conducted more easily to accommodate different physical length scales present in different regions (Rai 1984, Chesshire and Henshaw 1990); (3) the multi-block method, in the spirit of divide-conquer, also provides a natural route for parallel computations (Gropp and Keyes 1992a, 1992b).

In the multi-block method, because the grid lines may not be continuous across grid block interfaces, information between blocks has to be transferred with due care. Such an information transfer method is preferably easy to implement, while maintaining necessary accuracy and computational efficiency. A major related issue is that, for many flow problems, it is often important to use conservative interface procedure to ensure that physical conservation laws are satisfied (Berger 1987, Kallinderis 1992, Chesshire and Henshaw. 1994). Such a consideration can impose stringent constraints on the construction of an effective interface scheme; furthermore, in some cases, the above needs can conflict one another. Simultaneous achievement of both conservation and accuracy can be difficult.

In the present study, a methodology for solving incompressible viscous flows with multi-block structured grid in the framework of a pressure-based method is explored. In Chapter 2, a pressure-based method for solving two-dimensional incompressible Navier-Stokes equations in non-orthogonal curvilinear grid is summarized. The issues of the interface treatment in the multi-block method are investigated in Chapter 3. Specifically, the effects of non-conservative and conservative treatments for mass flux on solution accuracy are studied. Different ways to couple pressure fields between adjacent blocks and different iterative strategies between blocks are discussed. In Chapter 4, data structures associated with grid interface treatment are detailed. Assessments are made of the accuracy and effectiveness of these interface schemes. The applications of the multi-block method are demonstrated through the turbulent flows around hydraulic turbine distributors involving cascades of multiple airfoils. These numerical results are presented in Chapter 5.

Besides numerical discretization schemes and complex geometries, the treatment of turbulent flows is another issue of much practical importance to the success of CFD. Over the last several decades, various turbulent models have been developed and applied to many flow problems with varied degrees of success. These models range from the simplest and least expensive algebraic models to the seven-equation Reynolds-stress models, which include six equations for the Reynolds-stress components and one equation for the dissipation rate of the turbulence kinetic energy. Among them, the two-equation models have been most popular in complex engineering flow computations. The most popular two-equation models is the K-ε model (Launder and Spalding 1974).

However, the two-equation models are derived based on certain assumptions under some specific flow conditions. One of them is assuming that the production and the dissipation rate of the turbulent kinetic energy is under equilibrium condition. While this is satisfactory for some simple flows, for complex flows including flow recirculation, streamline curvature, adverse pressure gradient, etc., the equilibrium condition does not exist, and the original two-equation models cannot give satisfactory results (Chen and Kim,

1987, Yakhot et al. 1992). Therefore, there is a clear need for better two-equation models for complex turbulent flows in which the equilibrium condition is not satisfied. In Chapter 6, the K-ε model under the non-equilibrium condition will be explored with modifications proposed and assessed.

For turbomachinery flows, the effect of system rotation can substantially impact the flow structure (Johnston et al.1972). However, the original K-ε model (Launder and Spalding 1974) does not respond to the rotational effect (Howard et al. 1980, Shimemura 1993). In Chapter 7, this problem will be tackled within the context of the K-ε model. Detailed physical analyses and modeling process will be presented. Several numerical tests and applications to the turbomachinery flows will be conducted and demonstrated.

CHAPTER 2
PRESSURE-BASED METHOD FOR THE NAVIER-STOKES EQUATIONS

In this chapter, the pressure-based method for solving incompressible viscous flows in non-orthogonal curvilinear coordinate is presented. Basically, the method employs a control volume approach and uses a staggered grid for the velocity components and the pressure, in order to avoid a checkerboard pressure distribution. The algorithm solves the governing equations in a sequential manner. The velocity components are computed from the respective momentum equations. The pressure correction is solved by the pressure correction equation which is formed by manipulating the continuity equation and the momentum equations. Then, the velocity components and pressure are corrected by the pressure correction. The whole process is repeated until the desired convergence criterion is reached. In the following, the governing equations and the corresponding transformed equations are first introduced. Several common used convection schemes for the momentum equation are presented. Then, the derivation of the pressure correction equations is given. Finally, the boundary conditions and the solution procedure are discussed.

2.1 Governing Equations

The governing equations adopted in this study are the two-dimensional steady state, incompressible, constant property, Navier-Stokes equations along with the corresponding form of the continuity equation:

$$\frac{\partial}{\partial x}(\varrho u) + \frac{\partial}{\partial y}(\varrho v) = 0 \tag{2.1}$$

$$\frac{\partial}{\partial x}(\varrho uu) + \frac{\partial}{\partial y}(\varrho vu) = -\frac{\partial p}{\partial x} + \frac{\partial}{\partial x}(\mu \frac{\partial u}{\partial x}) + \frac{\partial}{\partial y}(\mu \frac{\partial u}{\partial y}) \tag{2.2}$$

$$\frac{\partial}{\partial x}(\varrho uv) + \frac{\partial}{\partial y}(\varrho vv) = -\frac{\partial p}{\partial y} + \frac{\partial}{\partial x}(\mu\frac{\partial v}{\partial x}) + \frac{\partial}{\partial y}(\mu\frac{\partial v}{\partial y}) \quad (2.3)$$

With the introduction of coordinate transformation $\xi = \xi(x, y), \eta = \eta(x, y)$, the equations above are cast in the curvilinear coordinates (Shyy 1994),

$$\frac{\partial}{\partial \xi}(\varrho U) + \frac{\partial}{\partial \eta}(\varrho V) = 0 \quad (2.4)$$

$$\frac{\partial}{\partial \xi}(\varrho Uu) + \frac{\partial}{\partial \eta}(\varrho Vu) = -y_\eta\frac{\partial p}{\partial \xi} + y_\xi\frac{\partial p}{\partial \eta} + \frac{\partial}{\partial \xi}[\frac{\mu}{J}(q_1u_\xi - q_2u_\eta)] + \frac{\partial}{\partial \eta}[\frac{\mu}{J}(-q_2u_\xi + q_3u_\eta)]$$

(2.5)

$$\frac{\partial}{\partial \xi}(\varrho Uv) + \frac{\partial}{\partial \eta}(\varrho Vv) = +x_\eta\frac{\partial p}{\partial \xi} - x_\xi\frac{\partial p}{\partial \eta} + \frac{\partial}{\partial \xi}[\frac{\mu}{J}(q_1v_\xi - q_2v_\eta)] + \frac{\partial}{\partial \eta}[\frac{\mu}{J}(-q_2v_\xi + q_3v_\eta)]$$

(2.6)

where the contravariant velocity components are given by:

$$U = uy_\eta - vx_\eta \quad (2.7)$$

$$V = vx_\xi - uy_\xi \quad (2.8)$$

J (the Jacobian of the transformation), q_1, q_2 and q_3 are given by the following

$$q_1 = x_\eta^2 + y_\eta^2 \quad (2.9)$$

$$q_2 = x_\xi x_\eta + y_\xi y_\eta \quad (2.10)$$

$$q_3 = x_\xi^2 + y_\xi^2 \quad (2.11)$$

$$J = x_\xi y_\eta - x_\eta y_\xi \quad (2.12)$$

2.2 Discretization of the Momentum Equations

A staggered grid system is adopted, as shown in Fig. 2.1. The scalar variables are located at the center of the four adjacent grid points. Both u and U are located at the midpoint of the east and west faces of the control volume. Both v and V are located at the midpoint

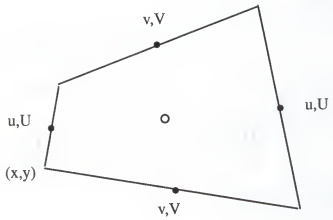

(i) Configuration of a staggered grid system

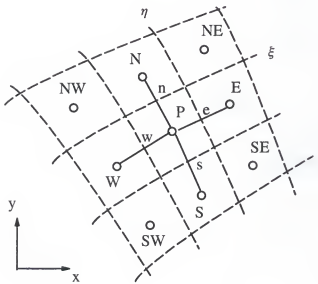

(ii) Curvilinear grid system

Fig. 2.1 Staggered grid and notation for curvilinear grid system

of the north and south faces of the control volume. In terms of the notation shown in Fig. 2.1, for a node P enclosed in its cell and surrounded by its neighbors N, S, E and W, the finite difference approximation to the conservation law can be performed by taking the integral of the momentum equations over the control volume. By arbitrarily taking $\Delta\xi = \Delta\eta = 1$, the resulting u- and v- momentum equations yield

$$[\varrho Uu + y_\eta p - \frac{\mu}{J}(q_1 u_\xi - q_2 u_\eta)]\Big|_w^e + [\varrho Vu - y_\xi p - \frac{\mu}{J}(-q_2 u_\xi + q_3 u_\eta)]\Big|_s^n = 0 \tag{2.13}$$

$$[\varrho Uv - x_\eta p - \frac{\mu}{J}(q_1 v_\xi - q_2 v_\eta)]\Big|_w^e + [\varrho Vv + x_\xi p - \frac{\mu}{J}(-q_2 v_\xi + q_3 v_\eta)]\Big|_s^n = 0 \tag{2.14}$$

The equations above can be put into a general difference form

$$[\varrho U\phi - \frac{\mu}{J}(q_1\phi_\xi - q_2\phi_\eta)]\Big|_w^e + [\varrho V\phi - \frac{\mu}{J}(-q_2 u_\xi + q_3\phi_\eta)]\Big|_s^n = S \cdot J \tag{2.15}$$

where ϕ is the general dependent variable and S is the source term. With appropriate finite difference schemes representing the convective and diffusive terms at the control volume boundaries, the discretized equation relating the variable at a central point P and its neighboring values is obtained (Shyy et al. 1985),

$$A_P\phi_P = A_E\phi_E + A_W\phi_W + A_S\phi_S + A_N\phi_N + S_v \tag{2.16}$$

where A's are the coefficients resulting from the numerical schemes chosen in the course of discretization. The pressure terms and the cross-derivative portion of the viscous terms due to the non-orthogonal grid are treated as source term here in S_v. The diffusion terms and the pressure terms are discretized using the standard second order central difference schemes, whereas the convection terms are discretized using one of the several convection schemes discussed in the next section. The discretization stencil for the convection schemes are shown in Fig. (2.2).

2.2.1 First-Order Upwind Scheme

For the first-order upwind scheme, the value of ϕ at any control volume interface is estimated using the value at the upwind neighbor. Thus, as is well known, the value ϕ_e at the east face is assigned the value ϕ_P if the flux F_e is positive, and the value ϕ_E if the flux F_e is negative. Here, the Flux F is defined as

$$F_{e,w} = (\varrho U)_{e,w} \tag{2.17}$$

$$F_{n,s} = (\varrho V)_{n,s} \tag{2.18}$$

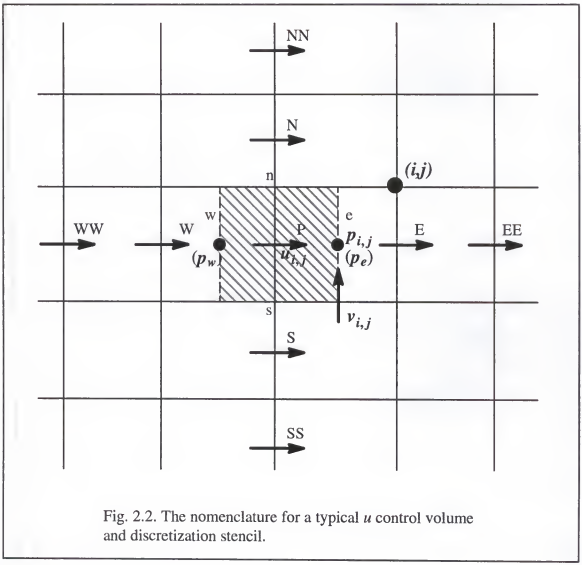

Fig. 2.2. The nomenclature for a typical u control volume and discretization stencil.

This choice of extrapolation amounts to a piecewise constant profile, with no variation allowed between the values of ϕ at two adjacent nodes along the one dimensional convection field. The convective flux on the east face can be conveniently written as

$$F_e\phi_e = \phi_P[\![F_e, 0]\!] - \phi_E[\![-F_e, 0]\!] \tag{2.19}$$

For the first-order upwind scheme, after subtracting the continuity equation multiplied by ϕ_P from the momentum equation given by Eqs. (2.2) or (2.3), we get

$$\begin{aligned} A_E &= D_e + [\![-F_e, 0]\!] \\ A_W &= D_w + [\![F_w, 0]\!] \\ A_N &= D_n + [\![-F_n, 0]\!] \\ A_S &= D_s + [\![F_s, 0]\!] \\ A_P &= A_E + A_W + A_N + A_S \end{aligned} \tag{2.20}$$

and $S=0$. Here, the operator $[\![p,q]\!]$ denotes the maximum of p and q. The diffusion coefficients is defined as

$$D_{e,w} = \left(\frac{\mu}{J}q_1\right)_{e,w} \tag{2.21}$$

$$D_{n,s} = \left(\frac{\mu}{J}q_1\right)_{n,s} \tag{2.22}$$

2.2.2 Central Difference Scheme

For the central difference scheme, ϕ at any interface is estimated by a linear interpolation between the two grid point neighbors on either side of the interface, regardless of the direction of local convection; for example

$$F_e\phi_e = F_e\frac{1}{2}(\phi_P + \phi_E) \tag{2.23}$$

The coefficients in Eq. (2.16), after subtracting the continuity equation multiplied by ϕ_P from the momentum equation, become

$$A_E = D_e - \frac{F_e}{2}$$

$$A_W = D_w + \frac{F_w}{2}$$

$$A_N = D_n - \frac{F_n}{2} \tag{2.24}$$

$$A_S = D_s + \frac{F_s}{2}$$

$$A_P = A_E + A_W + A_N + A_S$$

and $S=0$.

2.2.3 Second-Order Upwind Scheme

In this case, we estimate ϕ at any interface by a linear extrapolation of the ϕ values at two upwind neighbors. Thus, for example, depending on the sign of F_e, we estimate ϕ_e as

$$\phi_e = \frac{3}{2}\phi_P - \frac{1}{2}\phi_W \quad , \quad \text{if } F_e > 0 \ , \tag{2.25}$$

$$\phi_e = \frac{3}{2}\phi_E - \frac{1}{2}\phi_{EE} \quad , \quad \text{if } F_e < 0 \ . \tag{2.26}$$

The convective flux can thus be written as

$$F_e\phi_e = \left(\frac{3}{2}\phi_P - \frac{1}{2}\phi_W\right) [\![F_e, 0]\!] - \left(\frac{3}{2}\phi_E - \frac{1}{2}\phi_{EE}\right) [\![-F_e, 0]\!] \tag{2.27}$$

Many alternatives can be devised to implement the second-order upwind scheme into the standard notation typified by Eq. (2.16). A deferred correction approach is used here. The first-order upwind scheme is taken as the "basis" and the difference between the two schemes is assigned to the source term S, which is treated explicitly. One merit of such a treatment is that it maintains diagonal dominance in the course of the iterative updating.

As mentioned above, we write the total flux for the second-order upwind scheme as the flux for the first-order upwind scheme with the additional terms going into the source term S:

$$F_e u_e = \left[u_P + \frac{1}{2}(u_P - u_W)\right][\![F_e, 0]\!] - \left[u_E + \frac{1}{2}(u_E - u_{EE})\right][\![-F_e, 0]\!] \tag{2.28}$$

Similar to the first-order upwind and second-order central difference schemes, we subtract the continuity equation multiplied by ϕ_P. Thus, all the coefficients are the same as that for the first-order upwind scheme, i.e., those given by Eq. (2.20). However, we now have the following form for the source term S:

$$\begin{aligned} S = & -\frac{1}{2}(\phi_P - \phi_W)[\![F_e, 0]\!] + \frac{1}{2}(\phi_E - \phi_{EE})[\![-F_e, 0]\!] \\ & + \frac{1}{2}(\phi_W - \phi_{WW})[\![F_w, 0]\!] - \frac{1}{2}(\phi_P - \phi_E)[\![-F_w, 0]\!] \\ & - \frac{1}{2}(\phi_P - \phi_S)[\![F_n, 0]\!] + \frac{1}{2}(\phi_N - \phi_{NN})[\![-F_n, 0]\!] \\ & + \frac{1}{2}(\phi_S - \phi_{SS})[\![F_s, 0]\!] - \frac{1}{2}(\phi_P - \phi_N)[\![-F_s, 0]\!] \end{aligned} \tag{2.29}$$

2.3 Discretization of the Pressure Correction Equation

The continuity equation can be written in a discretized form over each control volume as following

$$(y_\eta \rho u - x_\eta \rho v)_e - (y_\eta \rho u - x_\eta \rho v)_w + (-y_\xi \rho u + x_\xi \rho v)_n - (-y_\xi \rho u + x_\xi \rho v)_s = 0 \tag{2.30}$$

It is assumed that u^* and v^* are the velocity components that satisfy the momentum equations with a given distribution p^*. Since u^* and v^* in general will not satisfy the mass continuity equation, the pressure p^* must be corrected. In the SIMPLE procedure (Patankar 1980), the corrected pressure is obtained from

$$p = p^* + p' \tag{2.31}$$

where p' is called the pressure correction. The corresponding velocity corrections u' and v' can be introduced in a similar way

$$u = u^* + u' , \quad v = v^* + v' \tag{2.32}$$

To derive the pressure correction equation, it is assumed that u^* and v^* are obtained from the momentum equations as follows

$$u_P^* = \sum_{i=E,W,N,S} \frac{A_i^u}{A_P^u} u_i^* + D^u + (B^u p_\xi^* + C^u p_\eta^*) \tag{2.33}$$

$$v_P^* = \sum_{i=E,W,N,S} \frac{A_i^v}{A_P^v} v_i^* + D^v + (B^v p_\xi^* + C^v p_\eta^*) \tag{2.34}$$

where D^u and D^v are the cross-derivative viscous terms in the u- and v- equations, respectively, and,

$$\begin{aligned} B^u &= -\frac{y_\eta}{A_P^u} , \quad C^u = \frac{y_\xi}{A_P^u} \\ B^v &= \frac{x_\eta}{A_P^v} , \quad C^v = -\frac{x_\xi}{A_P^v} \end{aligned} \tag{2.35}$$

The velocity components are assumed to be corrected by the following formulas

$$u = u^* + (B^u p_\xi' + C^u p_\eta') \tag{2.36}$$

$$v = v^* + (B^v p_\xi' + C^v p_\eta') \tag{2.37}$$

Subsequently, the corresponding correction forms for U and V are obtained by substituting Eqs. (2.36–2.37) into Eq. (2.7–2.8)

$$U = U^* + (B^u y_\eta - B^v x_\eta) p_\xi' + (C^u y_\eta - C^v x_\eta) p_\eta' \tag{2.38}$$

$$V = V^* + (B^v x_\xi - B^u y_\xi) p_\xi' + (C^v x_\xi - C^u y_\xi) p_\eta' \tag{2.39}$$

where U^* and V^* are calculated based on u^* and v^*. It is noted that the continuity equation, Eq. (2.30), can be written in the following finite difference form

$$(\varrho U)_e - (\varrho U)_w + (\varrho V)_n - (\varrho V)_s = 0 \tag{2.40}$$

To retain a five points approximation in the pressure correction equation, the p'_η term in Eq. (2.38) and the p'_ξ term in Eq. (2.39) are dropped, leading to the following simplified correction equations for U and V

$$U = U^* + (B^u y_\eta - B^v x_\eta) p'_\xi \tag{2.41}$$

$$V = V^* + (C^v x_\xi - C^u y_\xi) p'_\eta \tag{2.42}$$

These equations are then substituted into Eq. (2.40) to obtain the following pressure correction equation

$$a_P p'_P = a_E p'_E + a_W p'_W + a_N p'_N + a_S p'_S + S_P \tag{2.43}$$

$$a_P = a_E + a_W + a_N + a_S \tag{2.44}$$

$$S_P = (\varrho U^*)_w - (\varrho U^*)_e + (\varrho V^*)_s - (\varrho V^*)_n \tag{2.45}$$

with the coefficients given by

$$a_E = \varrho \left(\frac{y_\eta^2}{A_P^u} + \frac{x_\eta^2}{A_P^v} \right)_e \tag{2.46}$$

$$a_W = \varrho \left(\frac{y_\eta^2}{A_P^u} + \frac{x_\eta^2}{A_P^v} \right)_w \tag{2.47}$$

$$a_N = \varrho \left[\frac{x_\xi^2}{A_P^v} + \frac{y_\xi^2}{A_P^u} \right]_n \tag{2.48}$$

$$a_S = \varrho \left[\frac{x_\xi^2}{A_P^v} + \frac{y_\xi^2}{A_P^u} \right]_s \tag{2.49}$$

2.4 Physical Boundary Conditions

2.4.1 Boundary Conditions for the Momentum Equations

At solid walls, the non-slip condition is applied, i.e., the fluid velocity at a solid wall is the same as the wall velocity,

$$\vec{u} = \vec{u}_{wall} \tag{2.50}$$

At the inlet, the velocity distributions are prescribed. At the outlet, the distributions of velocity usually are unknown. A common practice is that the velocity gradients along the streamwise direction are taken as zero

$$\vec{u}_{\xi} = 0 \quad \text{or} \quad \vec{u}_{\eta} = 0 \tag{2.51}$$

2.4.2 Boundary Conditions for the Pressure Correction Equation

Usually, two types of boundary conditions are applied for the pressure correction equation. If the pressure is known at the boundary, the pressure correction is of course zero. If the velocity is known at the boundary, then, according to Eq. (2.41) or Eq. (2.42)

$$U = U^* \text{ or } V = V^* \tag{2.52}$$

This implies that

$$p'_{\xi} = 0 \text{ or } p'_{\eta} = 0 \tag{2.53}$$

i.e., the Neumann type boundary condition is applied to the pressure correction equation. At the outlet, where the boundary condition Eq. (2.51) is applied for velocity, the Neumann type boundary condition—Eq. (2.53) is applied to the pressure correction equation on an iteration basis. This implies that the velocity at the last iteration is assumed known, while Eq. (2.51) and Eq. (2.53) are applied alternately for the momentum equations and the pressure correction, respectively. However, this does not guarantee that the mass conservation over the entire domain is enforced. Usually, a global mass conservation correction is introduced in the iteration process to accelerate convergence and to guarantee that the continuity equation is satisfied at the convergence.(Shyy 1987, Blosch et al. 1994). In the global mass conservation correction step, the mass flux difference between the inflow and outflow is computed, and equally distributed along the outflow boundary. This is equivalent to imposing an extra boundary condition

$$\nabla \cdot \vec{u} = 0 \tag{2.54}$$

over the entire domain to guarantee that the pressure correction equation—Eq. (2.43) with its associate boundary conditions is consistent to the original continuity equation. However,

it should be noted that this extra boundary condition is only applied on the global basis, due to the lack of detail information of velocity distribution over the outflow boundary. Another issue should be pointed out that with Eq. (2.53) as the boundary condition, the pressure is only be known up to an arbitrary constant. Usually, the pressure at a reference point is fixed, the pressure over rest of the domain will be adjusted accordingly. More discussions about the outflow boundary treatment can be found in Sani and Gresho (1994). The boundary conditions at grid interface for multi-block computations will be discussed in the next chapter.

2.5 The Solution Procedure

In single-block grid computations, the solution procedure is as follows: (a) The momentum equations are solved to obtained the Cartesian velocity components with the guessed pressure field. When solving the momentum equations, the contravariant velocity components U and V are calculated after updating each of the velocity components. (b) With the updated U and V, the pressure correction equation is solved to obtain p'. (c) The Cartesian velocity and pressure fields are updated with the solution of the pressure correction equation with the Dyakonov iterations (Shyy 1994). Procedures (a)–(c) are repeated until the momentum and continuity equations are simultaneously satisfied to the required degree of accuracy. The linearized systems are solved with the line SOR method. With curvilinear coordinates, this combined use of both Cartesian and contravariant velocity components is devised. In particular, while the Cartesian components are the primary dependent variables in momentum equations, the contravariant components are corrected first in the pressure correction step to ensure the satisfaction of mass continuity. The current method has been applied to solve many engineering problems. The detailed assessments of its effectiveness and robustness can be found in Shyy et al. (1985), Braaten and Shyy (1986), Shyy (1994).

2.6 Concluding Remarks

In this chapter, the pressure-based method for solving incompressible viscous flows in non-orthogonal curvilinear coordinate is presented. Basically, the method employs a control volume approach and a staggered grid, and solves the governing equations in a sequential manner. Several common used convection schemes for the momentum equations are presented, and the derivation of the pressure correction equation is detailed. The various boundary conditions for the momentum equations and the pressure correction equation are presented. The role of global mass conservation on solution convergence is discussed. The presentation of the solution algorithm lay the foundation for the development of the interface treatment for the multi-block computation in the following chapters.

CHAPTER 3
MULTI-BLOCK METHOD FOR THE NAVIER-STOKES EQUATIONS

3.1 Background

Multi-block structured grids can be broadly classified as either patched grids (Rai 1984) or overlapping grids (Steger 1991). Patched grids are individual grid blocks of which two neighboring blocks are joined together at a common grid line without overlap. With overlapping grids, the grid blocks can be arbitrarily superimposed on each other to cover the domain of interest. Compared to patched grids, overlapping grids are more flexible to generate and can be more easily fitted to complex geometry, but information transfer between blocks is more complicated and flux conservation is more difficult to maintain. For both grid arrangements, the issues of interface treatment regarding both conservation laws and spatial accuracy need to be addressed. For flow problems involving discontinuities or sharp gradients of flow variables, it is well know that it is often advantageous to use a numerical scheme in conservation form. The need for accurate conservative grid interfaces was illustrated by Benek et al. (1983). Rai (1984, 1985) has developed a conservative interface treatment for patched grids and has conducted calculations demonstrating the shock capturing capability with the discontinuous grid interface. Berger (1987) has given a discussion of conservative interpolation in overlapping grids. Chesshire and Henshaw (1990, 1994) have conducted analyses on grid interface treatment and developed data structures for conservative interpolation on general overlapping grids. They solved slowly and fast moving shock problems with both conservative and non-conservative interpolation and found that, with the appropriate form of artificial viscosity, both conservative and non-conservative interface schemes can give good results. Part-Enander and Sjogreen (1994) also compared the effects of both conservative and non-conservative interpolation

on slowly moving shock problems. They found that the non-conservative interpolation could lead to large error; in their approach, the conservative interpolation alone was not stable, and the conservative flux interpolation with a characteristic decomposition and nonlinear filter were necessary to produce a satisfying solution. Meakin (1994) investigated the spatial and temporal accuracy of overlapping method for moving body problems and suggested that the issues with interface treatment was not necessarily one of conservative versus non-conservative, but one of grid resolution. The issue of accurate and conservative treatment of discontinuous grid has also been investigated by Kallinderis (1992). The related work about conservative interface treatment for overlapping grids can also be found in Moon and Liou (1989) and Wang et al. (1995). From the literature cited above, it can be seen that several factors can affect the solution quality for flow problems involving sharp flow gradient and discontinuous grid interfaces, e.g., the order of interpolation accuracy, conservative or non-conservative interpolation, convection schemes (or forms of artificial viscosity), and grid resolution. Which factor (or combination of several different factors) has the most critical effect is still not clear. Ideally, the physical conservation laws should be satisfied in the entire domain, but when discontinuous grids are encountered, to what extent should flux be conserved is still an open question. For some problems, compromise has to be made between maintaining flux conservation and interpolation accuracy consistently in both grid interface and interior regions. All these problems need to be investigated further.

For solving incompressible flow problems, because of the decoupling of thermodynamic pressure and velocity fields, the way to maintain mass conservation is crucial for designing an effective solving algorithm. Several algorithms have been developed to reach this goal, such as the projection method (Chorin 1967), the SIMPLE method (Patankar 1980) and the PISO method (Issa 1985), to name a few. A common point in those methods is that, instead of solving continuity equation directly, a pressure (or pressure correction) equation (formed by manipulating the continuity and momentum

equations) is solved in conjunction with the momentum equations. One of the key points for the success of those algorithms lies in whether the pressure (or pressure correction) equation and the associated boundary conditions truly represent the original equation—the continuity equation and the corresponding boundary conditions; in other words, whether the conservation of mass flux over the whole flow domain is strictly satisfied or not. For multi-block computation of incompressible flow, the maintenance of mass conservation across discontinuous grid interfaces is also an important issue. Some efforts have been made with different interface treatments for mass flux. For example, two-dimensional incompressible flow problems have been computed by employing patched grids (Perng and Street 1991, Lai et al. 1993, Thakur et al.1995). In those methods, the grid interface arrangements are either continuous or one coarse grid including integer number of fine grids so that the maintenance of mass conservation across the grid interface is relatively easy. Several authors (Meakin and Street 1988, Hinatsu and Ferziger 1991, Strikwerda and Scarbnick 1993 and Henshaw 1994) solved the flow problems using the overlapping grids and just employed direct interpolation of the dependent variables across the grid interface. The extent of satisfaction of mass conservation there depends solely on the order of the interpolation methods used. Yung et al. (1989) and Tu and Fuchs (1993) have used different mass correction methods to achieve global mass conservation across the grid interface, but the effects of those methods on solution accuracy have not been assessed. Wright and Shyy (1993) have developed a pressure-based multi-block method based on the discontinuous overlapping grid technique for solving the incompressible Navier-Stokes equations in Cartesian grid system. A locally conservative interface scheme, with first order accuracy, is devised to ensure that local and global conservation of mass and momentum fluxes are maintained. This overlapping grid methodology has been extend to the non-orthogonal curvilinear coordinates (Shyy et al. 1994). The related work about domain decomposition and parallel computation methods can be found in Gropp and Keyes (1992a, 1992b). Although much progress has been made in this field, some fundamental issues remain

unsolved. For mass flux treatment, an interface scheme with global mass conservation may not be sufficient to yield accurate solution. On the other hand, a local conservative interface scheme may have difficulties maintaining equal accuracy between the interface and interior regions. Furthermore, for incompressible flow computations, the pressure is generally known up to an arbitrary constant. When the flow solver is applied to multi-block grids, how to couple pressure fields in different blocks, and at the same time maintain mass flux conservation across interface is an important issue to be addressed.

3.2 Notation of Multi-Block Grids

In this section, the notation of multi-block grids is introduced in order to lay the foundation for the development of numerical method for multi-block computation in the later section. Suppose an entire computational domain is denoted as D. The whole domain D can be partitioned into a series of subdomains (or block) D_i, which either can overlap or patch one another, as indicated in Fig. 3.1. Then, the whole domain D can be considered as an union of subdomains D_i

$$D = D_1 \cup D_2 \cup \cdots\cdots \cup D_N \tag{3.1}$$

Similarly, suppose Φ is the solution of a particular equation or a system of equations over the entire domain D, the solution Φ can be composed of solutions on each subdomain

$$\Phi = \Phi_1 \cup \Phi_2 \cup \cdots\cdots \cup \Phi_N \tag{3.2}$$

3.3 Analysis of Model Equations

3.3.1 1-D Poisson Equation

Let us first consider a 1-D Poisson equation as an example to illustrate possible interface treatment methods. The Poisson equation is a second-order elliptic equation which can represent many different physical processes and can be considered as the degenerate

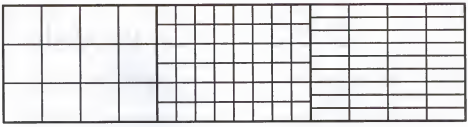

(a) patched grid

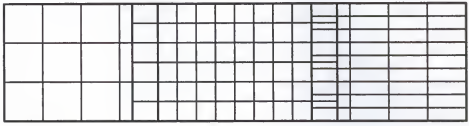

(b) overlapping grid

Fig. 3.1 Multi-block grid layouts

equation of the more general convection-diffusion equation. Suppose the governing equation and the associated boundary conditions are as following

$$\begin{cases} \Phi_{xx} = f \ , & x \in (0,1) \\ \Phi(0) = a \ , & \Phi(1) = b \end{cases} \tag{3.3}$$

where a and b are constants, f is a function of x. Here, the boundary conditions at the two ends of the domain are both Dirichlet conditions. For simplicity, only two grid blocks are considered. The governing equation is discretized on a 2-block overlapping grid as illustrated in the following expressions and Fig. 3.2

$$D_1 = \{x_1(i) | x_1(i) = x_1(1) + ih_1, \ i = 1, 2, ...N_1\} \tag{3.4}$$

$$D_2 = \{x_2(i) | x_2(i) = x_2(1) + ih_2, \ i = 1, 2, ...N_2\} \tag{3.5}$$

$$d = x_1(N_1) - x_2(1) \geq 0 \tag{3.6}$$

Let $\Phi_{k,i}$ denote the discrete approximation to Φ on the component grid k=1, 2 for i=1,2, ..., N_k. Here $\Phi_{k,i}$ is defined at the midpoints of the grid cells, as shown in Fig. 3.3. The grid

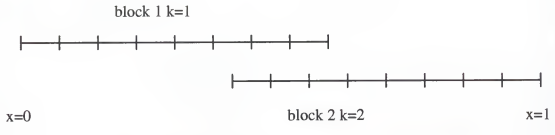

(a) One-dimensional multi-block grid for the interval [0,1]

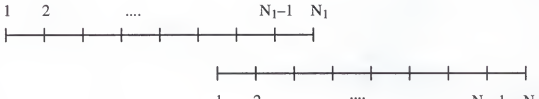

(b) Numbering of grid points

Fig. 3.2 One-dimensional multi-block grid organization

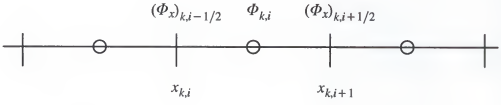

Fig. 3.3 Location of discrete variables

points will be denoted by $x_{k,i}$ with grid spacings $h_{k,i} = x_{k,i+1} - x_{k,i}$. In the present example,

for simplicity, the uniform grid spacing is used on each grid block k=1,2, so that $h_k = h_{k,i}$, for i=1,2, ...,N_k. Therefore, the governing equation can be discretized as:

$$(\Phi_x)_{k,i+1/2} - (\Phi_x)_{k,i-1/2} = h_k f_{k,i} \tag{3.7}$$

$$\Phi_{k,i+1} - 2\Phi_{k,i} + \Phi_{k,i-1} = (h_k)^2 f_{k,i} \tag{3.8}$$

The discretized equation on each block can be solved with either direct methods or iterative methods. However, the boundary conditions at the interfaces have to be provided to connect the solutions on the two blocks together so that a global solution can be obtained. In the following, different interface treatments will be discussed.

(a) Dirichlet interface condition

On block grid 1, Φ_{1,N_1} is unknown, and on block grid 2, $\Phi_{2,1}$ is unknown. They can be interpolated from the other grid in the following form

$$\Phi_{1,N_1} = \sum_{j=L_1}^{L_2} \gamma_j \Phi_{2,j} , \qquad 1 \le L_1 \le L_2 \le N_2 \tag{3.9}$$

$$\Phi_{2,1} = \sum_{j=M_1}^{M_2} \beta_j \Phi_{1,j} , \qquad 1 \le M_1 \le M_2 \le N_1 \tag{3.10}$$

where γ_j and β_j are interpolation coefficients. How many terms are involved in the interpolation is determined by the order of interpolation formula chosen. With this treatment, the unknown value of the dependent variable at the interface is interpolated from the other block and is supposed to be known, so that it is called Dirichlet type interface treatment, or simply, the D-type treatment. If both blocks use the D-type at the interfaces, this combination is called the D-D type treatment. With the above interface treatment, an iteration process between two blocks can be conducted to solve the equation on the whole domain.

(b) Neumann interface condition

For the second-order equation, Eq. (3.7), an alternative interface treatment can be used. Instead Φ, first-order derivative Φ_x is interpolated at the interface

$$(\Phi_x)_{1,N_1-1/2} = \sum_{j=L_1}^{L_2} \gamma_j (\Phi_x)_{2,j+1/2} \quad , \qquad 0 \le L_1 \le L_2 \le N_2 - 1 \tag{3.11}$$

$$(\Phi_x)_{2,1/2} = \sum_{j=M_1}^{M_2} \beta_j (\Phi_x)_{1,j+1/2} \quad , \qquad 0 \le M_1 \le M_2 \le N_1 - 1 \tag{3.12}$$

With this treatment, the derivative of Φ is interpolated from the other block and is supposed to be known, so that it is called Neumann type interface treatment, or the N-type treatment. If both blocks use the N-type treatment, then it is called the N-N type interface treatment. It is noted that for a 2-block 1-D Poisson equation, if the N-N type interface treatment is used, a physical unrealistic solution may be obtained, since the N-N type treatment only requires the first-order derivatives are equal at the interface, i.e.,

$$(\Phi_x)_1 = (\Phi_x)_2 \tag{3.13}$$

Across the interface, a constant may exist between the solutions from two blocks in the overlapping region, namely,

$$\Phi_1 = \Phi_2 + c \tag{3.14}$$

because Eq. (3.14) satisfies Eq. (3.13). A remedy to this problem is to use the N-type treatment at one side and the D-type treatment at the other side of the interface, which is called the D-N type interface treatment. The D-N type treatment can eliminate the possible non-uniqueness problem with the N-N type treatment. The different interface treatments considered here may have different effects on the convergence rate when solving the equation on multi-block grids (Rodrigue and Shah 1989).

3.3.2 2-D Poisson Equation

Here, the 2-D Poisson equation is considered as following

$$\Phi_{xx} + \Phi_{yy} = f \tag{3.15}$$

The computational domain is a rectangular domain, as illustrated in Fig. 3.4. It is decomposed into 2 overlapping domain D_1 and D_2 with a overlapping distance d>0 in the

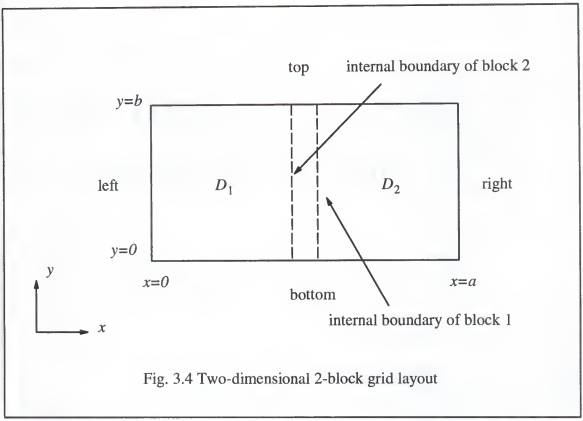

Fig. 3.4 Two-dimensional 2-block grid layout

x direction. With this configuration, what type of interface treatment can be applied also depends on what kind of physical boundary condition the problem has. For example, if the physical boundary conditions at all four domain boundaries are Dirichlet type, then all the interface treatments discussed above can yield unique solutions (Rodrigue and Shah 1989). On the other hand, if, at the top and bottom boundaries, the physical boundary conditions are of Neumann type, i.e.,

$$\Phi_y = c \tag{3.16}$$

where c is a constant, the N-N type interface treatment can not guarantee an unique solution (Wright and Shyy 1996). In addition, if, at the top and bottom boundaries, the physical boundary conditions are periodic condition, namely,

$$(\Phi)_{top} = (\Phi)_{bottom} \tag{3.17}$$

the application of the N-N type interface treatment can not guarantee an unique solution either, because there is no constraint at the top and bottom boundaries to fix the solution in the overlapping region.

3.3.3 1-D Convection-Diffusion Equation

Here we consider different interface treatments for a steady one-dimensional convection-diffusion equation discretized on a two-block overlapping grid. The governing equation is

$$(\varrho u\Phi)_x = (\Gamma\Phi_x)_x \tag{3.18}$$

Integration of Eq. (3.18) over the control volume as indicated in Fig. 3.5, gives

$$(\varrho u\Phi)_e - (\varrho u\Phi)_w = (\Gamma\Phi_x)_e - (\Gamma\Phi_x)_w \tag{3.19}$$

If we take

$$\Phi_e = 1/2(\Phi_E + \Phi_P) \quad \text{and} \quad \Phi_w = 1/2(\Phi_P + \Phi_W) \tag{3.20}$$

and use central difference scheme for the diffusion terms, Eq. (3.19) can be written as

$$\frac{1}{2}(\varrho u)_e(\Phi_E + \Phi_P) - \frac{1}{2}(\varrho u)_w(\Phi_P + \Phi_W) = \frac{\Gamma(\Phi_E - \Phi_P)}{\Delta x} - \frac{\Gamma(\Phi_P - \Phi_W)}{\Delta x} \tag{3.21}$$

If we define

$$F = \varrho u \ , \qquad D = \frac{\Gamma}{\Delta x} \tag{3.22}$$

the discretized equation becomes

$$a_P\Phi_P = a_E\Phi_E + a_W\Phi_W \tag{3.23}$$

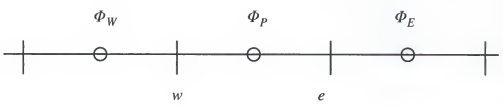

Fig. 3.5 Illustration of the control volume

where

$$a_E = D_e - \frac{F_e}{2} \quad , \qquad a_W = D_w - \frac{F_w}{2} \tag{3.24}$$

$$a_P = D_e + \frac{F_e}{2} + D_w - \frac{F_w}{2} \tag{3.25}$$

The first interface treatment to be considered is simply of Dirichlet type. If the two-block domain is the same as that shown in Fig. 3.2, at the right boundary of block 1, the boundary value of $\Phi_{1,N}$ can be interpolated from block 2. In order to evaluate the associated coefficient a_W at the interface, i.e., $a_{1,N}$, we have to obtain the coefficients D_w and $F_w/2$ using the the values from block 1 and interpolated values from block 2. The same method is applied to the left boundary of block 2

An alternative interface condition can be derived directly from Eq. (3.19), i.e., at the right boundary of block 1, the total flux

$$-(\rho u\Phi)_w + (\Gamma\Phi_x)_w \tag{3.26}$$

can be directly interpolated from block 2, i.e.,

$$(-\rho u\Phi + \Gamma\Phi_x)_{1,N_1-1/2} = \sum_{j=L_1}^{L_2} \gamma_j(-\rho u\Phi + \Gamma\Phi_x)_{2,j+1/2}, \quad 0 \le L_1 \le L_2 \le N_2 - 1 \tag{3.27}$$

This interface treatment is of Rubin type, or simply, the R-type. Similar to the N-N type interface treatment, if the R-R type treatment is applied, the nonuniqueness problem may appear. The D-R type interface treatment may fix this problem, or an extra constraint can be used to match the solutions in two blocks together (Chesshire and Henshaw 1994).

3.4 Analysis of the Naiver-Stokes Equations

The interface treatments for solving the model equations on two overlapping grids have been discussed in the last section. It can be extended to the Navier-Stokes computation.

However, there are some special issues associated with the Navier-Stokes computation in multi-block configurations that need to be addressed.

We begin by considering two domains Ω_1 and Ω_2 which can overlap or patch together. We denote the Navier-Stokes equations, Eq. (2.2–2.3) by the following

$$\mathcal{N}(\vec{u}, p) = 0 \tag{3.28}$$

The continuity equation, Eq. (2.1) is replaced by the pressure correction equation, Eq. (2.43), which is denoted as

$$P(p') = f(\vec{u}^*) \tag{3.29}$$

where $\vec{u}^*$ is the intermediate velocity. We will solve Eq. (3.28–3.29) on each separate domain. Boundary conditions for each domain are specified only on that part of the boundary which is not interior to the other domain. For the purpose of discussion, we assume that the velocity $\vec{u}$ is specified by the boundary value $\vec{b}$ on the boundary of $\Omega_1 \cup \Omega_2$. For that part of $\partial\Omega_1$ (the boundary of Ω_1) that lies within or patch with Ω_2 we require that the velocity and pressure to be equal to those obtained from the solution on Ω_2, and similarly for that portion of $\partial\Omega_2$ within or patch with Ω_1. When grid lines of the two domain over the overlapping region or at the patched boundary are not exactly matched, flow variables have to be interpolated between the two domains. The interpolation methods discussed in the last section can be directly applied to the Navier-Stokes equations.

However, the continuity equation requires the following compatibility condition to be satisfied by the boundary value $\vec{b}$,

$$\int_{\partial(\Omega_1 \cup \Omega_2)} \vec{b} \cdot \vec{n} = 0 \tag{3.30}$$

where $\vec{n}$ is the normal unit vector of boundary $\partial(\Omega_1 \cup \Omega_2)$. When we solve the governing equations on both domains, the continuity equation should be satisfied on each domain. i.e.,

$$\nabla \cdot \vec{u} = 0 \quad \text{on} \quad \Omega_i, \quad i = 1, 2 \tag{3.31}$$

or

$$\int_{\partial\Omega_i} \vec{u} \cdot \vec{n} = 0 , \quad i = 1,2 \tag{3.32}$$

This implies that across grid interface, the mass flux should be conserved,

$$\int_{interface} \vec{u}_1 \cdot \vec{n} = \int_{interface} \vec{u}_2 \cdot \vec{n} \tag{3.33}$$

otherwise, mass source or sink will be created at the interface. It is noted that Eq. (3.33) is an integral condition over the entire interface, but it also should be satisfied across any portion of the interface, i.e., on a local grid cell by cell basis.

However, interpolations of any order will introduce truncation errors, which will violate Eq. (3.33). The effect of interpolations between mass flux at the grid interface on the solution accuracy depends on the order of the interpolation. If necessary, based on interpolations, conservative correction of mass flux should be applied. In the following, details of the interface treatments for the Navier-Stokes equations will be presented.

3.5 Multi-Block Interface Treatments for the Navier-Stokes Equations

3.5.1 Multi-Block Grid Arrangement

In the current multi-block computational method, the entire flow domain can be decomposed into several subdomains (or blocks). Within each block, a structured grid is generated. Two different blocks can either patch together or overlap over several grid layers. In the present approach, between the adjacent blocks, the grid lines can be discontinuous, and multiple number of blocks can simultaneously overlap at the same location, if necessary (Wright and Shyy 1993, Shyy 1994). At grid interfaces, the grid lines of a given block are extended to the adjacent block by two grid cells to accommodate the 5-point convection schemes. More details will follow later.

3.5.2 Interface Treatment for the Momentum Equations

3.5.2.1 Direct interpolation of dependent variables

For the momentum equations, at an interface, both velocity and pressure boundary conditions are needed. If the south boundary is the internal boundary, let us consider the u-momentum equation as an example, the total momentum flux at the south boundary

$$F = \varrho Vu - y_\xi p - \frac{\mu}{J}(- q_2 u_\xi + q_3 u_\eta) \tag{3.34}$$

needs to be evaluated at the grid interface. For smooth flow fields, the direct interpolation of dependent variables from the adjacent block should be satisfactory. With the extended grid points, the dependent variables u, v and p can be interpolated from the adjacent block, and the geometric quantities y_ξ, q_2, q_3 and J can also be evaluated with the grid values in both blocks. A linear (or quadratic) interpolation can be used. The same approach is applicable to the boundaries on the other sides.

3.5.2.2 Interpolation of momentum fluxes

For problems involving large flow gradients, the conservative treatment of momentum fluxes is often desirable. Here, to analyze the interpolation of momentum fluxes as the internal boundary condition at a grid interface, consider the flux at the south boundary again. As indicated by Eq. (3.34), the momentum flux F includes convection, diffusion and pressure terms. One straightforward way is to directly interpolate flux F as a whole, from the adjacent block, and then put the flux into the source term of Eq (2.16). However, the flux F includes gradient terms such as u_ξ and u_η, direct interpolation of these gradient terms admits solutions where an arbitrary constant may be added to the solution on each grid, rendering the solution nonuniform (Wright and Shyy 1996). In the current treatment, the flux F is split into two terms, as indicated by Eq. (3.35), and the two terms are treated separately.

$$F = \underset{(i)}{\left[\varrho Vu - y_\xi p\right]} - \underset{(ii)}{\left[\frac{\mu}{J}(- q_2 u_\xi + q_3 u_\eta)\right]} \tag{3.35}$$

The first term in F is interpolated directly from the adjacent block, and is put into the source term in Eq. (2.16). For the second term, u itself is interpolated from the adjacent block, and gradient terms u_ξ and u_η at the interface are evaluated with the u values in both blocks. In this way, the problem of nonuniqueness is eliminated, and at the same time, the convection and pressure fluxes can be interpolated directly from the adjacent block.

Now, consider the interpolation of the first term in flux F,

$$F_1 = \rho V u - y_\xi p = \rho(v x_\xi - u y_\xi)u - y_\xi p \tag{3.36}$$

which includes geometric terms x_ξ and y_ξ. Since there is no relation between x_ξ and y_ξ in different blocks, it is fundamentally wrong to conduct a straightforward interpolation of F_1 between different blocks according to the form of Eq. (3.36). On the other hand, F_1 can be written in another form, namely,

$$\begin{aligned} F_1 &= \frac{\rho(v x_\xi - u y_\xi)u - y_\xi p}{(x_\xi^2 + y_\xi^2)^{1/2}} \quad (x_\xi^2 + y_\xi^2)^{1/2} \\ &= [\rho(v\cos\theta - u\sin\theta)u - p\sin\theta] \quad (x_\xi^2 + y_\xi^2)^{1/2} \\ &= \overline{F}_1 \; S \end{aligned} \tag{3.37}$$

where $\overline{F}_1$ is the normalized flux, and

$$\sin\theta = \frac{y_\xi}{(x_\xi^2 + y_\xi^2)^{1/2}} \tag{3.38}$$

$$\cos\theta = \frac{x_\xi}{(x_\xi^2 + y_\xi^2)^{1/2}} \tag{3.39}$$

$$S = (x_\xi^2 + y_\xi^2)^{1/2} \tag{3.40}$$

Here, θ is the angle between the grid line and the x-axis, and S is the length of grid face, as shown in Fig. 3.6. With the current interface arrangement, the angle θ in different blocks at the interface can be estimated directly and the normalized flux $\overline{F}_1$ can be interpolated directly. If we let the superscript 1 denote the current block and 2 denote the adjacent block, then the following expressions are obtained:

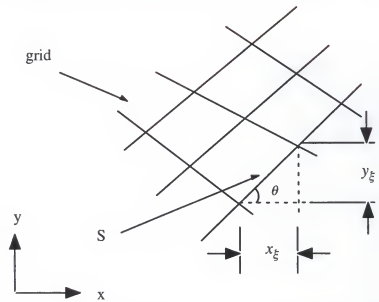

Fig. 3.6 Configuration of momentum flux interpolation

$$\overline{F}^{(1)}{}_1 = \sum_{i=1}^{i=k} \gamma_i \, \overline{F}^{(2)}{}_{1i} = \sum_{i=1}^{i=k} \gamma_i \, \frac{F^{(2)}{}_{1i}}{S^{(2)}{}_i} \tag{3.41}$$

$$F^{(1)}{}_1 = \overline{F}^{(1)}{}_1 S^{(1)} = S^{(1)} \sum_{i=1}^{i=k} \gamma_i \, \frac{F^{(2)}{}_{1i}}{S^{(2)}{}_i} \tag{3.42}$$

where γ_i s are the interpolation coefficients which depend on the interpolation formula adopted. With the above interpolation treatment, the conservation of flux F_1 is not strictly enforced. Later, an interpolation scheme with local conservative correction method will be introduced to strictly conserve the flux F_1. In summary, in the present interface treatment, the nonlinear part and the diffusion part of total momentum flux are treated separately. While the nonlinear parts are interpolated totally from the adjacent block, the evaluation of the diffusion flux employes the velocity components from both blocks to avoid creating nonunique solutions.

3.5.3 Interface Treatment for the Pressure Correction Equation

Three interface boundary conditions are proposed for the pressure correction equation. With the first treatment, the mass flux at the interface is taken as the boundary condition for the pressure correction equation. Suppose the south face of a control volume of the pressure correction equation is at the interface, as illustrated in Fig. 3.7. The p' equation for that control volume is as follows,

$$a_P p'_P = a_E p'_E + a_W p'_W + a_N p'_N + S_P \tag{3.43}$$

$$a_P = a_E + a_W + a_N \tag{3.44}$$

$$S_P = (\varrho U^*)_w - (\varrho U^*)_e + (\varrho V)_s - (\varrho V^*)_n \tag{3.45}$$

where $(\varrho V)_s$ is the mass flux from the south face at the interface presumably known, which is interpolated from the values on the adjacent block and is put into the source term. The term $a_S p'_S$ is no longer present in the p' equation for that control volume. Conversely, for the corresponding control volume at the interface of the adjacent block, the north face of control volume of the pressure correction equation is at the interface. The corresponding p' equation is as follows,

$$a_P p'_P = a_E p'_E + a_W p'_W + a_S p'_S + S_P \tag{3.46}$$

$$a_P = a_E + a_W + a_S \tag{3.47}$$

$$S_P = (\varrho U^*)_w - (\varrho U^*)_e + (\varrho V^*)_s - (\varrho V)_n \tag{3.48}$$

where $(\varrho V)_n$ is interpolated and $a_N p'_N$ is no longer present. Thus, on both sides of the grid interface, the boundary conditions for p' equation are implemented via the mass flux (ϱV) and are of the Neumann type. In other words, the pressure fields in different blocks are independent of one another. To make the pressure field compatible in the entire flow domain, the reference pressure in each block resulting from the Neumann boundary condition is adjusted according to the total momentum flux balance at a common line in the overlapping region between the blocks (Wright and Shyy 1993, Shyy 1994). This treatment is called method NN (meaning Neumann-Neumann condition). It is noted that when evaluating the

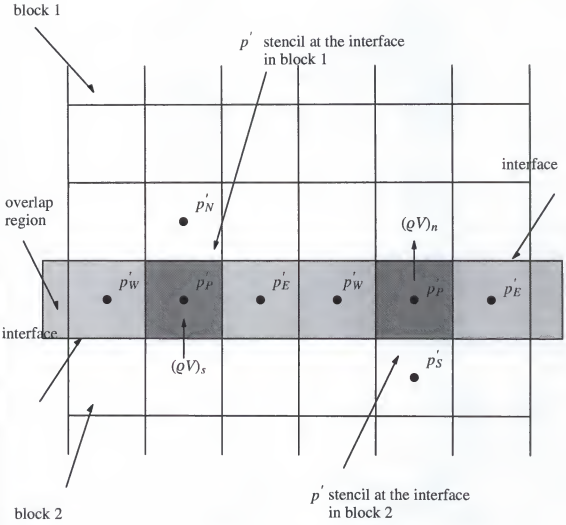

Fig. 3.7 Interface layout with one grid layer overlap

coefficients a_E and a_W terms in Eq. (3.43), whose expressions are shown in Eqs. (2.46) and (2.47), the A_P^v term need to be evaluated, which is shown from Eqs. (2.24), if the central difference scheme is used for the convection term. The term A_P^v is taken from the average of four surrounding values from the corresponding *v*-momentum equation, two of which are at the interface. The associated (ϱU) and (ϱV) are evaluated from the values within the block and the interpolated values in the adjacent block; the terms $\mu q_1/J$ and $\mu q_3/J$ are evaluated from the grid points within the current block and the extended fictitious points in the adjacent block.

With the second method, for the p' equation, on one side of the interface, the interpolated mass flux normal to the interface, say, $(\varrho V)_s$, is still used as the boundary condition in grid block 1, as shown in Fig. 3.8. On the other side of the interface, in the adjacent block, instead of $(\varrho V)_n$, p_N' is interpolated from grid block 1, as the boundary condition, as illustrated in Fig. 3.8. Besides the coefficients a_E and a_W discussed in the first method, another coefficient a_N need to be evaluated at the interface, which is expressed as below:

$$a_N = \varrho\left(\frac{x_\xi^2}{A_P^v} + \frac{y_\xi^2}{A_P^u}\right)_n \tag{3.49}$$

The term $(A_P^u)_n$ is the average from the values at four surrounding *u*-locations. At the interface, the two locations are outside the current block, as illustrated in Fig. 3.9. To compute the A_P^u at those two locations, whose expression is shown in Eq. (2.24), the terms (ϱU) and (ϱV) are interpolated at the extended grid points, and the terms $\mu q_1/J$ and $\mu q_3/J$ are evaluated using both the grid points within the current block and the extended fictitious points in the adjacent block. The similar method is applied when evaluating the $(A_P^v)_n$ term at the interface. The source term S_P still has its original form given by Eq. (2.45), in which the term $(\varrho V^*)_n$ is actually computed using the *v* value at the interface and the *u* values within the current block and the interpolated values outside the block. In summary, on one side of

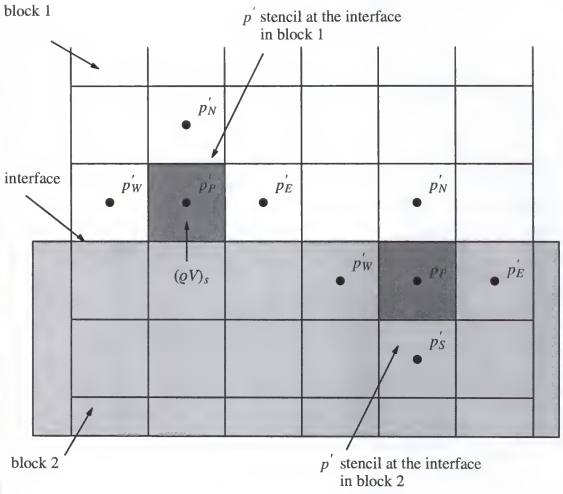

Fig. 3.8 Interface layout without overlap

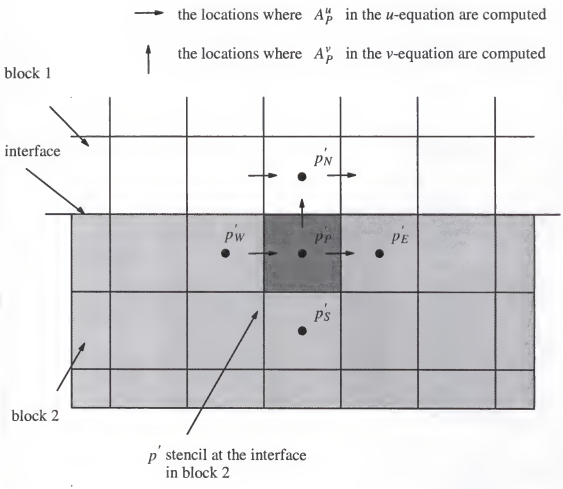

Fig. 3.9 Interpolation stencil for pressure correction equation at grid interface

the interface, the (ϱV) term is computed, while on the other side, it is interpolated. It is also noted that with the second treatment, the boundary condition is of Neumann type on one side and Dirichlet type on the other side. Since the pressure fields across the interface are tightly coupled together, the adjustment for the pressure field between blocks is no longer needed. This treatment is called method DN, standing for Dirichlet-Neumann condition. The third method is to interpolate the pressure correction p' at both sides of the interface. which is called method DD, standing for Dirichlet-Dirichlet condition.

3.5.4 Interface Treatment for Mass Flux

In the previous section, the interface treatments for the pressure correction equation are discussed, and three interface conditions are proposed. In those interface conditions, two of them involve using the interpolated mass flux from the adjacent block as the interface boundary condition. In the following, the interpolation of mass flux is discussed.

3.5.4.1 Linear (quadratic) interpolation of mass flux

With this treatment, the mass flux (ϱU) or (ϱV) is directly interpolated from the adjacent block, as discussed in the last section. However, this direct interpolation is not conservative, i.e., across the interface, the total interpolated flux is not equal to the original flux. The difference between the two fluxes depends on the order of the interpolation formula.

3.5.4.2 Interpolation with global correction

A natural way to get the conservative flux is to globally correct the flux after the interpolation. First, a non-conservative interpolation is conducted to obtain the flux at the interface from the neighboring block. The total flux evaluated from the neighboring block is denoted as F_a, the total interpolated flux is denoted as F_c. Second, the flux deficit $\Delta F = F_a - F_c$ is computed. Then, the flux at each current interface control volume face is added with $\Delta F/N$ (suppose there are N control volumes at the interface of the current block) so that the total flux across the interface is conserved globally. But this conservation is not locally enforced, and its effect on the solution need to be assessed.

3.5.4.3 Piecewise constant interpolation

Piecewise constant interpolation, which is used with inviscid flows by Rai (1984), is by nature locally conservative, but with only first order accuracy. It may cause accuracy problems for viscous flow computations

3.5.4.4 Linear (quadratic) interpolation with local conservative correction

With this treatment, the flux is interpolated first with linear or quadratic formula, then, the interpolated flux is corrected locally on a grid cell by cell basis. This treatment will be discussed in detail. Suppose a portion of an interface, corresponds to the width of a single control volume of the coarse grid 1, and to the width of several control volumes of the fine grid 2, indexed from i=1 to imax. This scenario is shown schematically in Fig. 3.10, where $\overline{V}_c$ is the contravariant velocity component normal to the grid face, normalized by the control volume face length S_c, at the coarse grid control volume face; and $\overline{V}_{fi}$ represents the contravariant velocity component, normalized by the control volume face length S_{fi}, at the fine grid control volume face. From the fine grid to coarse grid, $\overline{V}_c$ can be obtained as:

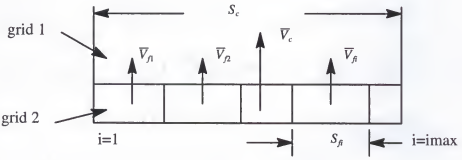

Fig. 3.10 Notations used in two-block interface (subscript c and f designate coarse and fine grid quantities, respectively).

$$\overline{V}_c S_c = \sum_{i=1}^{imax} \overline{V}_{fi} S_{fi} \tag{3.50}$$

Equation (3.50) is for the constant density flow. It can be easily extended to account for density variation. For the sake of simplicity, this aspect is neglected in the current discussion. In this way, the flux into the coarse grid control volume is uniquely determined from the corresponding fine grid fluxes conservatively. Conversely, given the coarse grid flux $\overline{V}_c S_c$, the conservation constraint yields the follow:

$$\sum_{i=1}^{imax} \overline{V}_{fi} S_{fi} = \overline{V}_c S_c \tag{3.51}$$

In this situation, conservation does not provide unique values for the $\overline{V}_{fi}$. A certain distribution has to be chosen to determine each $\overline{V}_{fi}$. As a first approximation, $\overline{V}_{fi}$ is obtained using the linear (or quadratic) interpolation of the normalized contravariant velocity in the coarse grid. The interpolated value is denoted as $\overline{V'}_{fi}$. With the first approximation, Equation (3.51) is not satisfied. Then the fine grid fluxes are scaled so that the total flux obtained is $\overline{V}_c S_c$. Accordingly, the values $\overline{V}_{fi}$ at the fine grid boundary are computed as follows:

$$\overline{V}_{fi} S_{fi} = \frac{|\overline{V'}_{fi}| S_{fi}}{\sum_{i=1}^{imax} |\overline{V'}_{fi}| S_{fi}} \overline{V}_c S_c \tag{3.52}$$

From Eq. (3.52), it can be seen that Eq. (3.51) expressing flux conservation from coarse grid to fine grid is satisfied and the flux distribution is close to that determined by the interpolation employed.

If the grid interface is not exactly matched in the sense of a coarse control volume face adjoining an integer number of fine grid control volume faces, a split-merge procedure is devised. The control volume in grid 2 can be split into smaller subcontrol volumes. In this manner, from control volumes in grid 1 and subcontrol volumes in grid 2, the locally conservative treatment can still be applied on a cell by cell basis, after the interpolation and

correction have been conducted. After that, the fluxes at the split subcontrol volume faces will be merged back to get the flux at the original control volume face. From grid 2 to grid 1, this same split-merge treatment is also applicable. The only extra work in this procedure is to create some arrays to store the intermediate information. Thus, the interface can be treated no matter what kind of interface arrangement is encountered. This linear (quadratic) interpolation with local correction treatment is not limited to the mass flux, it can also be applied to the conservative treatment of the momentum flux.

3.6 Solution Methods

After governing equations are discretized on multi-block domain, it can be solved by different solvers and solution strategies. Suppose there is a two-block domain $D = D_1 \cup D_2$. After the governing equations are discretized, we get two linear systems,

$$A_1\Phi_1 = f_1 \tag{3.53}$$

$$A_2\Phi_2 = f_2 \tag{3.54}$$

At the block interface, there is a interpolation relation between Φ_1 and Φ_2, say,

$$L_1\Phi_1 = L_2\Phi_2 \tag{3.55}$$

where L_1 and L_2 are interpolation operators. The three equations, Eq. (3.53–3.55) can be assembled into one linear system on domain of $D = D_1 \cup D_2$,

$$A\Phi = f \tag{3.56}$$

This whole linear system can be solved by different direct or iterative solvers. With this kind of strategy, the flexibility of grid generation is still retained, but the flexibility and convenience of implementation are lost. Furthermore, it is more difficult to achieve memory savings for large system equations. A more attractive method is to solve the each linear system on its block individually, with direct or iterative solvers. Between solution sweeps in each block, an updating exchange between blocks is conducted by interpolation. Suppose

S_i denotes solution sweep on block i, I_i denotes interpolation from block i. In two-block cases, the solution sequence could be

$$S_1 \rightarrow S_2 \rightarrow I_1 \rightarrow I_2 \tag{3.57}$$

or

$$S_1 \rightarrow I_2 \rightarrow S_2 \rightarrow I_1 \tag{3.58}$$

In this way, not only the flexibility of grid generation is retained, the implementation could be easier and more flexible also. More information about the efficiency of solution strategies on multi-block grids can be found in Meakin and Street (1988).

3.7 Solution Strategy for the Navier-Stokes Equations on Multi-Block Grids

3.7.1 Solution Procedure for Single Block Computations

For single block computations the procedure is as following:

(1) Guess the pressure field p^*.

(2) Solve the momentum equations to obtain u^* and v^*.

(3) Solve p' equation.

(4) Calculate p by adding p' to p^*.

(5) Calculate u and v from their stared values using velocity-correction formulas Eq.(2.41–2.42), and relations between velocities and contravariant velocities, Eq. (2.7–2.8).

(6) Solve the discretization equations for other scalar quantities (such as temperature, concentration and turbulence quantities) if they influence the flow filed through fluid properties, source terms, etc.

(7) Treat the corrected pressure p as a new guested pressure p^*, return to Step (2), and repeat the whole procedure until a converged solution is obtained.

It is noted that during this procedure, the solution of u^*, $v^*$and p' only proceed a few sweep steps, instead of solving each of those many steps, before going to solve other variables. Because between the outer iterations, if all other variables are in the intermediate

stages, only one variable is solved close to convergence does not help converge all the variables very much. The procedure adopted here can keep tighter coupling between the variables in the process of iteration. Furthermore, to prevent the iterations divergence or accelerate convergence, we usually under-relax u^* and v^* (with respect to the previous values of u and v) while solving the momentum equations. Also, we add only a traction of p' to p^*. In other words, instead of using Eq. (2.31), we employ

$$p = p^* + \alpha_p p' \tag{3.59}$$

with $\alpha_p < 1$, the optimum value of α_p is usually problem dependent.

3.7.2 Solution Procedure for Multi-Block Computations

In multi-block computations, another level of iteration is introduced, i.e., iteration between different grid blocks. With the iterations between equations in each block and iterations between blocks, two different iteration strategies can be adopted:

(a) An outer loop is formed by iterating between blocks; an inner loop is formed by iterating between equations. Between the outer iterations, information transfer between all relevant variables is conducted.

(b) An outer loop is formed between different equations; an inner loop is formed between blocks. Between the inner loop, for each equation, information transfer is conducted.

These two method can be illustrated in the following diagram:

Method (a):

For bn=1,nb

(1) Solve the momentum equations to obtain u^* and v^*.

(2) Solve p' equation.

(3) Calculate p by adding p' to p^*.

(4) Calculate u and v using the velocity-correction formulas.

(5) Solve the discretization equation for other scalar quantities

endfor

Repeat the whole procedure until a converged solution is obtained.

Method (b):

(1) Solve the momentum equations to obtain u^* and v^*, for bn=1,nb

(2) Solve p' equation, for bn=1,nb

(3) Calculate p by adding p' to p^*, for bn=1,nb

(4) Calculate u and v using the velocity-correction formulation for bn=1,nb

(5) Solve the discretization equation for other scalar quantities, bn=1,nb

Return to Step (1), and repeat the whole procedure until a converged solution is obtained. Here, nb denotes the total number of blocks.

In principle, both strategies can be used. Which one give better performance may be problem dependent. In the present method, the first one is adopted. The main consideration is, the evaluation of coefficients for the p' equation must use the stored coefficients from the momentum equations. With method (a), only the coefficients of the momentum equations from one block need to be stored. On the other hand, with method (b), the coefficients of the momentum equations from all the blocks have to be stored. The method (a) saves some memory compared to the method (b).

3.7.3 Convergence Criterion

Given appropriate boundary conditions and a well constructed computational mesh, the flow solver described above can be applied to any shaped domain. This is true whether a global or one of a number of subdomains is being considered. When the solver is applied to a single domain, convergence is measured by how well the computed flow fields satisfy the discrete equation of motion. Specifically, residual sources can be computed for each of the momentum equations, mass continuity equation and governing equations for other scalar variables.

If the discrete equations of motion have been satisfied exactly, then the residual sources will be zero. In practice, however, the residual sources are driven to some specified level of tolerance:

$$Res_i \leq Tol_i \tag{3.60}$$

where *Res* and *Tol* correspond to the *ith* residual source and tolerance, respectively; and i corresponds to u, v, mass and other scalar variables. When the solver is applied to a multi-block domain, one question is to be asked is how the global convergence should be defined and what iterative strategy should be used to achieve the global convergence.

The necessary condition for global convergence must be, in each block the solutions meet the requirements given as Eq. (3.60). However, this condition may not be a sufficient condition to guarantee global convergence, i.e., a highly converged solution can be obtained in one block before moving to a neighboring block. After applying the solver only once in each block, condition (3.60) can be satisfied. However, it is not likely that the correct global solution has been achieved. Rather, a highly converged solution would have been generated for each block based on only intermediate interface boundary conditions. Condition (3.60) is necessary for global convergence, but it is not sufficient to guarantee it. The solutions in the overlap regions must also converge to the same solution. In the present method, the interface information transfer between variables in overlapping regions is based on interpolation. At the global convergence, the differences between solutions in respective overlapping regions should be at the order of interpolation truncation errors. This can be achieved by conducting only a few sweeps between equations within each block, instead of iterating all the equations to a complete convergence in a particular block. Then the iteration sweeps move to other blocks, until the condition (3.60) is satisfied in all the blocks.

3.8 Concluding Remarks

In this chapter, the different interface conditions for solving the second-order model equations in multi-block domain are presented firstly in both one and two-dimensional form.

The effect of the interface condition on the solution uniqueness is discussed. Then the examination of the physical conservation law of Navier-Stokes equations in multi-block domain is conducted. For the momentum equations, the direct interpolation of the dependent variables between blocks can be used. The interpolation of momentum flux accounting for the grid transformation effect is discussed. For the pressure correction equation, three different forms of interface boundary conditions are provided. The interpolation methods for mass flux across grid interfaces with different conservation characteristics are introduced. Especially, A interpolation with local conservative correction method is devised for the flux conservation across interfaces. Finally, the iterative strategies and the convergence criterion are discussed.

CHAPTER 4
DATA STRUCTURES

4.1 General Interface Organization

With multi-block computation methods, because of the introduction of grid interface, certain data structure has to be devised to facilitate information transfer between different grid blocks. In the present method for two-dimensional computation, each grid block has four sides, which are numbered in counter clockwise sequence, as shown in Fig. 4.1. Each side may be divided into several segments corresponding to different boundary condition types (e.g., physical boundary conditions or grid interface condition). For each segment, the indices of the starting and ending grid points, the boundary condition type and the corresponding values of dependent variables on the physical boundaries are assigned. If the segment is a grid interface, the block number of the adjacent block, the identification of overlapping direction (in ξ and η direction), and the number of overlapping layer are assigned as well. Based on these inputs, a series of intersection tests are conducted to provide the information for interpolation coefficients and conservative treatment. all these coefficients are stored in tables for later use.

4.2 Interpolation

For a given grid point or a location of a dependent variable at an interface of a particular grid block, the basic information needed to facilitate the information transfer between the blocks is: (1) the adjacent block number, (2) the indices (ξ, η) of corresponding interpolating control volume, and (3) the interpolation coefficients. Among them, (1) is given by the input, and (2) and (3) will be determined by interpolation.

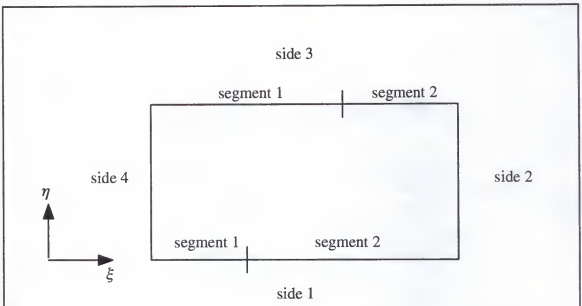

Fig. 4.1 Grid interface organization for multi-block configuration

With the staggered grid arrangement, there are four pairs of interpolation needed for grid points and all the dependent variables, i.e., interpolations between (a) grid vertices (for geometric quantities), (b) grid face centers for velocity u and contravariant velocity U, (c) grid face centers for velocity v and contravariant velocity V, and (d) grid cell centers (for pressure and other scalar variables). These interpolation stencils are indicated in Fig. 4.2. In the present method, only two basic interpolations are conducted, i.e., interpolations for cases (a) and (b). If we take the south boundary as an example, and use the Cartesian grid for simplicity, we can see that, the result of case (a), followed by an average procedure in η direction can be used by case (c), the interpolation for v; similarly, result of case (b) can be used by case (d), the interpolation for scalar variables. The similar approach can be applied to the other three boundary sides.

4.2.1 Grid Vertex Based Interpolation

In the following, the grid vertex-based interpolation is described in detail, and the linear interpolation is taken as example. Suppose there are two grid blocks. Side 3 of block 1 is patched with side 1 of block 2, as indicated in Fig. 4.3. Here, for illustration, the two grids

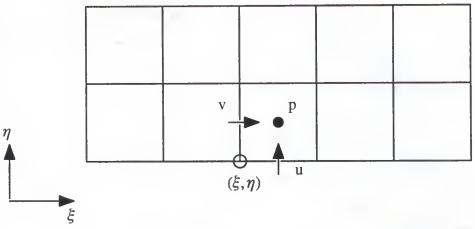

Fig. 4.2 Interpolation stencil for grid points and dependent variables

are taken apart a small distance. Block 1 is also called the current block, and block 2 is called the adjacent block. To conduct interpolation, the relative positions between grid points of block 1 and block 2 at the interface need to be identified. Therefore, the grid lines in η direction in block 1 are extended to intersect with side 1 of block 2. In block 1, line segments are formed by connecting grid points at the interface, i.e., side 3, with grid points next to the interface, as shown in Fig. 4.3. These line segments, for instance, segment $\overline{ab}$ are extended to intersect side 1 of block 2. The side 1 of block 2 are formed by a series of straight line segments between two adjacent grid points. For segment $\overline{ab}$, a series of intersection tests are conducted beginning from the starting point toward the ending point of side 1 of block 2. The straight line passing through point a (x_a, y_a) and point b (x_b, y_b) can be expressed as

$$a_1 y + b_1 x = c_1 \tag{4.1}$$

where

$$a_1 = x_b - x_a \tag{4.2}$$

$$b_1 = y_b - y_a \tag{4.3}$$

$$c_1 = y_a(x_b - x_a) - x_a(y_b - y_a) \tag{4.4}$$

Similarly, for a straight line passing through (x_i, y_i) and (x_{i+1}, y_{i+1}), at side 1 of block 2, the equation is

$$a_2 y + b_2 x = c_2 \tag{4.5}$$

where

$$a_2 = x_{i+1} - x_i \tag{4.6}$$

$$b_2 = y_{i+1} - y_i \tag{4.7}$$

$$c_2 = y_i(x_{i+1} - x_i) - x_i(y_{i+1} - y_i) \tag{4.8}$$

The intersection point (x_s, y_s) of these two lines can be found by solving Eq. (4.1) and Eq. (4.5). If the intersection point falls within the range of (x_i, y_i) and (x_{i+1}, y_{i+1}), the corresponding interpolation coefficients are computed. The returning information is stored in arrays as following

vertex_blk(IC,SN,BN)	the adjacent block number.
vertex_ik(IC,SN,BN)	index number of interpolation stencil in ξ direction of the adjacent block
vertex_jk(IC,SN,BN)	index number of interpolation stencil in η direction of the adjacent block
vertex_coef(1:2,IC,SN,BN)	coefficients for linear interpolation between grid vertices of the adjacent and the current block.

In these arrays, the integer IC is the index number of the grid along the side 3 of block 1; the integer SN is the side number of block 1 (in this example, SN is equal to 3); and the integer BN is the current block number. Therefore, for any grid point at the interface of the current block, the necessary information for interpolation is obtained by a series intersection tests. The same procedure can be applied to other three boundary sides. For steady grid

computation, these intersection tests need to be done only once, the result is stored in the arrays for later use.

4.2.2 Grid Face Center Based Interpolation

Grid face center (or edge) based interpolation can be implemented in the similar manner as grid vertex based interpolation. However, one more step is needed. The line segments are formed by connecting the grid face center points instead of by connecting the the grid vertices, then intersect tests are conducted. The output information is stored in four arrays

edge_blk(IC,SN,BN)	the adjacent block number.
edge_ik(IC,SN,BN)	index number of interpolation stencil in ξ direction of the adjacent block
edge_jk(IC,SN,BN)	index number of interpolation stencil in η direction of the adjacent block
edge_coef(1:2,IC,SN,BN)	coefficients for linear interpolation between grid face center of the adjacent and the current block.

The definitions of the integer IC, SN and BN for the edge based interpolation are similar to those for the vertex based interpolation.

The interpolation procedures above can be described by the following pseudo-code:

```
for BN=1, .....Nblock
  for SN=1, .....4 do
    for sgn=1, ..... Nsegment
      if the segment is a interface do
          intersection_test
      endif
```

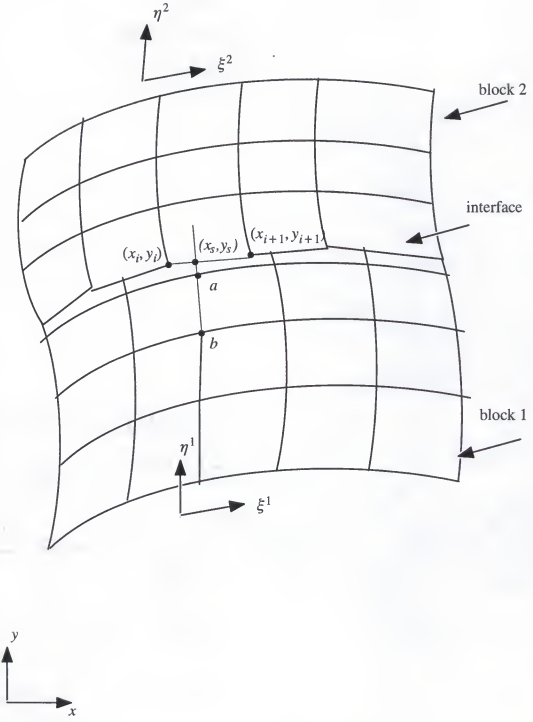

Fig. 4.3 Grid vertex based interpolation

```
        endfor
      endfor
    endfor
```

The subroutine intersection_test can be described as

```
    for i=Indexc1, .....Indexc2
      for j=1, .....Jmax do
        solve linear equations of two line segment
          if intersection point found do
              get the index numbers of the grid cell in the adjacent block
              get the interpolation coefficients
          endif
        endfor
    endfor
```

In the above procedure, Nblock is the total block number, Nsegment is the total segment number at a boundary side, and Jmax is the total grid number of adjacent block side. Indexc1 and Indexc2 are the starting and ending indices of an interface segment respectively.

4.3 Interpolation with Local Conservative Correction

In this section, the implementation and data structure of interpolation with local conservative correction will be described. We combine an explanation in words with a brief section of pseudo-code. Again, suppose there are two grid blocks. Side 3 of block 1 is patched with side 1 of block 2, as indicated in Fig. 4.3. For simplicity, the grid layers adjacent to the interface are isolated out for illustration, and are shown in Cartesian grid, as shown in Fig. 4.4. In the current configuration, the relative position between the two blocks are very general, i.e., there is no distinction of coarse or fine grid block. Basically, the whole procedure can be broken into three steps: grid cell split, flux interpolation and flux correction.

Fig. 4.5 The general interface configuration between two blocks.

4.3.1 Grid Cell Split

The first step is to split the grid cells of block 1 into a number of subcells by grid lines of block 2, so that each grid cell in block 2 matches integer number of subcells in block 1, as illustrated in Fig. 4.6. The method of interpolating flux with local conservative correction, which is described in section 3.5.4, can be conducted based on every grid cell flux at the interface of block 2. The output of the first step is to give the relation between every grid cell (named as parent cell) at interface of block 1 and the corresponding split subcells (named as child cells). A parent cell is identified by the index number along the interface, the side number and the current block number. A child cell is identified by the corresponding parent cell identification, a index number indicating the sequence number of the child cell in the parent cell and x, y coordinates of the starting and ending points of the child cell. This relation is shown in Fig. 4.7. The output information is stored in the following three arrays

number_child(IC,SN,BN)	total number of child cell plus 1, in a parent cell
x_child(ICELL,IC,SN,BN)	x-coordinate of the starting point of a child cell

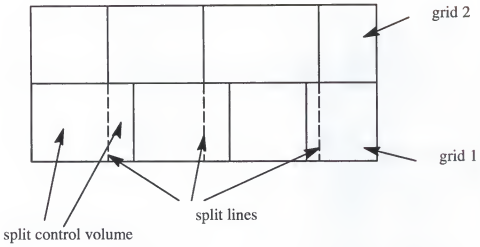

Fig. 4.6 The configuration of split cells at a grid interface.

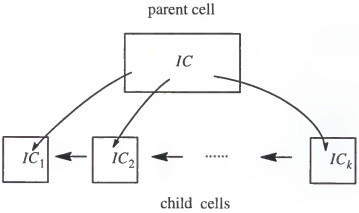

Fig. 4.7 The mapping between a parent cell and the child cells

y_child(ICELL,IC,SN,BN) y-coordinate of the starting point of a child cell

Here, the integer IC is the index number of parent cell along the interface of the current block; the integer SN is the side number of the interface; and the integer BN is the current block number. The integer ICELL is the index number of the sequence of the child cell in the parent cell.

The split procedure above is completed by conducting intersection tests. This procedure can be described by the following pseudo-code:

```
for BN=1, .....Nblock
  for SN=1, .....4 do
    for sgn=1, ..... Nsegment
      if the segment is a interface do
          subroutine split-cell
      endif
    endfor
  endfor
endfor
```

The subroutine split-cell can be described as

```
for i=Indexc1, .....Indexc2
  initialize number_child(i,SN,BN)=0
  for j=1, .....Jmax do
    intersection test
      if the intersection point found do
          increase number_child(i,SN,BN) by 1,
          ICELL=number_child(i,SN,BN)
          get x_child(ICELL,i,SN,BN), y_child(ICELL,i,SN,BN)
```

```
        endif
      endfor
    endfor
```

In the above procedure, Nblock is the total block number, Nsegment is the total segment number at a boundary side, and Jmax is the total grid number of adjacent block side. Indexc1 and Indexc2 are the starting and ending indices of an interface segment respectively.

4.3.2 Flux Interpolation

The second step is to interpolate fluxes from the grid cells at the interface of adjacent block (block 2) to the child cells at the interface of the current block (block 1). For mass flux transfer, this is basically a grid face center to grid face center interpolation, as described by the previous section on interpolation. For each child cell, the relevant information about interpolation is stored in the following arrays

flux_bk(ICELL,IC,SN,BN)	the adjacent block number
flux_ik(ICELL,IC,SN,BN)	index number of interpolation stencil in ξ direction of the adjacent block
flux_jk(ICELL,IC,SN,BN)	index number of interpolation stencil in η direction of the adjacent block
flux_coef(1:2,ICELL,IC,SN,BN)	flux interpolation coefficients for interpolation between the grid face center of the adjacent block and the child cell center of the current block.

Here, the integers IC, SN and BN are defined the same as in the vertex based interpolation information arrays. The integer ICELL is the child cell index in the corresponding parent cell. With above information, The flux for each child cell can be obtained by interpolating fluxes of grid cells at the interface of the adjacent block. But the interpolated flux is not

strictly conserved either on the local cell by cell basis or global interface basis, it is only used as the first approximation. The extent of flux conservation relies on the interpolation formula employed. Next, a correction step is introduced to conserve the flux strictly.

4.3.3 Local Flux Correction

The third step is to make a conservative correction of flux based on the first approximation in the second step, and on the scale of each individual grid cell at the interface of adjacent block (block 2). After the cell split step, a grid cell at the interface of adjacent block matches a integer number of child cells of current block. The interpolated flux at each corresponding child cell can be scaled according to the magnitude of the first approximation, so that the total flux from the child cells are equal to flux of grid cell of adjacent block exactly, as indicated in section 3.5.4. The remaining question is how to identify the correspondence between a grid cell at the interface of adjacent block and the matching child cells in the current block (block 1). With the cell split step, the relation between a parent cell in current block and the corresponding child cells are uniquely determined, but a grid cell in adjacent block may include child cells from several different parent cells of current block, as shown in Fig. 4.8. The procedure to set up this unknown correspondence will be described below.

In the current block, for each interface segment (called current segment)at a boundary side, the corresponding interface segment in the adjacent block, the starting and ending indices along that interface segment (called adjacent segment) are identified first. This identification process can be accomplished by the intersection test, and the following information are provided

seg_bk(ISG,SN,BN)	the adjacent block number.
seg_start(ISG,SN,BN)	starting index number along the interface segment in the adjacent block
seg_end(ISG,SN,BN)	ending index number along the interface segment in the adjacent block.

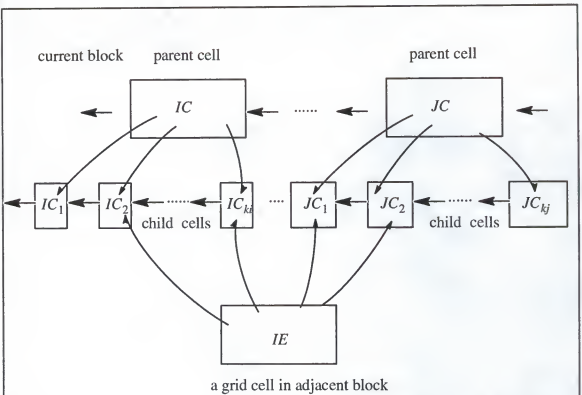

Fig. 4.8 The mapping between a parent cell and the child cells in the current block, and the mapping between the child cells and a grid cell in adjacent block.

seg_side(ISG,SN,BN) side index number of the interface segment in the adjacent block.

Here, the integer BN is the current block number, SN is the side number of the current block, and ISG is the segment number of the interface segment in that side.

Then, beginning at the starting grid cell in the adjacent segment, for each grid cell, a counting procedure is conducted to calculate the number of corresponding child cells in current segment, This counting procedure is based on another intersection test, i.e., the intersection test between the line segment of the grid cell in the adjacent block along the interface direction and the line segment connecting the child cell face centers in current block other than the interface direction. If the intersection point between the two line segments is identified, the child cell is found belong to the grid cell in adjacent segment, and is added

to that grid cell list. A particular array is created to stored this information

number_cell(IE,SE,BE)	the number of child cells included in a grid cell in adjacent segment

Here, the integer BE is the adjacent block number, SE is the side number of the adjacent block, and the integer IE is the grid cell index number at the interface of adjacent block. The integer array number_cell determines the number of child cells each grid cell in the adjacent segment matches.

After the counting procedure, the child cells in the current segment can be put into a one dimensional array based on the relative sequence of each child cell in the parent cell and the index sequence of the parent cells in the current segment. With this child cells sequence in current segment, the grid cell sequence in the adjacent segment and the correspondence between the two segments, the correspondence between the each grid cell in the adjacent segment and the child cells in the current segment can be uniquely determined, i.e., each grid cell in the adjacent segment matches integer number of child cells in the current segment. Therefore, the conservative correction of flux for each child cell can be made accordingly. Based on this correction, the flux is strictly conserved between each grid cell in adjacent segment and the corresponding child cells, and the flux distribution is close to that determined by the interpolation method chosen. Finally, after the correction, the fluxes in the child cells are merged back to the parent cell in the current segment, and the flux distribution along the interface is uniquely determined.

4.4 Concluding Remarks

In this chapter, the data structures for the multi-block interface treatment are devised. Basically, the tasks of the information transfer between discontinuous grid interfaces of different blocks can be divided into two categories: (1) interpolation between grid vertices

or grid face centers, and (2) interpolation with conservative correction for fluxes between grid faces. The most fundamental operation behind these two tasks is the intersection test among arbitrary oriented line segments in two-dimensional space. With the very simple input, the connectivity among grid blocks, grid boundaries, boundary segments and control volumes at grid interfaces can be set up automatically, based on the line segment intersection test. The related information is stored in a series of arrays for later use.

CHAPTER 5
ASSESSMENT OF THE INTERFACE TREATMENTS

5.1 Assessments of Conservative Treatments in the N-N Boundary Condition for the Pressure Correction Equation

In this section, the conservative and non-conservative treatments of mass flux with different accuracies are tested and compared. The test problem is the lid-driven cavity flow problem with Re=1000. First, a 3-block discontinuous Cartesian grid configuration with different grid resolutions is used. A grid system of 41x21, 81x13 and 41x11 grid points for block 1, 2 and 3 respectively, as shown in Fig. 5.1, is first employed. Here, the interface between block 1 and 2 coincides with the cavity horizontal center line. The second grid system doubles the grid resolutions of the first grid system, and has 81x41, 161x23 and 81x21 grid points in each block, respectively. The third grid system doubles the grid resolution in x direction of the second grid system and has 161x41, 321x23 and 161x21 grid points in three blocks. To clarify the terminology, the multi-block grid for the whole flow domain is called "grid system" here. Each grid system consist of several blocks. The first grid system described above is denoted as the coarse grid system, the second as the median grid system, and the third as the fine grid system. The three grid systems share the same topological characteristics in each block. We have created these three grid systems to investigate the interplay of interface treatment and overall grid resolutions. The grid layouts are not ideally suitable for the present recirculating flow, they are purposely set up to test the relative merits of different interface treatments. For all the test cases presented in this section, the second order central difference is used for convection, diffusion and pressure terms. Furthermore, the Neumann-Neumann interface condition is employed in all the cases

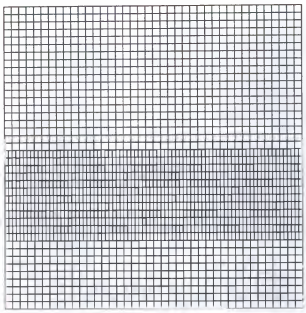

Fig. 5.1 Three-block grid with 41x21, 81x13 and 41x11 nodes for block 1, 2 and 3, respectively.

studied in this subsection. The Dirichlet-Neumann and Dirichlet-Dirichlet conditions will be investigated in next section.

Case 1. The Cartesian velocity components u and v and the contravariant velocity components U and V are linearly interpolated at the grid interfaces. Total momentum fluxes across the interfaces are conserved via the pressure adjustment. No mass conservation is enforced across the grid interfaces. The computations are conducted over the coarse, median and fine grid systems. For all three grid systems, the normalized residuals for u and v momentums are below 10^{-4}. The normalized mass residuals reach down to $1.5\text{x}10^{-3}$, $3.3\text{x}10^{-4}$ and $1.3\text{x}10^{-4}$ for the coarse, median and fine grid systems, respectively, and stabilize at those levels. Figures 5.2a and 5.2b show the u-component distributions along the vertical center line and v-component distributions along the horizontal center line. They are compared with the corresponding benchmark solution reported by Ghia et al. (1982). It can

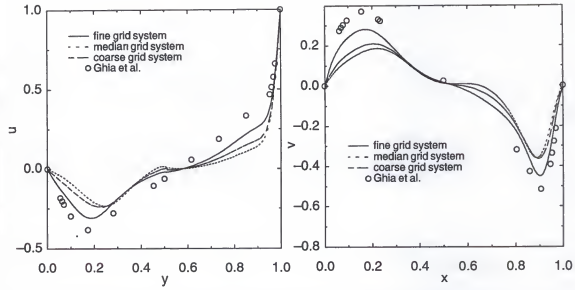

(a) u velocity along the vertical center line (b) v velocity along the horizontal center line

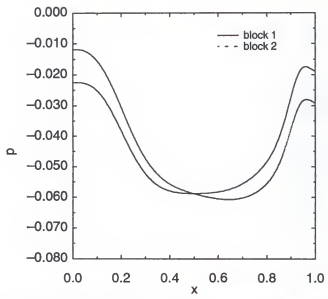

(c) pressure distribution at the interface between block 1 and 2 on the fine grid system.

Fig. 5.2 Solution profiles based on linear interpolation for U and V without mass conservation correction.

be seen that the solutions for all the three grid systems have substantial discrepancies with respect to the benchmark values. Although in general, the solutions improve as the grids are refined, the overall performance of all three systems are unsatisfactory. It is noted that for this problems computed with single grid distributed uniformly, a 81x81 grid system can yield very accurate solution already (Shyy et al. 1992). Accordingly, it is unsatisfactory to observe that both median and fine grid systems, even with resolutions better that 81x81 single uniform grid, still do not yield accurate solutions. Figure 5.2c shows the interface pressure distributions computed on block 1 and 2. The pressure in each block has been adjusted according to the total momentum balance at the interface. The absolute value of the pressure has no practical meaning. For a well converged solution, the pressures form different blocks are expected to have the same distributions at the interface; in the current case, even with fine grid system, the discrepancy between the two pressure distributions is obvious.

Case 2. Both the Cartesian velocity components u and v and the contravariant velocity components U and V are quadratically interpolated, But still without enforcing mass conservation. This procedure is of higher interpolation accuracy than that in case 1, however, neither has conservative treatment. The motivation here is to test the role played by the interpolation accuracy, and to investigate that for viscous flow, whether conservative treatment is necessary to obtain satisfactory solutions. For all three grid systems, the residuals for momentum equations are below 10^{-4}. The mass residuals stabilize at the level of $2.3\text{x}10^{-3}$, $4.3\text{x}10^{-4}$ and $7.5\text{x}10^{-5}$ for the coarse, median and fine grid systems, respectively. Figures 5.3a and 5.3b show the u-component and v-component distributions respectively for the three grid systems. Overall, these solutions are improved compared to the solutions shown in Fig. 5.2, and the solution on the fine grid system shows obvious improvement over the coarse and median grid systems solutions. However, discrepancies still exist between the present and the benchmark solutions. Figure 5.3c shows the pressure distributions at the interface of block 1 and 2. The discrepancies between the two distributions till exist. From cases 1 and 2, it can be seen that the solution can be improved

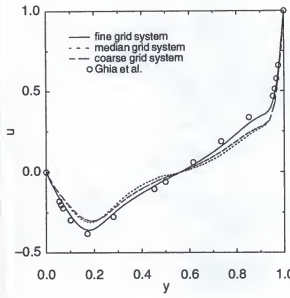

(a) u velocity along the vertical center line.

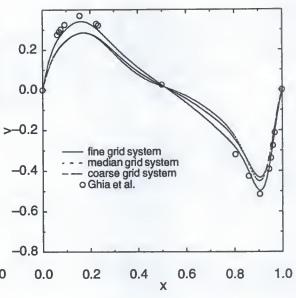

(b) v velocity along the horizontal center line.

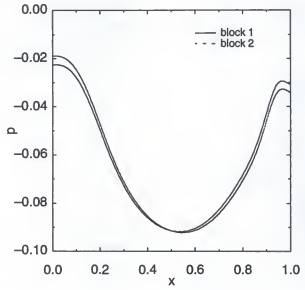

(c) pressure distribution at the interface between block 1 and 2 on the fine grid system

Fig.5.3 Solution profiles based on quadratic interpolation for U and V without mass conservation correction.

with the grid refinement. The overall solution accuracy is better with the quadratic interface interpolation than that with linear interpolation, which is expected because the quadratic interpolation increases the order of interpolation accuracy and should reduce the non-conservative error for mass flux across the grid interfaces. However, even with the fine grid system, the solution of quadratic interpolation is still not satisfactory. Because with both interpolations, the solutions are not as accurate as the single grid result. it appears that a non-conservative interface treatment for mass flux is not satisfactory when complex flow structures, such as recirculation, are present.

Case 3. Because the non-conservative linear and quadratic interpolations for the contravariant velocities cannot lead to a satisfactory solutions even for a very fine grid, a conservative interface is then tested. In this case, the Cartesian velocity components u and v are linearly interpolated. The contravariant velocities U and V are linearly interpolated first, followed by a global correction procedure for mass flux as discussed previously. The computation is conducted for the coarse grid system only. The momentum and mass flux residuals reach to the level of 10^{-5}. The results are shown in Fig. 5.4. Obviously, the solutions are not satisfactory. It appears that the conservative interface treatment conducted at the global level can not yield the correct solution either.

Case 4. The Cartesian velocity components u and v are still linearly interpolated. The contravariant velocities U and V are interpolated based in the piecewise constant formula, which by nature is locally conservative with first order accuracy. This treatment is implemented to investigate the effect of the local conservation on the solution. The computations are computed for the three grid systems. For the coarse and median grid systems, the residuals for the momentum and mass fluxes reach down to 10^{-5}. However, for the fine grid, the converged solution can not be obtained. Figures 5.5a and 5.5b present the u and v component distributions for the coarse and median grids. Both u and v profiles agree well with the benchmark solutions. Figures 5.5c and 5.5d exhibit the pressure distributions at the interfaces of block 1 and 2 for two grid systems. The pressures in the interface region

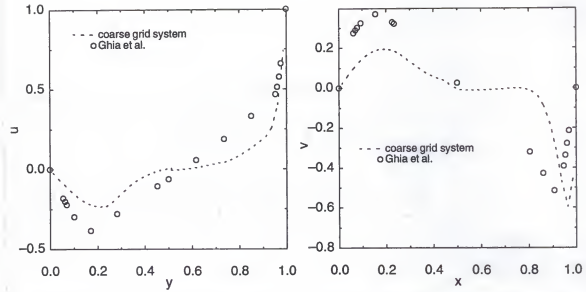

(a) u velocity along the vertical center line (b) v velocity along the horizontal center line.

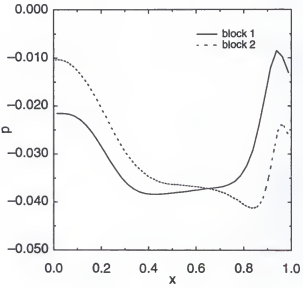

(c) pressure distribution at the interface between block 1 and 2 on the coarse grid system

Fig. 5.4 Solution profiles based on linear interpolation with global correction of mass conservation for U and V on the coarse grid system.

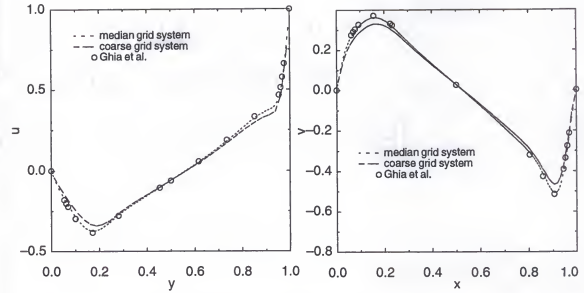

(a) u velocity along the vertical center line. (b) v velocity along the horizontal center line

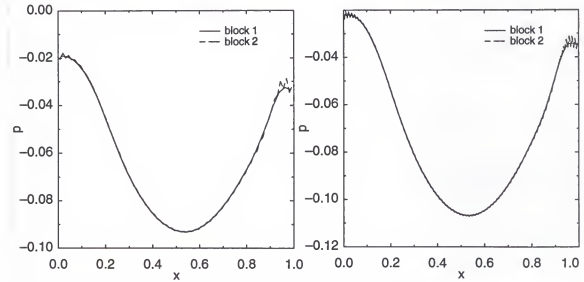

(c) pressure distribution at the interface between block 1 and 2 on the coarse grid system.

(d) pressure distribution at the interface between block 1 and 2 on the median grid system.

Fig. 5.5 Solution profiles based on piecewise constant interpolation for U and V.

obtained on different blocks conform each other generally well, except that some oscillations appear on block 2. The cause of this nonphysical oscillation comes from the fact that the mass flux distributions at the fine grid interface are assigned according to the piecewise constant formula. This distribution results in a series of stair-step mass profile at the interface of fine block, forcing the pressure field to oscillate in response to the non-smooth mass flux distribution. This same reason is also probably responsible for the nonconvergence of the fine grid solution.

Case 5. The Cartesian velocity components u and v are linearly interpolated. The contravariant velocities U and V are linearly interpolated first, followed by a local correction to maintain the cell by cell mass conservation across the interfaces. The tests are conducted for all three grid systems. The residuals for mass and momentum fluxes reach below the level of 10^{-5}. Figures 5.6a and 5.6b show the u and v component distributions. The solution on the coarse grid system shows a very small discrepancy compared to the benchmark solution; the solution on the median and fine grid systems agree well with the benchmark solution. Figure 5.6c displays the pressure distributions at the interface of block 1 and 2 on the fine grid system. The two pressure profiles conform to each other very well. Clearly, a treatment of interface mass flux with local conservation and certain accuracy holds a key to produce a accurate solution.

Case 6. The Cartesian velocity components u and v are quadratically interpolated. The contravariant velocities U and V are quadratically interpolated first, followed by a local correction to maintain the cell by cell mass conservation across the interfaces. Again, the computations are conducted for the three grid systems and residuals reach go down to 10^{-5}. Figures 5.7a and 5.7b show the u and v component distributions. Good agreements, comparable to Case 5 (Fig. 5.6) between the current solutions and benchmark solutions are observed. Figure 5.7c presents the pressure distributions at the interface of block 1 and 2 on the fine grid system. The pressure distributions also conform to each other very well. For the present flow problem, both the linear and quadratic interpolations with local correction

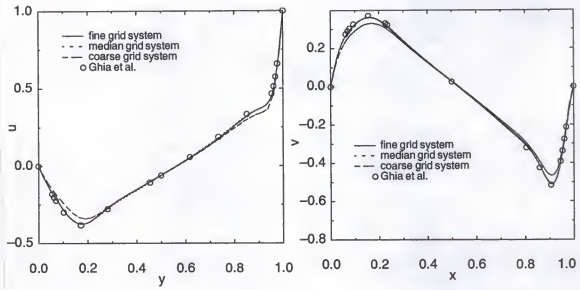

(a) u velocity along the vertical center line.(b) v velocity along the horizontal center line.

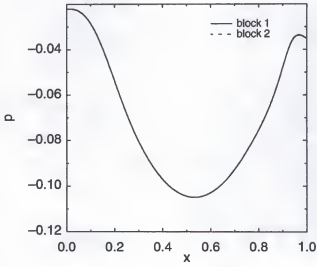

(c) pressure distribution at the interface between block 1 and 2 on the fine grid system.

Fig. 5.6 Solution profiles based on linear interpolation with local correction of mass conservation for U and V.

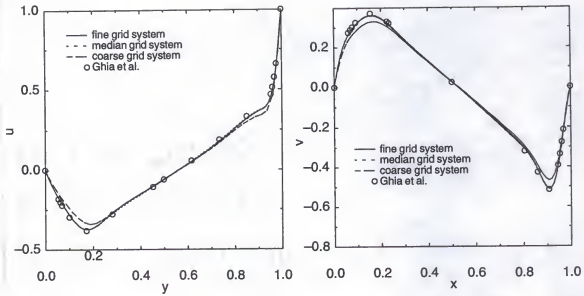

(a) u velocity along the vertical center line. (b) v velocity along the horizontal center line.

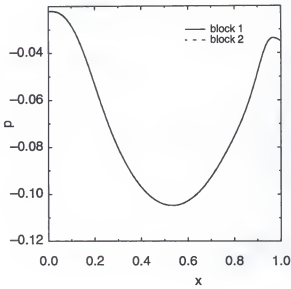

(c) pressure distribution at the interface between block 1 and 2 on the fine grid system.

Fig. 5.7 Solution profiles based on quadratic interpolation with local correction of mas conservation for U and V

give the accurate solutions. Since the discretization scheme for the interior nodes are second order accurate, it appears that a linear interpolation (aided by the local conservative correction) treatment is sufficient.

Case 7. Finally the same flow problem is investigated with a 3-block curvilinear grid, which has 81x41, 161x23 and 81x21 grid points for block 1, 2 and 3, respectively, as shown in Fig. 5.8. The interface treatment is the same as that in Case 5, and the momentum and mass residuals reach down to 10^{-5}. Figure 5.9 demonstrates the u component distribution at the vertical center line and compares it with the corresponding benchmark solution. Good agreement is observed, which illustrates the capability of the current interface treatment on curvilinear grid systems.

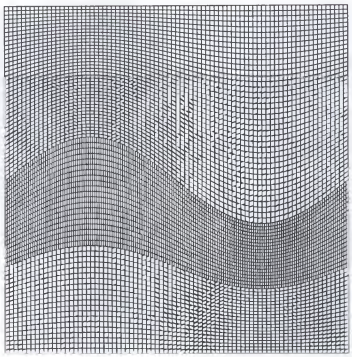

Fig. 5.8 Three-block curvilinear grid with 81x41,161x23 and 81x21 nodes for block 1,2 and 3, respectively.

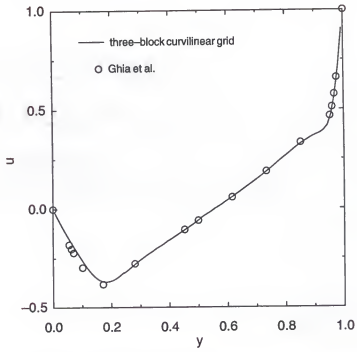

Fig. 5.9 The u velocity along the vertical center line. Linear interpolation with local correction of mass conservation for U and V.

5.2 Comparison of Two Different Interface Conditions for the Pressure Correction Equation

In this section, the N-N and D-N type interfaces for the pressure correction are compared. The lid-driven cavity flow with Re=1000 is still used as the test case, with the flow domain partitioned into two discontinuous grid block at the cavity horizontal center line. A grid system of 65x33 and 61x34 nodes is used for block1 and block 2, respectively, as shown in Fig. 5.10. There is one grid layer overlap between the two blocks. The mass flux at the interface is estimated based on piecewise linear interpolation with local conservative correction.

Figures 5.11a and 5.11b show the u-profile along the vertical center line and v-profile along the horizontal center line for both interface methods on the overlapping grid;

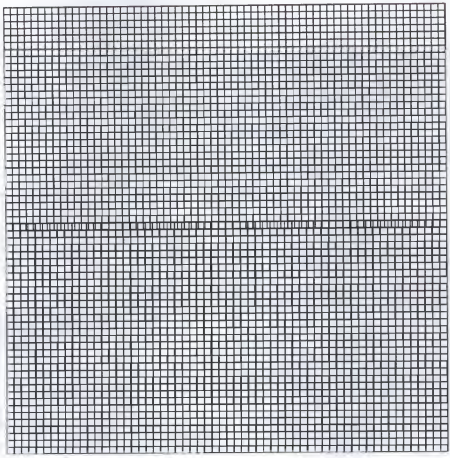

Fig. 5.10 Two block overlapping grid with 65x33 and 61x34 nodes in each block

they are compared with the corresponding benchmark solution reported by Ghia et al. (1982). The pressure distributions from the two methods are shown in Fig. 5.11c. It can be seen that the solutions produced by both methods are almost identical and conform very well with the benchmark solution. It is also noted that the discontinuous interface at the horizontal center line has no noticeable effect on the solutions.

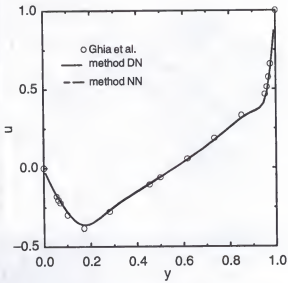

(a) The u velocity along the vertical center line

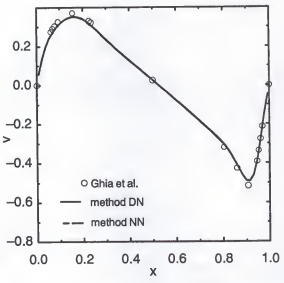

(b) The v velocity along the horizontal center line

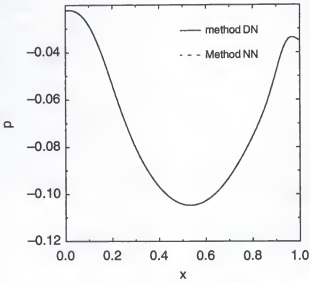

(c) The pressure distributions at the interface

Fig. 5.11 Comparison of two interface treatments on cavity flow calculations with $Re=10^3$. (The two interface treatments result in indistinguishable solutions).

For both methods, under-relaxation is needed to make the algorithm converge. For the method NN, the values of 0.3 and 0.5 for the momentum equations and pressure correction equation are found to yield an adequate convergence rate. For the method DN, the values of 0.3 and 0.1 for the momentum equations and pressure equation are required to obtain a converged solution. Figure 5.12 compares the convergence rates of the two methods with the relaxation factors stated above. The normalized mass residual is used as a representative quantity. The method DN appears converge faster than the method NN, although it seems to have a more restrictive stability bound.

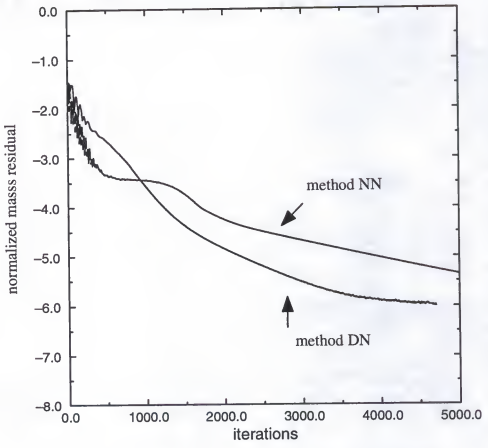

Fig. 5.12 Comparison of convergence paths between the two interface methods: DN and NN

It is noted that for the DN interface treatment, if the mass flux at the interface is interpolated without local conservative correction, the solution obtained is unsatisfactory. In addition to the methods DN and NN, the DD interface treatment for the pressure correction equation, i. e., p' is interpolated at both sides as the interface boundary condition, is also tested. For the test case above, it is found that this interface treatment can not yield a satisfactory solution.

5.3 Simulations of the Hydraulic Turbine Distributor Flows

A distributor is a circular component in a hydraulic turbine consisting of multiple pairs of airfoils which directs the flow from a spiral casing downward into a runner which drives a shift producing useable power output. An illustration of the hydraulic turbine considered here can be found in Shyy (1994). Because of the strong coupling between the spiral casing and distributor flow, the flow in a combined spiral casing and distributor is difficult to model and predict. Instead, a two-level modeling approach is proposed by Shyy and Vu (1993) to simulate the spiral casing flow with the effect of distributor. While a distributor is naturally a three-dimensional component, a two-dimensional section of the distributor between a single passage bounded by airfoils above and below can represent the overall flow characteristics. In this section, the advantages of multi-block computational method and concept are illustrated through the distributor flow simulations. Two distributor configurations are considered.

5.3.1 Case A: 5 Blades

With this configuration, a single periodic sector consists of two fixed stay vanes (first row of airfoils) and three pivoting wicket gates (second row of airfoils). Figure 5.13 shows the flow domain and the grid of two consecutive periodic sectors. In the actual computation, only one periodic sector is computed. For a single passage, to accommodate the three wicket gates, the flow domain consists of two blocks (86x23 and 86x23 nodes), each of those is between a pair of wicket gates. the grid interfaces are continuous in the case. For the upper

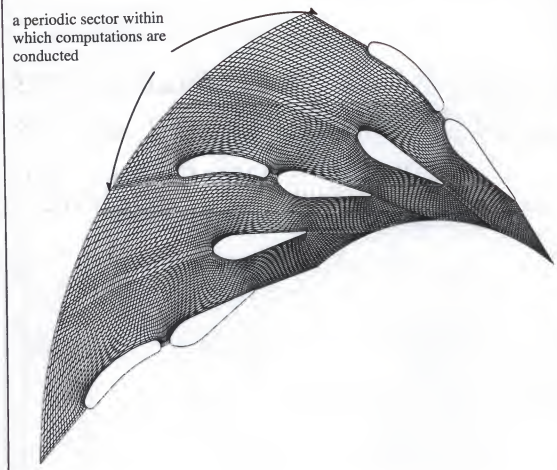

Fig 5.13 Distributor A: The two block grid with 86x23 nodes in each block. Shown here are two consecutive periodic sectors.

and lower boundaries, the periodic boundaries are alternated with the solid walls representing the stay vane and wicket gate. It is noted that, due to the non-parallel arrangement between two consecutive blades, the periodic condition needs to be applied with the consideration of coordinate rotation.

The present two-dimensional flow analysis is based on the full Reynolds-averaged Navier-Stokes equations. The Reynolds number based on the inlet flow condition is 10^6. The original K-ε two-equation turbulence model is adopted here as the closure form (Launder and Spalding 1974). As to the discretization, second order central difference schemes are

applied to all derivatives except convection terms, which are treated by the second order upwind scheme (Shyy 1994, Shyy et al. 1992, Thakur and Shyy 1993). At the inlet of the flow domain, a uniform flow distribution is assigned with a given flow angle, which is measured relative to the tangent of the circle defining the locations of the leading edge of the stay vanes. For the present case, the flow analyses are performed at the inlet flow angle of 20 and 30 degrees. At the exit, zero first-order derivative along the streamwise direction is taken for all dependent variables, except for static pressure which is regulated by the exit mass flux condition. At the nodal position next to the solid wall, the wall function treatment is applied (Launder and Spalding 1974). The solution is considered to have converged when the sum of the momentum and mass residuals, normalized by the inlet momentum and mass fluxes respectively, is below 10^{-4}. The streamline is presented in Figure 5.14. At 20 degree inlet flow angle, flow separates at the upper surface of stay vane; while at 30 degree inlet flow angle, no separation happens. Figure 5.15 shows the corresponding pressure distributions. In both cases, substantial fluids flow across the periodic boundary, requiring a careful treatment there.

5.3.2 Case B: 4 Blades

With this configuration, a single periodic sector consists of two fixed stay vanes and two wicket gates. Figure 5.16 shows the flow domain and the grid (142x23 nodes for a single sector). Again, two sectors are stacked together to help visualize the periodic boundaries. For the present domain, a single block grid with continuous periodic boundary condition is found to be fairly skewed throughout a majority of the domain, because grid lines along the bottom boundary proceed directly to their corresponding points on the top boundary. Instead, a single block grid with the discontinuous grid distribution across the periodic boundary is adopted, as illustrated in Figure 5.16. At the first pair of periodic boundary, the grid spacings on the two sides of the interface are of ratio of a 2:1, with the upper boundary acting as the fine grid interface. At the second periodic boundary the grid is continuous, and at the third periodic boundary, the grid spacings on the two sides of the interface are of a ratio of 1:2 with

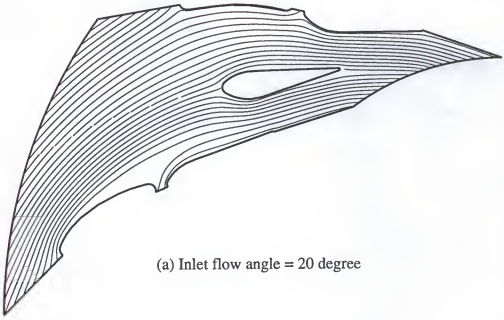

(a) Inlet flow angle = 20 degree

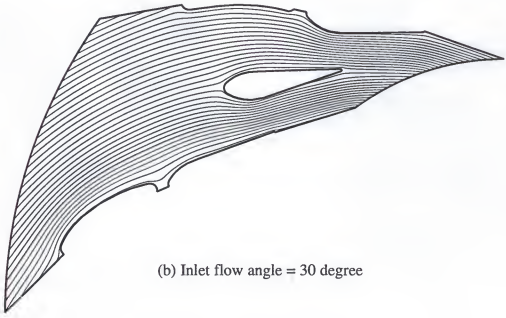

(b) Inlet flow angle = 30 degree

Fig. 5.14 Streamline patterns for two inlet flow angles within a periodic sector.

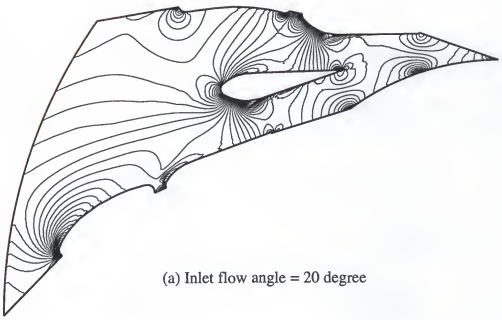

(a) Inlet flow angle = 20 degree

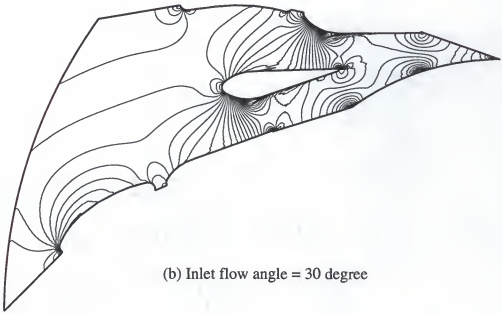

(b) Inlet flow angle = 30 degree

Fig. 5.15 Pressure fields for two inlet flow angles within a periodic sector.

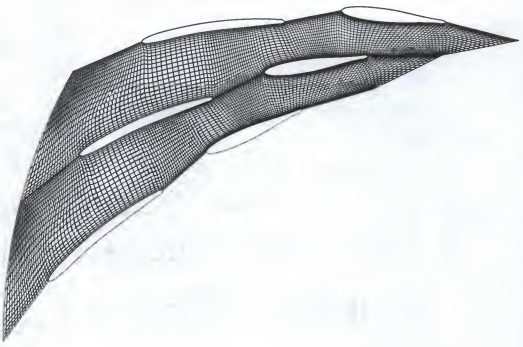

Fig. 5.16 Distributor B: Single block grid with discontinuous periodic boundaries. Two periodic sectors are shown here.

the lower boundary acting as the fine grid interface. The periodic boundaries are treated as non-overlapping discontinuous grid interfaces. It can be seen that, with introduction of the discontinuous grid interface, the grid skewness is greatly reduced for this type of domain consisting of a staggered array of airfoils. In this case, the incoming flow condition is similar to that in case A. The flow analyses are also performed for the inlet flow angle of 20 and 30 degrees. When the convergence is reached, both the normalized momentum and mass residuals are below 10^{-4}, showing that the discontinuous grid interface treatment is successful. The corresponding streamline and pressure distributions are shown in Fig. 5.17 and 5.18, respectively.

5.4 Concluding Remarks

In this chapter, the interface conditions and the data structures proposed in the previous two chapters are investigated through the numerical experiments. For the momentum equations, the dependent variables are interpolated between grid blocks by bilinear or quadratic interpolation. For the pressure correction equation, three interface treatments are investigated. It is found that with the local conservative interface mass flux treatment with certain degree of accuracy, both the Neumann-Neumann and Neumann-Dirichlet type boundary conditions can yield satisfied solutions. Compared to the Neumann-Neumann type boundary condition, the mixed Neumann-Dirichlet type boundary condition allows better pressure coupling between grid blocks. For the cases tested, both boundary treatments give very comparable accuracy. A linear interpolation with local conservative correction method is found satisfactory for communicating mass flux across an interface. The applications of the multi-block method are shown through the simulations of the hydraulic turbine distributor flows.

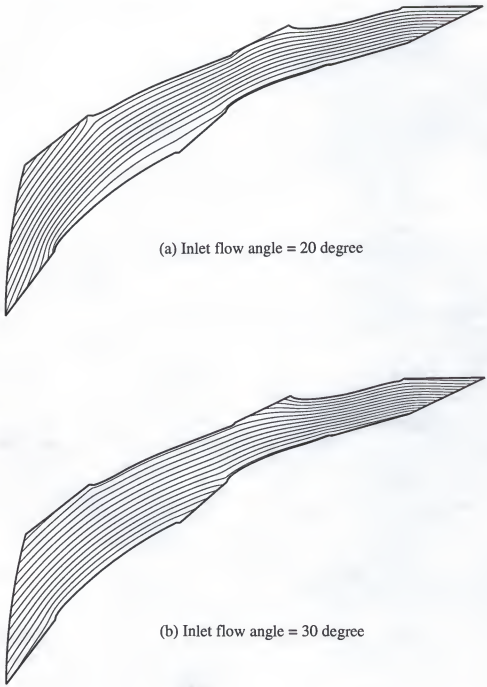

Fig. 5.17 Streamline patterns for two inlet flow angles within a periodic sector.

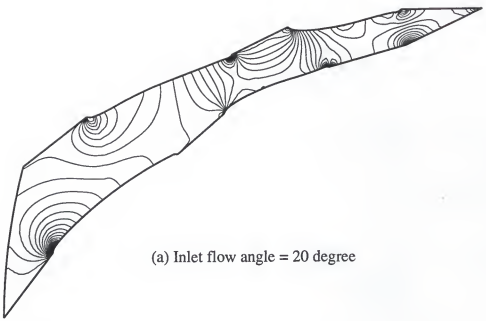

(a) Inlet flow angle = 20 degree

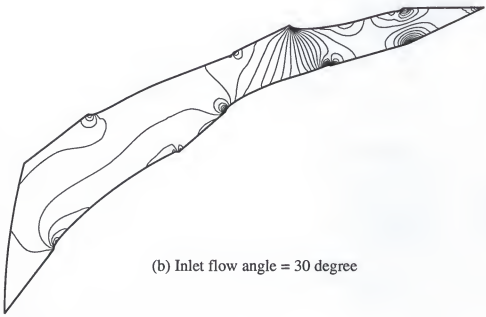

(b) Inlet flow angle = 30 degree

Fig. 5.18 Pressure fields for two inlet flow angles within a periodic sector.

CHAPTER 6
TWO-EQUATION TURBULENCE MODELING WITH NON-EQUILIBRIUM EFFECT

6.1 Background

To perform practical turbulent flow calculations at high Reynolds numbers, it is often convenient to use the Reynolds averaged Navier-Stokes equations

$$\varrho\frac{\partial\overline{u}_i}{\partial t}+\varrho\frac{\partial}{\partial x_j}(\overline{u}_i\overline{u}_j)=-\frac{\partial p}{\partial x_i}+\frac{\partial}{\partial x_j}(2\mu S_{ij}-\varrho\overline{u_i'u_j'}) \tag{6.1}$$

$$\frac{\partial\varrho}{\partial t}+\frac{\partial}{\partial x_i}(\varrho\overline{u}_i)=0 \tag{6.2}$$

$$S_{ij}=\frac{1}{2}(\frac{\partial\overline{u}_i}{\partial x_j}+\frac{\partial\overline{u}_j}{\partial x_i}) \tag{6.3}$$

These equations are obtained by decomposing the dependent variables into mean and fluctuating parts ($u=\overline{u}+u'$), then conducting averaging of the Navier-Stokes equations. This procedure introduces new unknowns, i.e., the so called Reynolds-stress tensor terms, $-\varrho\overline{u_i'u_j'}$, which can be denoted by τ_{ij}, namely,

$$\tau_{ij}=-\varrho\overline{u_i'u_j'} \tag{6.4}$$

By inspection, $\tau_{ij}=\tau_{ji}$, so that this is a symmetric tensor, and thus has six independent components. For general three-dimensional constant property flows, we have four mean flow properties, i.e., pressure and three velocity components. Along with the six Reynolds-stress components, we thus have ten unknowns. To close the system of the governing equations, the Reynolds-stress components have to be modeled.

One of the earliest proposals for modeling the Reynolds-stresses is Boussinesq's eddy-viscosity concept which assumes that the turbulent stresses are proportional to the mean flow velocity gradients(Schlichting 1979). This relation can be expressed as

$$\overline{u_i' u_j'} = \frac{2}{3} K\delta_{ij} - \nu_t\left(\frac{\partial \overline{u}_i}{\partial x_j} + \frac{\partial \overline{u}_j}{\partial x_i}\right) \tag{6.5}$$

where K is the turbulent kinetic energy, δ_{ij} is the Kronecker delta, and ν_t is the eddy viscosity. With this assumption, the task of finding the Reynolds-stresses reduces to the determination of the eddy viscosity. The eddy viscosity can be written as

$$\nu_t = \frac{l_0^2}{t_0} \tag{6.6}$$

where l_0 is the turbulent length scale and t_0 is the turbulent time scale-quantities which can vary dramatically in space and time for a given turbulent flow.

The simplest of all turbulence models are known as algebraic models or zero-equation models, in which both l_0 and t_0 are specified algebraically by empirical means. The first useful zero-equation model for computing the eddy viscosity was Prandtl's mixing length theory. In Prandtl's mixing length theory for a wall-bounded non-separating shear flow(Schlichting 1979),

$$\nu_t = l_0^2 \left|\frac{d\overline{u}}{dy}\right| \tag{6.7}$$

where $l_0 = \varkappa y$ is the mixing length, $\varkappa$ is the von Karman constant, and y is the normal distance from a solid boundary. This representation is only formally valid for thin turbulent shear flows near a wall, where the mean velocity is unidirectional. This simple mixing length model has been generalized to multi-dimensional turbulent flows with tensorially invariant forms (Cebeci and Smith 1974, Baldwin and Lomax 1978) and applied to a wide variety of flows. However, the zero-equation models suffer from the deficiency in their need for a specification of the turbulent length scale l_0, a very difficult, if not impossible, task for complex turbulent flows.

Beyond the length scale specification problem with zero-equation models, there is another criticism that, it is not physically consistent to construct the turbulent velocity scale from the mean velocity gradients as expressed in Eq. (6.7). The proper measure of the turbulent velocity scale is the intensity of the turbulent fluctuations (i.e., we should take $u_0 = K^{1/2}$, where $u_0 = l_0/t_0$) Hence, a more physically consistent representation for the eddy viscosity is given by

$$\nu_t = K^{1/2} l_0 \tag{6.8}$$

Prandtl developed a one-equation model based on Eq. (6.8) wherein a modeled transport equation for the turbulent kinetic energy is solved (Wilcox 1993). However, the one-equation models still have the same drawback as zero-equation models: they require the specification of the turbulent length scale which is virtually impossible to prescribe for complex turbulent flows.

To solve turbulent flows in complex configurations in which the turbulent length and time scale (l_0, t_0) are not universal, the two-equation models—wherein transport equations are solved for two independent quantities that are directly related to the turbulent length and time scales was proposed (Jones and Launder 1972). In the most common approach, the turbulent length and time scales are defined based on the turbulent kinetic energy K and the dissipation rate ε (i.e., $l_0 \propto K^{3/2}/\varepsilon$, $t_0 \propto K/\varepsilon$) with modeled transport equations for K and ε. The eddy viscosity is given by

$$\nu_t = C_\mu K^2/\varepsilon \tag{6.9}$$

where C_μ is a empirical model constant. The two-equation models remove many of the problems associated with specifying the length scale in the zero- and one-equation models, and have been applied to a variety of turbulent flows with various degrees of complexities. However, for some complex turbulent flows (e.g., with adverse pressure field, streamwise curvature, system rotation, etc.), the original K-ε model (Launder and Spalding 1974) cannot give satisfactory results. There are several possible factors contributing to the failures of the

K-ε model for complex turbulent flows. One of them is that coefficients are obtained based on simple flow conditions, which may not be valid for complex turbulent flows. Another weakness of the K-ε model is that it is still based on the Boussinesq's hypothesis which makes use of a scalar turbulent viscosity. The Boussinesq's hypothesis inherently assumes that turbulent viscosity is isotropic. However, turbulent viscosity, unlike molecular viscosity which is a fluid property, is a flow variable. For complex turbulent flows, eddy viscosity is, in general, an anisotropic quantity strongly affected by geometry and physical mechanisms.

To solve complex turbulent flows with anisotropic turbulent stresses, the Reynolds-stress model is explored in which each component of the Reynolds-stress tensors is solved by a partial differential equation (Launder et al. 1975). But these equations are still not closed, and a significant amount of modeling is required to treat terms involving the pressure-velocity correlation and high order moments. In reality, the success of the Reynolds-stress model is not consistent. Furthermore, compared to the eddy viscosity models, the Reynolds-stress models are more expensive to compute, because for each of the Reynolds-stress components, a partial differential equation has to be solved. This partially limits its applications in engineering flow simulations.

To reduce the expense of the Reynolds-stress models, attempts have been made to simplify the form of the Reynolds-stress transport equations. The simplification is aimed at reducing these PDEs to algebraic equations. However, the success of such models is also less than consistent. Based on the above discussion, it would seem that an improved two-equation model capable of addressing complex flow problems will be very desirable.

In the following, the Reynolds-stress transport equations and the original K-ε transport equations are firstly presented and analyzed. The implementation of the original K-ε model for two-dimensional incompressible flows in curvilinear coordinates is detailed. Then, issues associated with the non-equilibrium conditions in the K-ε turbulence model for complex flows are discussed. The interaction between different physical terms is illustrated

and analyzed. Finally, the non-equilibrium model is used to investigate two- and three-dimensional complex turbulent flow problems.

6.2 Turbulent Transport Equations

6.2.1 Reynolds-Stress Transport Equation

Let $\mathcal{N}(u_i)$ denote the Navier-Stokes operator for constant flow properties, viz.,

$$\mathcal{N}(u_i) = \varrho\frac{\partial u_i}{\partial t} + \varrho u_k\frac{\partial u_i}{\partial x_k} + \frac{\partial p}{\partial x_i} - \mu\frac{\partial^2 u_i}{\partial x_k \partial x_k} = 0 \tag{6.10}$$

In order to derive an equation for the Reynolds-stress tensor, we form the following ensemble average

$$\overline{u_i^{'}\mathcal{N}(u_j) + u_j^{'}\mathcal{N}(u_i)} \tag{6.11}$$

The full form of the Reynolds-stress equation is given as (Wilcox 1993)

$$\frac{\partial \tau_{ij}}{\partial t} + \overline{u}_k\frac{\partial \tau_{ij}}{\partial x_k} = -\tau_{ik}\frac{\partial \overline{u}_j}{\partial x_k} - \tau_{jk}\frac{\partial \overline{u}_i}{\partial x_k} + \varepsilon_{ij} - \Pi_{ij} + \frac{\partial}{\partial x_k}[\nu\frac{\partial \tau_{ij}}{\partial x_k} + C_{ijk}] \tag{6.12}$$

where

$$\Pi_{ij} = \overline{p^{'}(\frac{\partial u_i^{'}}{\partial x_j} + \frac{\partial u_j^{'}}{\partial x_i})} \tag{6.13}$$

$$\varepsilon_{i,j} = 2\mu\overline{\frac{\partial u_i^{'}}{\partial x_k}\frac{\partial u_j^{'}}{\partial x_k}} \tag{6.14}$$

$$C_{ijk} = \varrho\overline{u_i^{'}u_j^{'}u_k^{'}} + \overline{p^{'}u_i^{'}}\delta_{jk} + \overline{p^{'}u_j^{'}}\delta_{ik} \tag{6.15}$$

are, respectively, the pressure-strain correlation, the dissipation rate tensor and the turbulent diffusion correlation.

6.2.2 *K-ε* Transport Equations

The transport equation for the turbulent kinetic energy $K = -\frac{1}{2}\frac{\tau_{ii}}{\varrho}$ is obtained by contracting Eq. (6.12)

$$\varrho\frac{\partial K}{\partial t} + \varrho\overline{u}_j\frac{\partial K}{\partial x_j} = \mathcal{P} - \varrho\varepsilon + \frac{\partial}{\partial x_j}[\mu\frac{\partial K}{\partial x_j} - \frac{1}{2}\overline{\varrho u_i' u_i' u_j'} - \overline{p' u_j'}] \tag{6.16}$$

where

$$\mathcal{P} = \tau_{ij}\frac{\partial \overline{u}_i}{\partial x_j} \tag{6.17}$$

$$\varepsilon = \nu\overline{\frac{\partial u_i'}{\partial x_j}\frac{\partial u_i'}{\partial x_j}} \tag{6.18}$$

$$\frac{1}{2}\varrho\overline{u_i' u_i' u_j'}$$

$$\overline{p' u_j'}$$

are, respectively, the turbulent production, turbulent dissipation rate, turbulent diffusion and pressure diffusion terms.

A conventional approximation made to represent turbulent transport of scalar quantities is based on the notion of gradient-diffusion. In analogy to the molecular transport processes, we model $-\varrho\overline{u_j'\phi'} \sim \mu_t\partial\overline{\phi}/\partial x_j$. However, there is no justification for such a model regarding the pressure diffusion term, it is simply grouped with the turbulent transport term, and together they are also treated by the gradient-transport model

$$\frac{1}{2}\varrho\overline{u_i' u_i' u_j'} + \overline{p' u_j'} = -\frac{\mu_t}{\sigma_k}\frac{\partial K}{\partial x_j} \tag{6.19}$$

Therefore, the modeled equation for the turbulent kinetic energy becomes

$$\varrho\frac{\partial K}{\partial t} + \varrho\overline{u}_j\frac{\partial K}{\partial x_j} = \mathcal{P} - \varrho\varepsilon + \frac{\partial}{\partial x_j}[(\mu + \frac{\mu_t}{\sigma_k})\frac{\partial K}{\partial x_j}] \tag{6.20}$$

where σ_k is a closure coefficient. At this point, no approximation has entered, of course, we hope the model is realistic enough that σ_k can be chosen be constant.

The exact equation for the turbulent dissipation rate ε can be obtained by taking the following moment of the Navier-Stokes equation (Wilcox 1993)

$$2\nu\overline{\frac{\partial u_i}{\partial x_j}\frac{\partial}{\partial x_j}(\mathcal{N}(u_i))} = 0 \tag{6.21}$$

This equation takes the form

$$\varrho\frac{\partial \varepsilon}{\partial t} + \varrho\overline{u}_j\frac{\partial \varepsilon}{\partial x_j} = \mathcal{P}_\varepsilon - \Phi_\varepsilon + \mathfrak{D}_\varepsilon + \mu\nabla^2\varepsilon \tag{6.22}$$

where

$$\mathcal{P}_\varepsilon = -2\mu\overline{\frac{\partial u_k'}{\partial x_i}\frac{\partial u_k'}{\partial x_j}}\frac{\partial \overline{u}_i}{\partial x_j} - 2\mu\overline{\frac{\partial u_i'}{\partial x_k}\frac{\partial u_j'}{\partial x_k}}\frac{\partial \overline{u}_i}{\partial x_j} - 2\mu\overline{u_k'\frac{\partial u_i'}{\partial x_j}}\frac{\partial^2 \overline{u}_i}{\partial x_j x_k} \tag{6.23}$$

$$\Phi_\varepsilon = 2\mu\nu\overline{\frac{\partial^2 u_i'}{\partial x_j \partial x_k}\frac{\partial^2 u_i'}{\partial x_j \partial x_k}} + 2\mu\overline{\frac{\partial u_k'}{\partial x_i}\frac{\partial u_k'}{\partial x_j}\frac{\partial u_i'}{\partial x_j}} \tag{6.24}$$

$$\mathfrak{D}_\varepsilon = -\mu\frac{\partial}{\partial x_j}\overline{(u_j'\frac{\partial u_i'}{\partial x_k}\frac{\partial u_i'}{\partial x_k})} - 2\nu\frac{\partial}{\partial x_j}\overline{(\frac{\partial p'}{\partial x_i}\frac{\partial u_j'}{\partial x_i})} \tag{6.25}$$

are, respectively, the production, destruction and turbulent diffusion of dissipation. These three terms involve information not available from the Reynolds-stress transport equation, and need to be modeled.

By assuming that the anisotropy of dissipation tensors is proportional to the anisotropy of the Reynolds-stress tensors, due to the fact that the former follows the latter as a result of the energy cascade from large to small scales, the production of dissipation can be modeled as (Speziale 1995)

$$\mathcal{P}_\varepsilon = -C_{\varepsilon 1}\frac{\varepsilon}{K}\tau_{ij}\frac{\partial \overline{u}_i}{\partial x_j} \tag{6.26}$$

For equilibrium flows at high Reynolds numbers, the destruction of dissipation can be modeled as

$$\Phi_\varepsilon = C_{\varepsilon 2}\varrho\frac{\varepsilon^2}{K} \tag{6.27}$$

The turbulent diffusion of dissipation is usually grouped with molecular diffusion as

$$D_\varepsilon = \frac{\partial}{\partial x_j}[\frac{\mu_t}{\sigma_\varepsilon}\frac{\partial \varepsilon}{\partial x_j}] \tag{6.28}$$

Therefore, the modeled equation for the dissipation rate is

$$\varrho\frac{\partial \varepsilon}{\partial t} + \varrho\overline{u}_j\frac{\partial \varepsilon}{\partial x_j} = C_{\varepsilon 1}\frac{\varepsilon}{K}\tau_{ij}\frac{\partial \overline{u}_i}{\partial x_j} - C_{\varepsilon 2}\varrho\frac{\varepsilon^2}{K} + \frac{\partial}{\partial x_j}[(\mu + \frac{\mu_t}{\sigma_\varepsilon})\frac{\partial \varepsilon}{\partial x_j}] \tag{6.29}$$

and $C_{\varepsilon 1}$, $C_{\varepsilon 2}$ and σ_ε are constants to be determined. Typically, $C_{\varepsilon 2}$ is determined from the experiment of decaying isotropic turbulence, and $C_{\varepsilon 1}$ is determined experimentally based on the local equilibrium shear flow(Mohammadi and Pironneau 1994). Following such practice, Launder and Spalding (1974) suggested that, the various constants used in the original K-ε models assume the following values:

$$C_\mu = 0.09 \qquad C_{\varepsilon 1} = 1.44 \qquad C_{\varepsilon 2} = 1.92 \qquad \sigma_k = 1.0 \qquad \sigma_\varepsilon = 1.3 \tag{6.30}$$

6.3 Implementation of the K-ε Model for 2-D Flow

With the above development, the two-dimensional momentum equations can now be written as

$$\frac{\partial}{\partial t}(\varrho\phi) + \frac{\partial}{\partial x}(\varrho u\phi) + \frac{\partial}{\partial y}(\varrho v\phi) = \frac{\partial}{\partial x}\left(\mu_{eff}\frac{\partial \phi}{\partial x}\right) + \frac{\partial}{\partial y}\left(\mu_{eff}\frac{\partial \phi}{\partial y}\right) - \left(\frac{\partial p}{\partial x} \text{ or } \frac{\partial p}{\partial y}\right) \tag{6.31}$$

where ϕ=u *or* v, with $\mu_{eff} = \mu + \mu_t$. Here μ represents the laminar viscosity, and μ_t the turbulent viscosity.

The transport equations for K and ε, after the modelling assumptions are incorporated, can be expressed in the following form:

$$\frac{\partial}{\partial t}(\varrho\phi) + \frac{\partial}{\partial x}(\varrho u\phi) + \frac{\partial}{\partial y}(\varrho v\phi) = \frac{\partial}{\partial x}\left(\Gamma\frac{\partial \phi}{\partial x}\right) + \frac{\partial}{\partial y}\left(\Gamma\frac{\partial \phi}{\partial y}\right) + R_1 + R_2 \tag{6.32}$$

where

$$\Gamma = \begin{cases} \mu + \dfrac{\mu_t}{\sigma_k} & \text{for the } K-\text{eqn} \\ \mu + \dfrac{\mu_t}{\sigma_\varepsilon} & \text{for the } \varepsilon-\text{eqn} \end{cases} \tag{6.33}$$

$$R_1 = \begin{cases} \mu_t \, R & \text{for the } K-\text{eqn.} \\ \dfrac{C_{\varepsilon 1} \, \mu_t \, \varepsilon \, R}{K} & \text{for the } \varepsilon-\text{eqn.} \end{cases} \tag{6.34}$$

with

$$R = 2\left[\left(\frac{\partial u}{\partial x}\right)^2 + \left(\frac{\partial v}{\partial y}\right)^2\right] + \left[\frac{\partial u}{\partial y} + \frac{\partial v}{\partial x}\right]^2 \tag{6.35}$$

and

$$R_2 = \begin{cases} -\varrho \, \varepsilon \equiv -\left(\dfrac{C_\mu \, \varrho^2 \, K^*}{\mu_t}\right) K & \text{for the } K-\text{eqn.} \\ -C_{\varepsilon 2} \, \varrho \, \dfrac{\varepsilon^2}{K} \equiv -\left(C_{\varepsilon 2} \, \varrho \, \dfrac{\varepsilon^*}{K^*}\right) \varepsilon & \text{for the } \varepsilon-\text{eqn.} \end{cases} \tag{6.36}$$

The above equations are integrated over the control volume and then discretized in a manner similar to the momentum equations, described earlier. They can be transformed to body-fitted (ξ, η) coordinates, similar to the u- and v-momentum equations. The transformation is straightforward, with the final form identical to the momentum equations with the exception of R_1 and R_2 source terms, and will not be presented here.

6.3.1 Boundary Conditions and Wall Treatment

The treatment of inflow and outflow boundaries of the computational domain is done in the usual manner. All the variables at the inlet are specified or estimated. For example, if the inflow velocities are specified, K is estimated as a fraction of the square of the inlet velocity whereas ε is estimated from K and a suitable length scale representing the size of turbulent eddies (usually specified as a fraction of the inlet dimension). The variables at the outflow boundaries are estimated by a zero gradient condition which is based on the assumption that the flow is convection-dominated.

Near wall boundaries, the local Reynolds numbers are low and viscous effects are important; thus the above summarized K-ε model cannot be utilized since much of the

modeling argument is based on the high Reynolds number considerations. Moreover, steep variations in flow profiles close to the wall need a large number of grid points for proper resolution. To handle these difficulties, two approaches are commonly employed, one involving low Reynolds number versions of the K-ε model (Jones and Launder 1972, Patel et al. 1985) and the other involving the so-called wall functions (Launder and Spalding 1974). The former requires a relatively fine grid resolution in the wall region. The latter is easier to implement, but the assumption of local equilibrium between the production and dissipation of the turbulent kinetic energy is not always valid. In practice, however, the wall function approach has often produced results of accuracy comparable to the low Reynolds number approach (Viegas et al. 1985). Moreover, for complex 3-D flows, one often has very little choice but to use wall functions due to the limitation of the number of nodes that can be employed. In the present study, the wall function approach has been employed and is described next.

Close to a solid wall, a one-dimensional Couette flow analysis, parallel to the wall, is a convenient way to develop the wall function approach. Within the wall layer, the total shear stress can be considered to be a constant. The momentum equation reduces to a simple non-dimensional form given by

$$\tau = (\mu + \mu_t)\frac{\partial u^t}{\partial n} \tag{6.37}$$

where u^t is the velocity tangential to the wall (at point P, at a distance l_n normal to the wall, as shown in Fig. 6.1), and $\boldsymbol{n}$ is the direction normal to the wall. The above equation can be rewritten, using the wall shear stress and friction velocity, as

$$\frac{\tau}{\tau_w} = \left(1 + \frac{\mu_t}{\mu}\right)\frac{\partial u^+}{\partial y^+} \tag{6.38}$$

Here, τ_w is the shear stress at the wall. The local Reynolds number (or the non-dimensional normal distance of point P from the wall), y^+, is determined from

$$y^+ = \frac{\varrho\, u_\tau\, l_n}{\mu} \tag{6.39}$$

and the non-dimensional velocity u^+ is given by

$$u^+ = \frac{u^t}{u_\tau} \tag{6.40}$$

where u_τ is the friction velocity at the wall:

$$u_\tau = \sqrt{\frac{\tau_w}{\varrho}} \tag{6.41}$$

For a turbulent boundary layer over a solid flat plate, experimental evidence indicates that the wall region can be divided into two distinct zones (Hinze 1959), namely:
(a) the viscous sublayer ($0 < y^+ < 5$) which is dominated by molecular viscous effects, and
(b) the law of the wall layer ($30 < y^+ < 400$) where the shear stress is largely unchanged and is dominated by the Reynolds-stress.

A convenient engineering practice to match these two zones is to define $y^+ = 11.63$ as the point above which the flow is assumed fully turbulent and below which is dominated by viscous effects. At this location the linear velocity profile of the viscous sublayer meets the logarithmic velocity profile in the law of the wall layer.

6.3.1.1 Laminar sublayer ($y^+ < 11.63$)

In the viscous sublayer , $\mu_t/\mu \ll 1$, and the assumption $\tau = \tau_w$ leads to

$$u^+ = y^+ \quad \Rightarrow \quad \tau = \tau_w = \frac{\mu u^t{}_P}{l_n} \tag{6.42}$$

6.3.1.2 Law of the wall layer ($y^+ > 11.63$)

In the inertial sublayer , $\mu_t/\mu \gg 1$ and again the assumption $\tau = \tau_w$ along with

$$\mu_t = \varrho \varkappa y \, u_\tau \tag{6.43}$$

leads, after integrating Eq. (6.38), to

$$u^+ = \frac{1}{\varkappa} \log_e y^+ + B \equiv \frac{1}{\varkappa} \log_e (E y^+) \tag{6.44}$$

In the above, $\varkappa$ is the von Karman constant with the value 0.42. The quantity E is a function of the factors such as wall roughness, streamwise pressure gradient, etc. For a smooth impermeable wall with negligible streamwise pressure gradient, it is assigned the value

9.793. With the constant shear stress approximation in the wall layer, the transport equation for the turbulent kinetic energy (K), which is defined in Eqs. (6.32–6.36), reduces to the following:

$$-\overline{u'v'}\frac{du}{dy} = \varepsilon \tag{6.45}$$

Using the definition of Reynolds stress given by Eq. (6.5) and that of ε from Eq. (6.9), and the definition of τ from Eq. (6.37) with $\mu_t/\mu \gg 1$, we obtain the following relation:

$$\tau \equiv \tau_w = \varrho\, K\, C_\mu^{1/2} \tag{6.46}$$

Using Eq. (6.40) and Eq. (6.41), we obtain

$$u^+ \cong \frac{u^t}{\sqrt{\tau_W/\varrho}} \quad \Rightarrow \quad \tau_W = \frac{u^t}{u^+}\,\varrho\, C_\mu^{1/4}\, K^{1/2} \tag{6.47}$$

Then using the definitions (6.46) and (6.44), we finally obtain for the shear stress at the wall:

$$\tau_W = \frac{\varrho\, C_\mu^{1/4}\, K^{1/2}\, \varkappa\, u^t}{\ln(Ey^+)} \tag{6.48}$$

where y^+ is evaluated from

$$y^+ = \frac{l_n\sqrt{\tau_W/\varrho}}{\nu} \cong \frac{l_n\, \varrho\, C_\mu^{1/4}\, K^{1/2}}{\mu} \tag{6.49}$$

Also, from Eq. (6.46) and (6.43) and the definition of ε from Eq. (6.9), we obtain the following form for ε in the wall layer:

$$\varepsilon = \frac{C_\mu^{3/4}\, K^{3/2}}{\varkappa\, l_n} \tag{6.50}$$

6.3.2 Implementation of the Wall Shear Stress in Momentum Equations

To illustrate the implementation of the wall shear stress for a control volume adjacent to a wall, we refer to Fig. 6.1. If the point P is in the viscous sublayer, the net viscous terms at the south control volume face are estimated in the usual manner. If the point P is in the inertial sublayer, the shear stress (parallel to the wall) is estimated from Eq. (6.48).The case

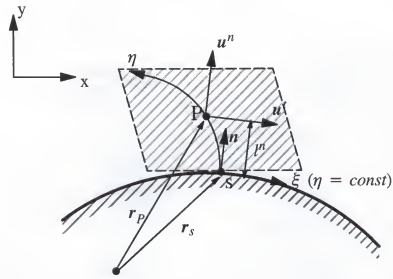

Fig. 6.1. Boundary control volume adjacent to a curved wall.

of interest is the one where the point P is in the log layer where the tangential velocity follows the log law normal to the wall. The resultant shear force at the south (bottom) face of the control volume shown in Fig. 6.1 is given by

$$F^s_{shear} = \tau_w \, A_s = \tau_s \sqrt{q_3} \tag{6.51}$$

where

$$\tau_w = \frac{\varrho_P K_P^{1/2} C_\mu^{1/4} \varkappa}{\ln E \frac{l_n K_P^{1/2}}{\nu}} \boldsymbol{u}^t \tag{6.52}$$

$$\boldsymbol{u}^t = \boldsymbol{u} - \boldsymbol{u}^n \,, \qquad l_n = \left(\boldsymbol{r}_P - \boldsymbol{r}_s\right) \cdot \boldsymbol{n} \tag{6.53}$$

In the above, l_n is the normal distance away from the wall, and $\boldsymbol{u}^n$ and $\boldsymbol{u}^t$ are the normal and tangential velocity components, respectively. The unit normal at the point s in Fig. 6.1 is $\boldsymbol{n} = \nabla\eta/|\nabla\eta|$, which can be expressed as

$$(n_x,\ n_y) = \frac{(\eta_x,\ \eta_y)}{\sqrt{\eta_x^2 + \eta_y^2}} \tag{6.54}$$

Thus, the x- and y-components of the velocity normal to the wall, $\boldsymbol{u}^n$, are given by

$$\boldsymbol{u}^n = (un_x + vn_y)\boldsymbol{n}$$

$$= \left(uy_\xi - vx_\xi\right)\frac{y_\xi}{q_3}\,\boldsymbol{i} + \left(-uy_\xi + vx_\xi\right)\frac{x_\xi}{q_3}\,\boldsymbol{j}$$

$$u_x^n = -V\frac{y_\xi}{q_3} \qquad\qquad u_y^n = V\frac{x_\xi}{q_3} \tag{6.55}$$

and the x- and y-components of the velocity tangential to the wall, $\boldsymbol{u}^t$, can be written as

$$u_x^t = \left(1 - n_x^2\right)u + n_x n_y\, v = u + V\frac{y_\xi}{q_3} \tag{6.56}$$

$$u_y^t = \left(1 - n_y^2\right)v + n_x n_y\, u = v - V\frac{x_\xi}{q_3} \tag{6.57}$$

Thus, the components of wall shear stress along x- and y-directions are given by

$$(\tau_w)_x = \frac{\varrho_P K_P^{1/2} C_\mu^{1/4} \varkappa}{\ln Ey^+}\, u_x^t \qquad\qquad (\tau_w)_y = \frac{\varrho_P K_P^{1/2} C_\mu^{1/4} \varkappa}{\ln Ey^+}\, u_y^t \tag{6.58}$$

The wall shear stress given by Eq. (6.52) is related to the tangential velocity as

$$\tau_w = \mu_{eff}\frac{\partial \boldsymbol{u}^t}{\partial \boldsymbol{n}} \tag{6.59}$$

Since the viscous terms in the momentum equations, are expressed in terms of $\partial\phi/\partial\xi$ and $\partial\phi/\partial\eta$ (where $\phi \equiv u$ *or* v), we need to establish a relation between the normal derivative of the tangential velocity and $\partial\phi/\partial\xi$ and $\partial\phi/\partial\eta$. Towards this end, we utilize the derivative, of a quantity f, normal to a ξ (*i.e.*, $\eta = const$) line:

$$\frac{\partial f}{\partial n}(\eta) = \frac{1}{J\sqrt{q_3}}\left[-q_2\frac{\partial f}{\partial \xi} + q_3\frac{\partial f}{\partial \eta}\right] \tag{6.60}$$

Now, taking the normal derivatives of u_x^t:

$$\frac{\partial u_x^t}{\partial n} = \frac{\partial u}{\partial n} - \frac{\partial u_x^n}{\partial n}$$

$$= \frac{1}{J\sqrt{q_3}}\left[- q_2\frac{\partial u}{\partial \xi} + q_3\frac{\partial u}{\partial \eta}\right] - \frac{1}{J\sqrt{q_3}}\left[- q_2\frac{\partial}{\partial \xi}\left(- V\frac{y_\xi}{q_3}\right) + q_3\frac{\partial}{\partial \eta}\left(- V\frac{y_\xi}{q_3}\right)\right] \tag{6.61}$$

Thus,

$$- q_2\frac{\partial u}{\partial \xi} + q_3\frac{\partial u}{\partial \eta} = J\sqrt{q_3}\frac{\partial u_x^t}{\partial n} + \left[q_2\frac{\partial}{\partial \xi}\left(V\frac{y_\xi}{q_3}\right) - q_3\frac{\partial}{\partial \eta}\left(V\frac{y_\xi}{q_3}\right)\right] \tag{6.62}$$

The LHS of Eq. (6.62) is the net viscous term in the u-momentum equation expressed in (ξ, η) coordinates. The RHS is merely a rearrangement of the net viscous stress – the first term can be interpreted as the x-component of the shear stress (parallel to the wall) and the second term as the x-component of stress normal to the wall.

Finally, the viscous terms at the south face in the u-momentum equation, are computed as follows:

$$\left[\frac{\mu_{eff}}{J}\left(- q_2\frac{\partial u}{\partial \xi} + q_3\frac{\partial u}{\partial \eta}\right)\right]_s = \left[\mu_{eff}\frac{\partial u_x^t}{\partial n}\sqrt{q_3}\right]_s + \left[\frac{\mu_{eff}}{J}\left\{ q_2\frac{\partial}{\partial \xi}\left(V\frac{y_\xi}{q_3}\right) - q_3\frac{\partial}{\partial \eta}\left(V\frac{y_\xi}{q_3}\right)\right\}\right]_s$$

$$= \left[(\tau_w)_x\sqrt{q_3}\right]_s + \left[\frac{\mu_{eff}}{J}\left\{ q_2\frac{\partial}{\partial \xi}\left(V\frac{y_\xi}{q_3}\right) - q_3\frac{\partial}{\partial \eta}\left(V\frac{y_\xi}{q_3}\right)\right\}\right]_s \tag{6.63}$$

where $(\tau_w)_x$ is given by Eq. (6.58). Similarly, for the v-momentum equation:

$$\left[\frac{\mu_{eff}}{J}\left(- q_2\frac{\partial v}{\partial \xi} + q_3\frac{\partial v}{\partial \eta}\right)\right]_s = \left[(\tau_w)_y\sqrt{q_3}\right]_s + \left[\frac{\mu_{eff}}{J}\left\{ - q_2\frac{\partial}{\partial \xi}\left(V\frac{x_\xi}{q_3}\right) + q_3\frac{\partial}{\partial \eta}\left(V\frac{x_\xi}{q_3}\right)\right\}\right]_s \tag{6.64}$$

6.3.3 Implementation of the *K-ε* Equations near Wall Boundaries

The turbulent kinetic energy at the point *P* near a wall, K_P, is obtained from the usual *K*-balance, but the flux expression at the wall boundary is suppressed by setting $A_S=0$ (for

the bottom boundary shown in Fig. 6.2). The evaluation of the source term for the K-equation is modified by noting that the second term in R given by Eq. (6.35) can be simplified near the wall as

$$\mu_t \left(\frac{\partial u}{\partial y} + \frac{\partial v}{\partial x} \right)^2 \cong \tau_S \left(\frac{u_P - u_S}{l_n} \right) \tag{6.65}$$

where $u_S = 0$ at the wall boundary, τ_S is the average of neighboring values of τ_W, and u_P is the average of the neighboring values of u. Moreover, the dissipation term in the K-equation near the wall is extended to the laminar sublayer by modifying it as

$$\varepsilon \cong \frac{c_\mu^{3/4} K^{3/2} u^+}{l_n} \tag{6.66}$$

where u^+ is defined by either Eq. (6.42) for the viscous sublayer or Eq. (6.44) for the inertial sublayer. Also, for lack of better knowledge, the diffusion of K to the wall is set to zero.

The value of ε reaches a finite value at the walls which is generally an unknown, unlike the value of K which falls to zero at the wall. The ε-equation itself reduces to a simple form but in the computation, the value of ε near the wall boundaries is estimated from the

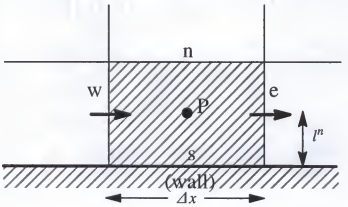

Fig. 6.2. Wall treatment for K and e.

equilibrium expression given by Eq. (6.50), and not from the usual ε-balance since we have insufficient knowledge to define the coefficient A_S.

6.4 Turbulence Modeling for Non-Equilibrium Flows

The original K-ε model detailed above is commonly employed for many different types of engineering applications. For many applications, this model yields at least competitive results with respect to other models, including both algebraic models and Reynolds-stress models. Despite this fact, the standard K-ε model has known deficiencies for certain types of flows. One notable case is for flows without equilibrium between the production and dissipation of the turbulent kinetic energy, as expressed by Eq. (6.45). In the following, we examine the performance of the standard K-ε two-equation turbulence model for certain non-equilibrium flows and assess the potential benefits of modifying the model proposed by Launder and Spalding (1974).

There are five parameters which need to be determined in the original K-ε two-equation model, namely, the turbulent Prandtl numbers for K and ε, the two coefficients regulating the magnitude of the production and dissipation in the ε equation ($C_{\varepsilon 1}$ and $C_{\varepsilon 2}$), and the coefficient regulating the magnitude of the eddy viscosity (C_μ). The coefficients $C_{\varepsilon 1}$, $C_{\varepsilon 2}$, and C_μ are determined largely based on the equilibrium condition, in which case the production and dissipation of K balance each other and convective/diffusive effects are negligible. However, for certain fluid flows, such as flows with rotation, adverse pressure gradient, recirculation, and large streamline curvature, flow equilibrium does not exist. When a turbulent flow is not in equilibrium, besides the length and time scales dictated by the flow configuration, dynamic characteristics create extra length and time scales according to the local flow structure. In the original model, the modeling coefficients do not respond to such structural changes because their values are fixed; variations in values of these coefficients will have to be considered when the global and local length and time scales are

not comparable. An attractive approach is to extend the applicability of the original model K-ε by accounting for non-equilibrium conditions, but to make the modified model reduce back to the original model when the equilibrium condition is met.

Modifications have been proposed to the original K-ε two-equation model to account for the effect of recirculation and large mean strain rate (Lien and Leschziner 1994, Shih et al. 1995, Speziale 1995). An entirely distinct approach to modelling turbulence has been taken by Yakhot and Orszag (1986) in the context of K-ε model, who, using Renormalization Group Theory (RNG) theory, have been able to derive the K-ε model with much rigor. The RNG-based K-ε model is of the same form as the original K-ε model, but assumed different model coefficients which are evaluated by the theory. Two of the coefficients have been modified with the corrections of Yakhot and Smith (1992). In the modified version of the RNG-based K-ε model, all the coefficients still have constant values which have been shown to be inappropriate for flows with high strain rate. A correction has been made to the ε-equation (Yakhot et al. 1992). That correction, not strictly arising from RNG consideration, is designed to sensitize the ε-equation to high mean strain rate so as to increase the rate of dissipation, which, in turn, can lower the level of turbulence viscosity. This correction has been found to yield improved solution in some cases such as the backward facing step flow and flow in a turnaround duct (Orszag et al. 1993).

In the present study, several alternatives are investigated :

(i) Adding a time scale in the ε-equation by introducing of a functional form for $C_{\varepsilon 1}$, to account for non-equilibrium between production and dissipation. This modification results in what is hereafter called the non-equilibrium model. This model has been tested in a compressible recirculating flow with improved performance over the standard model (Chen and Kim, 1987, Tucker and Shyy, 1993). A further modification can be made by allowing a similar variation for the coefficient $C_{\varepsilon 2}$, as will be discussed later.

(ii) The renormalization group (RNG) model, which can serve as a comparison to the non-equilibrium model (Orszag et al. 1993).

(iii) A low Reynolds number formulation with a modified functional form for C_μ. In the present form, a popular expression has been chosen (Launder and Sharma 1974), as shown in the equations to follow. In this modification, the key parameter is the turbulent Reynolds number, R_t, defining the characteristics of the turbulent versus laminar viscosities. It has been most frequently applied to the near wall condition; however, this modeling concept can also be extended to the non-equilibrium flow condition. This model has also been adopted and extended in turbulent flows involving phase change with substantial improvement reported in Shyy et al. (1992). While other models can also be formulated in which C_μ is defined as a function of the strain rate and the streamline curvature. They are not considered in this investigation in order to maintain a reasonable scope.

The governing equations for the various K-ε models can be unified in the form shown below in Eqs. (6.67)–(6.74), with the constants summarized in Table 6.1.

$$\frac{\partial K}{\partial t} + \overline{u}_i \frac{\partial K}{\partial x_i} = P - \varepsilon + \frac{\partial}{\partial x_i}\left(\frac{\nu_T}{\sigma_k}\frac{\partial K}{\partial x_i}\right) \tag{6.67}$$

$$\frac{\partial \varepsilon}{\partial t} + \overline{u}_i \frac{\partial \varepsilon}{\partial x_i} = C_{\varepsilon 1}\frac{\varepsilon}{k}P - C_{\varepsilon 2}\frac{\varepsilon^2}{k} + \frac{\partial}{\partial x_i}\left(\frac{\nu_T}{\sigma_\varepsilon}\frac{\partial \varepsilon}{\partial x_i}\right) \tag{6.68}$$

$$P = 2\nu_T \overline{S}_{ij}\overline{S}_{ij} \tag{6.69}$$

$$\overline{S}_{ij} = \frac{1}{2}\left(\frac{\partial \overline{u}_i}{\partial x_j} + \frac{\partial \overline{u}_i}{\partial x_j}\right) \tag{6.70}$$

$$\nu_t = C_\mu \frac{K^2}{\varepsilon} \tag{6.71}$$

For the low Reynolds number model, C_μ is no longer a constant, but instead takes the following functional form:

$$C_\mu = 0.09f \tag{6.72}$$

where

$$f = \exp\left[\frac{-3.4}{(1 + R_t/50)^2}\right] \tag{6.73}$$

$$R_t = \frac{K^2}{\varepsilon \nu_l} \tag{6.74}$$

In the following, we present a number of test cases to compare the relative performances of the various models described above for non-equilibrium flows.

6.5 Case Studies

6.5.1 Backward Facing Step Flow

The most frequently compared parameter in this flow problem is the length of the recirculation zone, which is around 6.5 to 7.5 times the step height for flow over a step with a height equal to one-third of the overall channel height. Detailed experimental information can be found in Kim et al. (1978). A recent work on large eddy simulation has been reported by Akselvoll and Moin (1995).

Table 6.1. Comparison of coefficients adopted by different models

Model	C_μ	$C_{\varepsilon 1}$	$C_{\varepsilon 2}^*$	σ_k	σ_ε
Standard	0.09	1.44	1.92	1.0	1.3
RNG	0.085	$1.42 - \frac{\eta(1 - \eta/\eta_0)}{1 + \beta\eta^3}$	1.68	0.7179	0.7179
Non Equilibrium	0.09	$1.15 + 0.25\frac{P}{\varepsilon}$	1.90	0.8927	1.15

$\eta = S\frac{K}{\varepsilon}$ $\quad S = (2\overline{S}_{ij}\overline{S}_{ij})^{\frac{1}{2}}$ $\quad \eta_0 = 4.38$ $\quad \beta = 0.015$

* Variation in $C_{\varepsilon 2}$ will be discussed later.

Calculations have been performed for a flow at Re=10^6 with a grid consisting of 121x91 nodes. For the computations presented, a second-order upwind scheme is used for the convection terms. Using Figs. 6.3–6.7 for reference, the following points are noted:

(i) Figure 6.3 shows the streamfunction, u- and v-velocity component and pressure contours obtained with the standard model. A summary of the re-attachment lengths predicted by the various models is given in Table . Both the RNG and non-equilibrium models improve the prediction of the reattachment point substantially; however, relatively modest differences exist between them. On the other hand, the overall flow characteristics such as the pressure distributions predicted by all three turbulence models are quite similar, indicating that this flow is pressure-convection dominated.

(ii) As evidenced by Fig. 6.4, substantial differences in the distribution of $C_{\varepsilon 1}$ have been predicted by the two modified models. This aspect is also clearly presented in the profile plots shown at x_r/H=3.0 (Fig. 6.5) and x_r/H=9.0 (Fig. 6.6). Hence, it is interesting to observe that the predicted recirculation region lengths are very close for the two models.

(iii) Figures 6.5 and 6.6 show that the production term and dissipation term in the K equation are not equal, especially in the recirculation zone, demonstrating that the flowfield is not in equilibrium; hence, it justifies the use of modified expressions embodied in the non-equilibrium and RNG models. It is also interesting to observe that with the

Table 6.2. Re–attachment lengths for backward–facing step flow

Model	Re–attachment length
Standad $K-\varepsilon$	5.74
RNG $K-\varepsilon$	6.78
Non–equilibrium $K-\varepsilon$	7.19
Low–Re non–equilibrium $K-\varepsilon$	7.19

Streamfunction Smax=2.00 Smin=-8.49×10^{-2}
Reattachment point $x_r/H = 5.74$

u–velocity umax=1.01 umin=–0.26

v–velocity vmax=8.12×10^{-2} vmin=-8.42×10^{-2}

Pressure Pmax=4.98×10^{-2} Pmin=–0.17

Fig. 6.3. Solution characteristics of standard K-ε model: Re=1.0×10^6, Grid size=121x91, second-order upwind scheme.

Viscosity $(\nu_T)max/\nu=9.10x10^3$ $(\nu_T)min/\nu=3.74$

(i) Standard K-ε model

Coefficient $(C_{\varepsilon 1})max/1.44=1.26$ $(C_{\varepsilon 1})min/1.44=0.16$

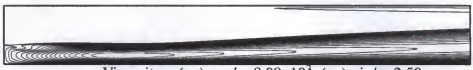

Viscosity $(n_T)max/n=8.09x10^3$ $(n_T)min/n=2.50$

(ii) RNG K-ε model

Coefficient $(C_{\varepsilon 1})max/1.44=2.14$ $(C_{\varepsilon 1})min/1.44=0.32$

Viscosity $(\nu_T)max/\nu=7.27x10^3$ $(\nu_T)min/\nu=3.72$

(iii) Non-equilibrium K-ε model

Fig. 6.4. Eddy viscosity and $C_{\varepsilon 1}$ contours for the three K-ε models: $Re=1.0x10^6$, Grid size=121x91, second-order upwind scheme.

non-equilibrium model, and to a less extent with the RNG model, the source terms in both the K and ε equations exhibit sharper profiles, which means that the distribution of eddy viscosity is more responsive to the change in the flow structure.

(iv) Figure 6.4 shows that the standard model yields the highest eddy viscosity, while the non-equilibrium model yields the lowest. In a more detailed manner, as shown in Fig. 6.6, one observes that the RNG model does not always yield smaller eddy viscosity compared to the standard model. However, the region where both the standard and RNG models predict comparable eddy viscosities is outside the recirculation zone, making this aspect less significant. Overall, the non-equilibrium model seems to yield consistently lower values of eddy viscosity in the whole domain.

(v) Figures 6.4–6.6 also reveal that the locations of maximum eddy viscosity show only a modest variation with respect to the x-coordinate; furthermore, they are not the same as those of K, ε, or the source/sink terms in the K-ε equations. Since μ_t is related to K^2/ε, this observation is not surprising.

(vi) Finally, the K profiles at two locations are plotted in Fig. 6.7. Combined with the ε profiles shown in Figs. 6.5 and 6.6, there is no clear trend regarding the primary quantities of the K-ε equations. The eddy viscosity trend, however, is more discernible, especially between the original and non-equilibrium models.

6.5.2 Hill Flow Inside a Channel

This case, as schematically shown in Fig. 6.8, is designed to investigate the characteristics of the flow over a polynomial-shaped obstacle mounted on a flat channel. Similar to the backward facing step, a recirculating region forms on the leeward side of the hill. The characteristics of this flow are well documented and the problem was used as one of the benchmark cases for the 4th ERCOFTAC/IAHR Workshop on Refined Flow Modeling (April 3–7, 1995, Karlsruhe, Germany. The database address is: http://fluindigo.mech.surrey.ac.uk). The inlet flow condition as well as flow profiles of

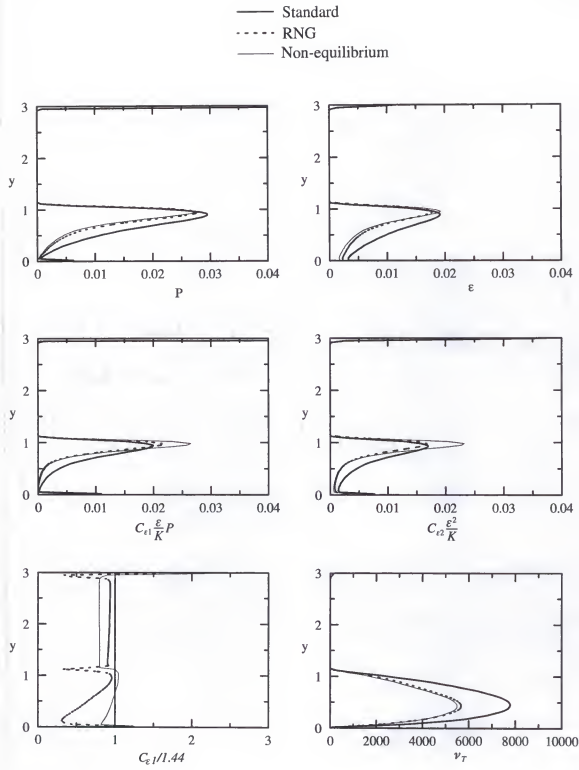

Fig. 6.5. Profile comparisons of the modelling terms resulting from the different K-ε models x/H=3.0.

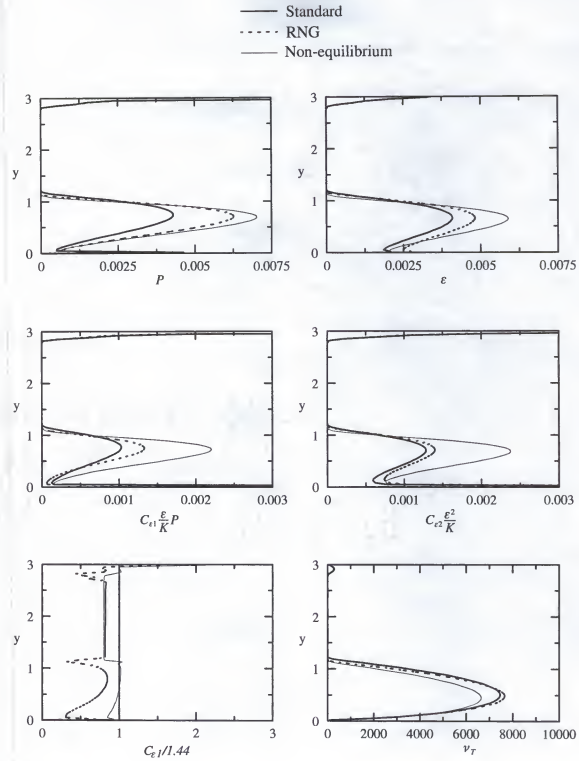

Fig. 6.6. Profile comparisons of the modelling terms resulting from the different K-ε models at x/H = 9.0.

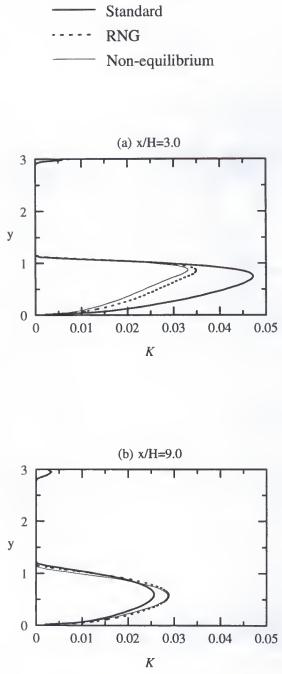

Fig. 6.7. Profile comparisons of turbulent kinetic energy resulting from the different K-ε models at (a) x/H = 3.0 and (b) x/H = 9.0.

mean and turbulent quantities at various locations are available in a computer data bank administered by ERCOFTAC. Detailed experimental information can be found in Almeida et al. (1993).

This flow exhibits substantial variation in the streamline curvature from both the hill and the recirculation zone behind the hill, which poses a stringent test for turbulence models. The present computations have been conducted with 151x121 grid points along the streamwise and transverse directions, respectively. The convection scheme used is based on second-order upwind differencing (Shyy et al. 1992).

(i) Figure 6.9 compares the standard and non-equilibrium models with the experimental data for the u-velocity profiles at six locations along the hill. Substantial changes have been recorded along the streamwise location; the two models have produced very comparable agreements to measurements.

(ii) Figure 6.10 shows the v-velocity profiles at the corresponding locations. Because the v-velocity component has a smaller magnitude, the differences between the two models are more discernible. Neither model is superior in all aspects; however, the non-equilibrium model exhibits increasing maximum v-velocity magnitudes from x/hmax=1 to the reattachment point, located at x/hmax=4.79; this trend is consistent with the experimental information.

(iii) Figure 6.11 shows the eddy viscosity profiles and the $C_{\varepsilon 1}$ profiles at selected locations. Consistent with the previous case, the non-equilibrium model generally shows smaller maximum eddy viscosity, and hence reduced turbulent transport. This characteristic is clearly observable in the recirculation region. Outside the recirculation region, however, the eddy viscosities predicted by the two models are in very close agreement.

(iv) Table 6.3 shows the re-attachment lengths for the non-equilibrium model with the modification to $C_{\varepsilon 2}$ based on the ratio P/ε. The motivation for allowing $C_{\varepsilon 2}$ to vary according to the flow structure is provided by the observation that the non-equilibrium model substantially over-predicts the re-attachment length for this flow. This indicates that

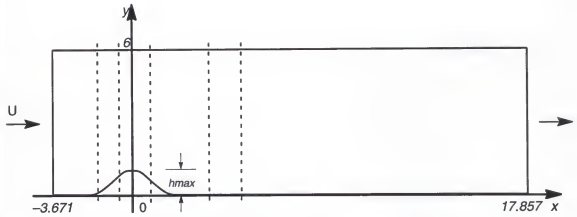

(a) Schematic of the geometry

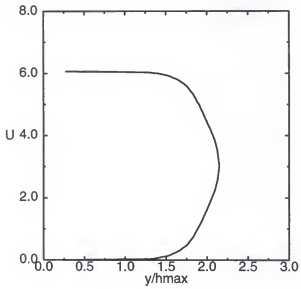

(b) Inlet condition

Fig. 6.8. Schematic of the geometry with inlet condition for single hill flow. The dashed lines indicate where comparisons are made.

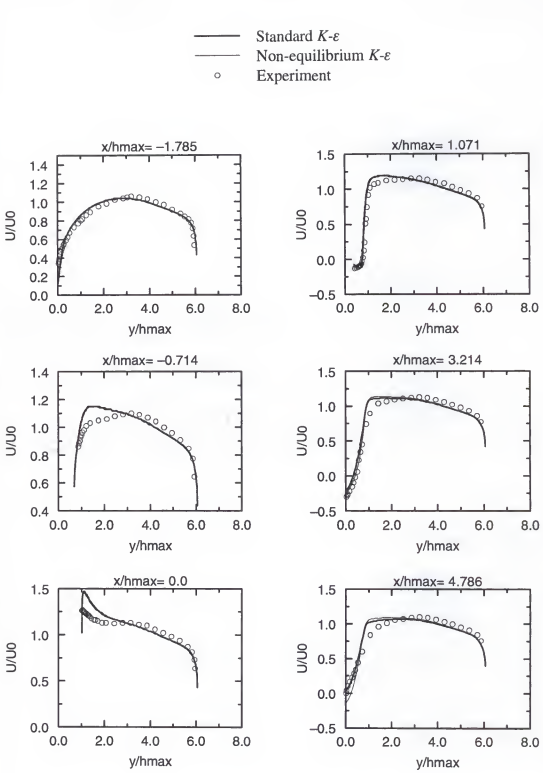

Fig. 6.9. Comparisons of u-velocity among experimental, the standard K-ε model and the non-equilibrium model results at different locations for a single hill flow; Re=6x10^4.

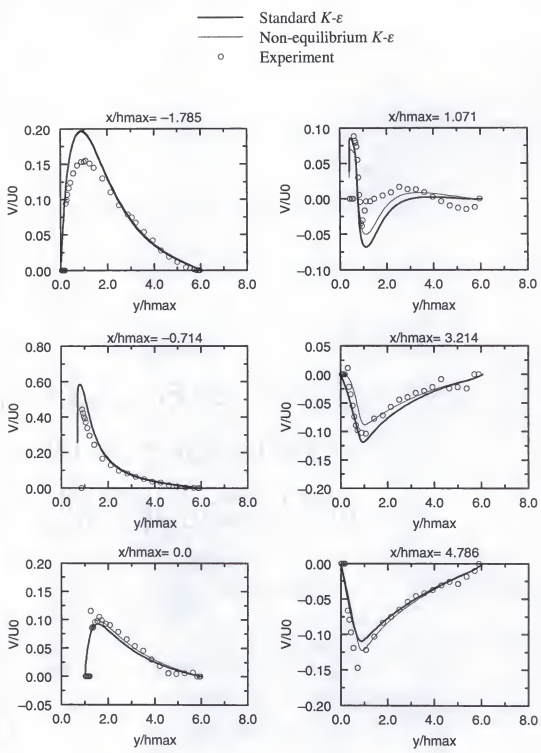

Fig. 6.10. Comparisons of v-velocity among experimental, the standard K-ε model and the non-equilibrium model results at different locations for a single hill flow; Re=6×10^4.

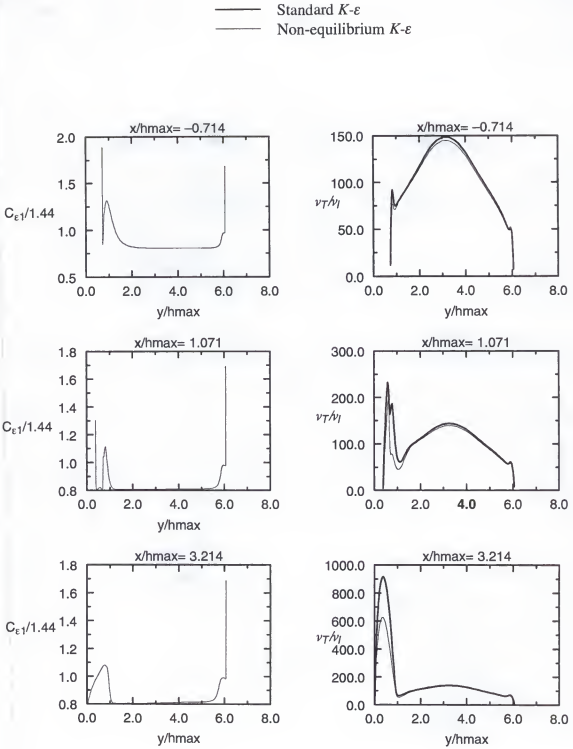

Fig. 6.11. Comparisons of $C_{\varepsilon 1}$ and eddy viscosity between the standard and the non-equilibrium K-ε model results at different locations for a single hill flow; Re=$6x10^4$.

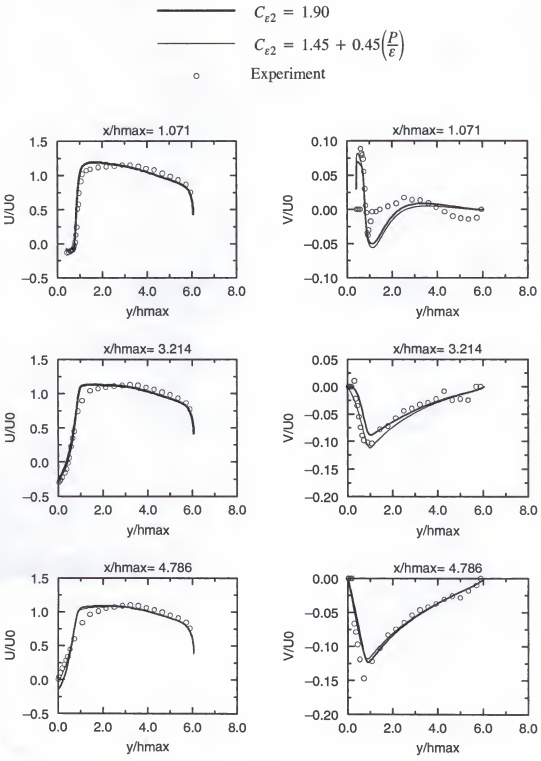

Fig. 6.12. Comparisons of *u*- and *v*- velocity among experiment and non-equilibrium model with different $C_{\varepsilon 1}$ values for a single hill flow; Re=6x10^4.

there is too much production of ε, resulting in a prohibitively low value of ν_t. Accordingly, we have devised a modification to allow $C_{\varepsilon 2}$ to respond to the ratio P/ε in a way similar to $C_{\varepsilon 1}$. Figure 6.12 shows the u- and v-velocity profiles at three locations with two different $C_{\varepsilon 2}$. The non-equilibrium effect with these two values of $C_{\varepsilon 2}$ on the velocity profiles can be clearly observed. This exercise demonstrates that further improvement of the non-equilibrium model can be made. It appears that $C_{\varepsilon 2} = 1.45 + 0.45(\frac{P}{\varepsilon})$ is a good choice.

6.5.3 3-D Diffuser Flow

This problem consists of a channel of 90-degree turn, with the cross-section changing from circular at the inlet to rectangular at the outlet, and with an outlet-to-inlet area ratio of 5. The inlet flow is swirling, which causes the main flow to be prone to form recirculation regions in the core. After making the 90-degree turn, the flow may separate in the upper wall region due to the large streamline curvature associated with the turning. More details about this complicated flow problem can be found in Vu and Shyy (1990).

In the present case, we study the relative performance between the standard and the non-equilibrium models for such a diffuser, where two "piers" are placed in the middle of the channel along the streamwise direction. Figure 6.13 shows the geometry and a side-view plot of the grid system which has been used. A second-order upwind convection scheme with two grid sizes, one with about 80,000 nodes and the other with about 250,000 nodes has been used. The following points are noted about the flow solutions.

Table 6.3. Effect of modification of $C_{\varepsilon 2}$ in non − equilibrium model on re − attachment length for the hill flow

$C_{\varepsilon 2}$	$1.35 + 0.55\left(\frac{P}{\varepsilon}\right)$	$1.45 + 0.45\left(\frac{P}{\varepsilon}\right)$	$1.55 + 0.35\left(\frac{P}{\varepsilon}\right)$	$1.65 + 0.25\left(\frac{P}{\varepsilon}\right)$	1.9	Exper.
$\frac{x_r}{h_{max}}$	4.678	4.892	5.179	5.357	5.714	4.786

(i) Figure 6.14 compares the distribution of the eddy viscosity in the middle side-view plane. Although both predictions seem qualitatively similar, clearly, the non-equilibrium model predicts a more compact distribution than the standard model. This aspect is consistent with our observation in the previous cases. Because the non-equilibrium model is more sensitive to changes in the flow structure, it maintains lower values of the eddy viscosity in the outer region. In comparison, the standard model tends to be more diffusive, in that the eddy viscosity is generally higher in much of the flow domain.

(ii) The differences in the eddy viscosity distribution make a visible impact on the velocity field. Figure 6.15 shows that with the non-equilibrium model, convection is weaker in the central region just downstream of the inlet, which forms a blockage there and causes the flow to be stronger in the upper wall region of the elbow. The standard model, in comparison, is more uniform before the turn of the diffuser. In addition, the velocity field is less uniform in the elbow domain because it is less restricted by the core flow during the turn.

(iii) Finally, the two turbulence models are compared using the three-dimensional streaklines plots shown in Fig. 6.16 and Fig. 6.17. As evidenced by these plots, the predicted swirling structures in the throat domain are different with the two models because the non-equilibrium model yields smaller eddy viscosity values. Consequently, the flow rate distribution in the downstream passages is also different.

6.6 Concluding Remarks

In this chapter, the modeling issues of K-ε turbulence model are discussed and analyzed. Specifically, the comparison study of original, RNG and non-equilibrium K-ε models are conducted with three recirculating flow cases: (a) the backward facing step flow (where separating point is fixed). (b) the hill flow (where separation point is not fixed). (c) the 3-D diffuser flow (3-D flow with streamline curvature). It has been observed that the

equilibrium condition—which is the basis of the original K-ε model, is not satisfied for some flow conditions, especially, separating flows. The non-equilibrium K-ε model, where the ε-equation is modified according to the imbalance between the production term and dissipation term of the turbulent kinetic energy, produces encouraging results for certain complex flow computations. As evidenced by the test problems, the non-equilibrium model appears to be more responsive to the change in flow structure, often resulting in lower maximum eddy viscosity and reduced turbulent transport. It may, however, have too strong a sensitivity in the region not far from non-equilibrium. Further optimization of $C_{\varepsilon 1}$, $C_{\varepsilon 2}$, and C_{μ} is desirable.

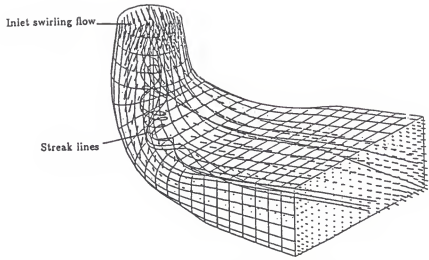

(a) a 3D view of the flow configuration

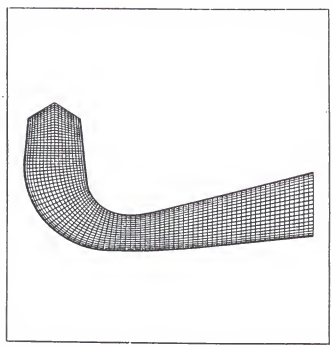

(b) Grid distribution on side–view plane

Fig. 6.13. Schematic of configuration and grid layout of a draft tube.

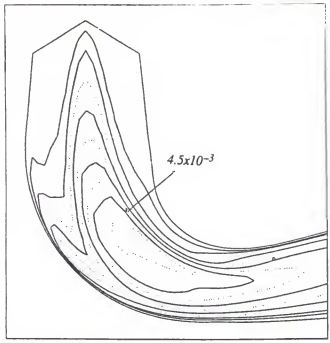

(a) Standard model

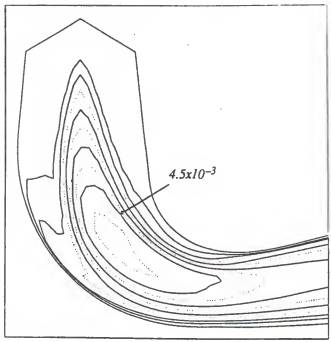

(b) Non–equilibrium model

Fig. 6.14. Comparison of eddy viscosity with the standard and the non-equilibrium models.

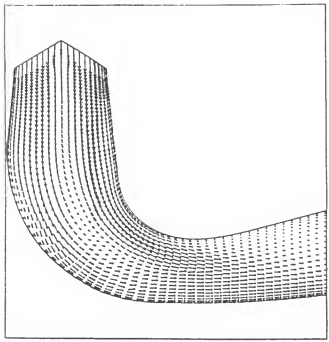

(a) Standard model

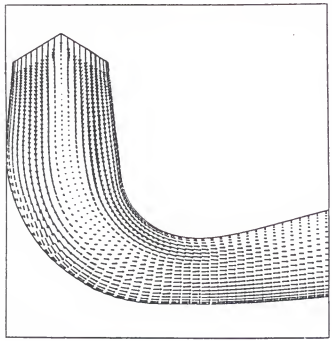

(b) Non–equilibrium model

Fig. 6.15. Comparison of velocity field with the standard and the non-equilibrium models.

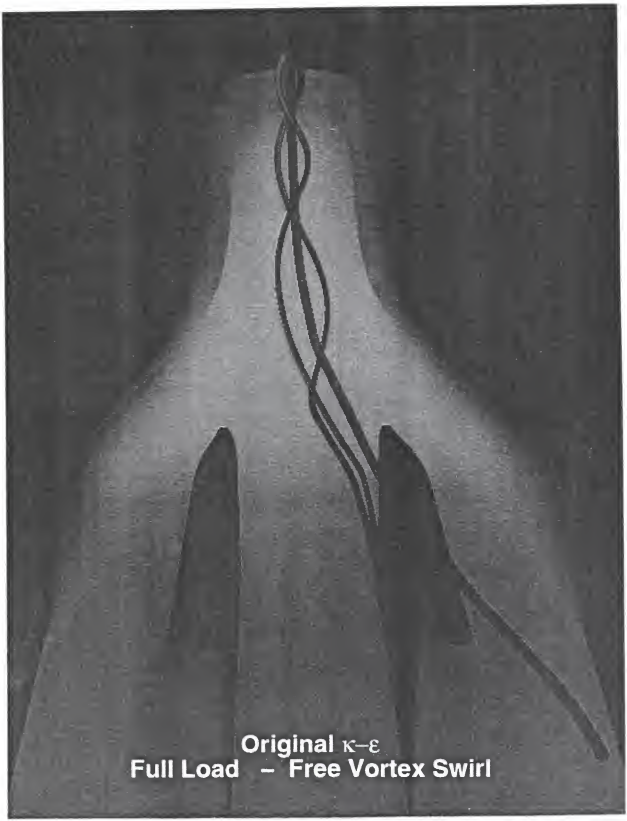

Fig. 6.16. Streakline plot for 3-D diffuser with internal piers. Standard K-ε model.

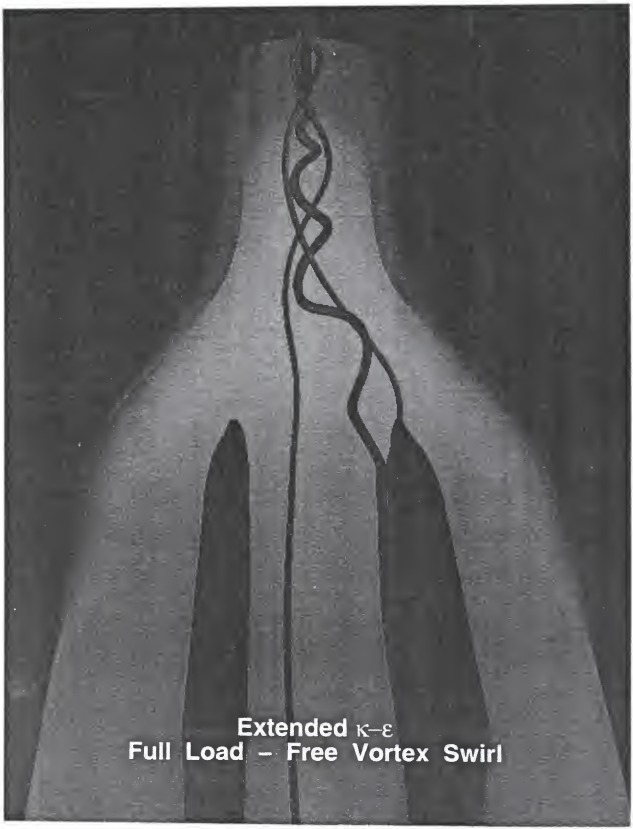

Fig. 6.17. Streakline plot for 3-D diffuser with internal piers. Non-equilibrium K-ε model.

CHAPTER 7
TWO-EQUATION TURBULENCE MODELING WITH ROTATIONAL EFFECT

7.1 Background

It is known from both experiment and direct numerical simulation data that for homogeneous flow, the system rotation can change the turbulence dissipation rate(Bardina et al. 1985, Shimemura 1993). It is also well known that when the axis of rotation is perpendicular to the plane of mean shear, rotation induces Coriolis force which can have a considerable effect on the mean flow pattern as well as the turbulence structure. It was pointed out by Johnston et al. (1972) that there are two basic effects associated with boundary layers on rotating surfaces: (i) if components of the Coriolis acceleration exist parallel to the solid surface on which the layers are growing, three-dimensionality, i.e., secondary flows will tend to develop in the mean flow field of the layers; (ii) if a component of the Coriolis acceleration is perpendicular to a solid surface, stabilizing effects are observed in the turbulence structure. Both effects are important in the flow fields of centrifugal impellers.

Three different stability-related phenomena in bound rotating shear flows have been observed by Johnston et al. (1972): (i) rotation can, by a change in the wall-layer streak burst rate, modifying the rate of turbulence production relative to dissipation and thereby modifying the profiles of turbulence energy, stress and mean velocity across the layer; (ii) rotation can increase or decrease the tendency of a hydrodynamically unstable laminar layer to undergo transition to a turbulent state, i.e., rotation can promote or suppress turbulent transition; (iii) finally, for laminar boundary layers and laminar channel flows, rotation may induce instability of the flow to large-scale disturbances, for example, the development of large cellular vortical models of the Taylor-Gortler type. The effect of the Coriolis force on turbulence structure of shear flows has been analyzed by Johnston et al. (1972), and the role

of the gradient Richardson number has been identified. The stability-related phenomena of rotating flows have also been analyzed by Bradshaw (1969) with the examination of other turbulent shear flows with analogous non-conservative body forces: curved-streamline flows with centrifugal forces and density stratified flows with buoyant forces normal to the plane of flow, and by Tritton (1992) with the 'displaced particle analysis'.

Direct and large-eddy simulations of turbulence, which require the solution of the three-dimensional time-dependent Navier-Stokes equations, may complement experimental investigation of rotating shear flows in a fruitful way, and thereby promote our understanding of the influences of rotation on the turbulence structure. The direct and large-eddy simulation of flow in a rotating channel (Kim 1983, Kristoffersen and Andersson 1993) reproduced many of the experimentally observed effects of the Coriolis forces on the mean flow and its turbulence structure. However, these flow simulations are only obtained at relatively low Reynolds number. For simulating high Reynolds number rotating turbulence flows, turbulent models with rotating effect are needed.

A number of computational studies using the Reynolds-averaged approach have been done to predict the effect of rotation on turbulence as well as mean flow quantities. The simplest turbulence model is based on the mixing length formula (Bradshaw 1969):

$$l/l_0 = 1/(1 + \beta\ R_i) \tag{7.1}$$

where β is a constant determined from experiments, l_0 is the mixing length at zero rotation, and R_i is the Richardson number, which is the local stability parameter and a negative value of R_i denotes an unstable region while a positive value denotes a stable region. Howard et al. (1980) and Younis (1993) used a two-equation K-ε model with modifications based on the value of the turbulent Richardson number to incorporate the effect of rotation on turbulence structure and on the mean flow. Galmes and Lakshminarayana (1984) and Warfield and Lakshminarayana (1987) used algebraic Reynolds-stress models to account for the rotational effect and the anisotropy of the turbulence. Launder et al. (1987) used a full

second moment closure to calculate fully developed rotating channel flow. In general, these methods have been successful in capturing the mean characteristics of the flow and in some cases also the turbulent quantities. However, the computational expense depends on the extent of the complexity of the turbulence models.

In the following, the rotational effect on turbulence modeling within the context of the K-ε model is investigated. Firstly, the turbulent transport equation for Reynolds-stress in the rotational frame is presented. The rotational effect analysis with the K-ε model is detailed. Secondly, a physical analysis of effect of rotation on turbulence structure is conducted. Based on the these analyses, a K-ε model with rotational effect in general three-dimensional coordinate is proposed. The proposed model is tested with two flow cases: two-dimensional channel flow and backward facing step flow. Finally, simulation of a torque converter flow will be presented.

7.2 The Momentum and Turbulent Transport Equations

If the coordinate system is attached with the rotational system, then the momentum equation is expressed as below

$$\varrho\frac{\partial\vec{q}}{\partial t} + \varrho\vec{q}\cdot\nabla\vec{q} = -\nabla P + \mu\nabla^2\vec{q} - 2\varrho\vec{\Omega}\times\vec{q} - \varrho\vec{\Omega}\times(\vec{\Omega}\times\vec{r}) \quad (7.2)$$

Here, $\vec{q}$ is the velocity vector, and $\vec{\Omega}$ is the angular velocity of the coordinate system. Equation (7.2) can be written in the non-dimensional form

$$\frac{\partial\vec{q}}{\partial t} + \vec{q}\cdot\nabla\vec{q} = -\nabla P + \frac{1}{\mathrm{Re}}\nabla^2\vec{q} - 2R_0\vec{\Omega}\times\vec{q} - R_0{}^2\vec{\Omega}\times(\vec{\Omega}\times\vec{r}) \quad (7.3)$$

Here, for simplicity, the same symbols are used for both the dimensional and non-dimensional variables. $R_e = \dfrac{\varrho U_0 l_0}{\mu}$ is the Reynolds number, U_0 is the velocity scale, and l_0 is the length scale. $R_0 = \dfrac{\Omega_0 l_0}{U_0}$ is the rotational number, and Ω_0 is the angular velocity

scale. Clearly, if $R_0 \sim O(1)$, then the Coriolis force and centrifugal force will have noticeable effects on flows through the momentum equation.

For turbulent flows, the system rotation not only affects flow fields through the momentum equation, it also affects flow fields by modifying the turbulent transport process. This can be seen through the Reynolds-stress equation. If the momentum equation, Eq. (7.2) is written in the tensor form

$$\varrho\frac{\partial u_i}{\partial t} + \varrho u_k\frac{\partial u_i}{\partial x_k} = -\frac{\partial p}{\partial x_i} + \mu\frac{\partial^2 u_i}{\partial x_k \partial x_k} - 2\varrho e_{ipk}\Omega_p u_k - \varrho e_{irs}\Omega_r(e_{spk}\Omega_p r_k) \quad (7.4)$$

The corresponding Reynolds-stress equations is

$$\frac{\partial \tau_{ij}}{\partial t} + \overline{u}_k\frac{\partial \tau_{ij}}{\partial x_k} = -\tau_{ik}\frac{\partial \overline{u}_j}{\partial x_k} - \tau_{jk}\frac{\partial \overline{u}_i}{\partial x_k} + \varepsilon_{ij} - \Pi_{ij} + \frac{\partial}{\partial x_k}[\nu\frac{\partial \tau_{ij}}{\partial x_k} + C_{ijk}] + Rot_{ij} \quad (7.5)$$

where

$$Rot_{ij} = \underset{(i)}{-2e_{ipk}\Omega_p\varrho\overline{u_j' u_k'}} - \underset{(ii)}{2e_{jpk}\Omega_p\varrho\overline{u_i' u_k'}} \quad (7.6)$$

Here, Rot_{ij} is the extra term caused by Coriolis force. It can be seen that the Reynolds-stress components τ_{ij} is affected through the interaction between the angular velocity and other Reynolds-stress components, and τ_{ij}, in turn affects the velocity field. Where nominally centrifugal force has no direct effect on τ_{ij}, as indicted by Eq. (7.5), it can affect τ_{ij} by changing the mean flow field through the momentum equations.

The turbulence kinetic energy equation can be obtained by taking the trace of Eq. (7.5). In fact, the trace of term (i) in Eq. (7.6) is

$$\begin{aligned} trace\ of\ (i) = -2\varrho[&e_{123}\Omega_2\overline{u_1' u_3'} + e_{132}\Omega_3\overline{u_1' u_2'} \\ &+ e_{231}\Omega_3\overline{u_2' u_1'} + e_{213}\Omega_1\overline{u_2' u_3'} \\ &+ e_{312}\Omega_1\overline{u_3' u_2'} + e_{321}\Omega_2\overline{u_3' u_1'}] \end{aligned} \quad (7.7)$$

$$
\begin{aligned}
&= -2\varrho[\Omega_2\overline{u_1'u_3'} - \Omega_3\overline{u_1'u_2'} \\
&\quad + \Omega_3\overline{u_2'u_1'} - \Omega_1\overline{u_2'u_3'} \\
&\quad + \Omega_1\overline{u_3'u_2'} - \Omega_2\overline{u_3'u_1'}] \\
&= 0
\end{aligned}
$$

Similarly, the trace of term (ii) in Eq. (7.6) is also zero. Accordingly, the turbulent kinetic equation is seemingly unchanged by the system rotation,

$$\varrho\frac{\partial K}{\partial t} + \varrho\overline{u}_j\frac{\partial K}{\partial x_j} = \mathcal{P} - \varrho\varepsilon + \frac{\partial}{\partial x_j}[\mu\frac{\partial K}{\partial x_j} - \frac{1}{2}\overline{\varrho u_i' u_i' u_j'} + \overline{p'u_j'}] \tag{7.8}$$

although the system rotation has no direct effect on the turbulent kinetic energy equation, its effect is implicitly included in $\mathcal{P}$ and ($\frac{1}{2}\overline{\varrho u_i' u_i' u_j'} + \overline{p'u_j'}$) terms.

With system rotation, the equation for the turbulent kinetic energy dissipation rate is

$$\varrho\frac{\partial \varepsilon}{\partial t} + \varrho\overline{u}_j\frac{\partial \varepsilon}{\partial x_j} = \mathcal{P}_\varepsilon - \Phi_\varepsilon + \mathcal{D}_\varepsilon + \mu\nabla^2\varepsilon + Rot(\varepsilon) \tag{7.9}$$

where

$$Rot(\varepsilon) = -4\nu e_{ipk}\Omega_p\overline{\frac{\partial u_i'}{\partial x_j}\frac{\partial u_k'}{\partial x_j}} \tag{7.10}$$

is the term caused by system rotation. Expanding this term, we get

$$Rot_{123} = -4\nu\Omega_2\overline{\frac{\partial u_1'}{\partial x_j}\frac{\partial u_3'}{\partial x_j}} \tag{7.11}$$

$$Rot_{132} = 4\nu\Omega_3\overline{\frac{\partial u_1'}{\partial x_j}\frac{\partial u_2'}{\partial x_j}} \tag{7.12}$$

$$Rot_{231} = -4\nu\Omega_3\overline{\frac{\partial u_2'}{\partial x_j}\frac{\partial u_1'}{\partial x_j}} \tag{7.13}$$

$$Rot_{213} = 4\nu\Omega_1 \overline{\frac{\partial u_2'}{\partial x_j}\frac{\partial u_3'}{\partial x_j}} \tag{7.14}$$

$$Rot_{312} = -4\nu\Omega_1 \overline{\frac{\partial u_3'}{\partial x_j}\frac{\partial u_2'}{\partial x_j}} \tag{7.15}$$

$$Rot_{321} = 4\nu\Omega_2 \overline{\frac{\partial u_3'}{\partial x_j}\frac{\partial u_1'}{\partial x_j}} \tag{7.16}$$

$$Rot(\varepsilon) = Rot_{123} + Rot_{132} + Rot_{231} + Rot_{213} + Rot_{312} + Rot_{321} = 0 \tag{7.17}$$

Interestingly, the system rotation has seemingly no direct effect on the turbulence dissipation rate equation, either. From the analysis above, it can be seen that the original K-ε model does not explicitly account for the rotational effect on turbulence transport process. To simulate rotating turbulent flows with K-ε model, modifications have to be made to account for the explicit effect of Coriolis force on turbulent transport process. In the next section, theoretical analyses will be conducted to investigate the mechanisms of Coriolis force affecting the fluid flow stability characteristics and the turbulent transport process, and identify the key parameter in the process.

7.3 Theoretical Analyses

7.3.1 Displaced Particle Analysis

The role of rotation on the stability of a shear flow is given by Tritton (1992) with the so called 'displaced particle analysis'. His argument related originally to the stability of laminar flows. However, it may also be an indication of the processes occurring with turbulent flows.

The specific configuration under consideration is an unidirectional shear flow in a rotational reference frame, with the vorticity associated with the shear parallel to that of the system rotation. We choose Cartesian coordinates, so that the mean flow is in the x-direction

with speed varying in the y-direction, $\boldsymbol{u} = (u(y), 0, 0)$. The system rotates with angular velocity Ω about the z axis. The shear vorticity is

$$\zeta = -\frac{\partial u}{\partial y} \tag{7.18}$$

and the effect of the rotation is indicated by the ratio of the background vorticity to this:

$$S = \frac{2\Omega}{\zeta} \tag{7.19}$$

This can be seen in Fig. 7.1 with positive $\frac{\partial u}{\partial y}$ and and positive Ω so that S is negative. Suppose that a small perturbation leads to a fluid particle being displaced a small distance δ in the y-direction. In its undisplaced position it has longitudinal velocity u_1 and when displaced it has velocity u_1'. There is a Coriolis force $2\varrho\Omega u_1'$ acting on it as shown in Fig. 7.1 (ϱ is fluid density). Similar Coriolis force $2\varrho\Omega u_2$ acts on an undisplaced particle at its new

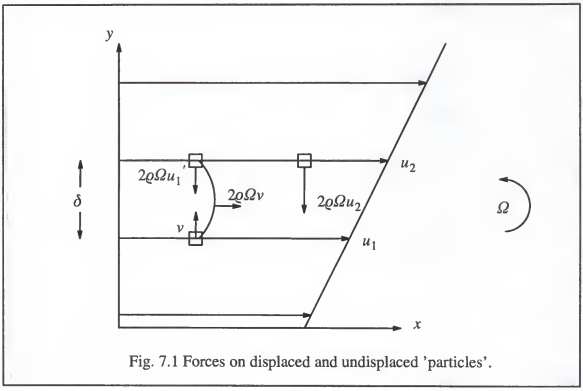

Fig. 7.1 Forces on displaced and undisplaced 'particles'.

position and thus will be balanced by a pressure gradient in the y-direction. That pressure gradient also acts on the displaced particle. Hence, the net force tends to displace the particle further if $u_1' < u_2$ and to return it towards its original position if $u_1' > u_2$, $u_1' \neq u_1$ because of the Coriolis force that acted whilst the particle was moving with velocity v in the y-direction

$$u_1' - u_1 = \int 2\Omega v dt = 2\Omega\delta \tag{7.20}$$

Hence,

$$\begin{aligned} u_1' - u_2 &= u_1' - u_1 + u_1 - u_2 \\ &= 2\Omega\delta - \frac{\partial u}{\partial y}\delta \\ &= -\frac{\partial u}{\partial y}(S+1)\delta \\ &= \zeta(S+1)\delta \end{aligned} \tag{7.21}$$

The net effect of the Coriolis and pressure forces on the displaced particle is a force

$$2\varrho\Omega(u_2 - u_1') = -\varrho\zeta S(S+1)\delta \tag{7.22}$$

Remembering that we are considering negative ζ (positive $\frac{\partial u}{\partial y}$) and negative S, we see that the particle tends to be displaced further if $S > -1$, restored if $S < -1$. Corresponding considerations for positive S show that the particle always tends to be restored in this case. Thus there is a destabilizing mechanism, to which the shear and Coriolis effects are both intrinsic, occurring in the range $-1 < S < 0$.

Bradshaw (1969) defined an equivalent gradient 'Richardson number' as

$$B = S(S+1) = \frac{-2\Omega(\partial u/\partial y - \Omega)}{(\partial u/\partial y)^2} \tag{7.23}$$

He first recognized the role of this dimensionless parameter in rotating flows by making an analogy with system rotation, streamline curvature, and buoyancy in turbulent shear flows.

Although Tritton's analysis is initially related to the stability of laminar shear flows rather than to turbulence, both lines of argument led to the same main result, showing that this fluid particle stability mechanism could be an indication of the effect of Coriolis force on turbulent shear flows. In summary, the effect of rotation is destabilizing when

$$-1 < S < 0 \tag{7.24}$$

i.e.,

$$B < 0 \tag{7.25}$$

Maximum destabilization occurs at $S = -\frac{1}{2}$ (i.e., $B = -\frac{1}{4}$), and restabilization of the flow may be expected when $S < -1$. On the other hand, positive S is always associated with stabilized flow.

7.3.2 Simplified Reynolds-Stress Analysis

The rotational effect on turbulent flow has been analyzed with the simple boundary-layer type flow (Johnston et al. 1972). It is useful to consider the rotation effect by looking at the equations for the rates of increase of the turbulent correlations $\overline{u'^2}, \overline{v'^2}, \overline{w'^2}$ and $-\overline{u'v'}$ as we follow time-mean particle motion. For the two-dimensional boundary layer case, the Reynolds-stress equations are

$$D(-\overline{u'v'})/Dt = \overline{v'^2}\partial\bar{u}/\partial y + (\overline{u'^2} - \overline{v'^2})2\Omega + [O.T.] \tag{7.26}$$

$$D(\overline{u'^2})/Dt = -\overline{u'v'}2\partial\bar{u}/\partial y - (-\overline{u'v'})4\Omega + [O.T.] \tag{7.27}$$

$$D(\overline{v'^2})/Dt = +0 + (-\overline{u'v'})4\Omega + [O.T.] \tag{7.28}$$

$$D(\overline{w'^2})/Dt = +0 + 0 + [O.T.] \tag{7.29}$$

The terms on the left-hand sides are the 'advection' or 'mean transport' terms. Just to the right of the equals sign are the production terms appearing in a non-rotating frame. Next on the right are the rotation 'production' terms, that enter the Eqs. (7.26–7.29) for rotating flows as a result of the Coriolis accelerations. Finally, all other terms are lumped together and

designated $[O.T]$. These terms include rate of viscous transport and dissipation, diffusion and convection by turbulence and the fluctuating pressure-strain interaction terms. All the $[O.T]$ terms are identical to their respective zero-rotation forms.

The equation for development of turbulent kinetic energy

$$K = \frac{1}{2}(\overline{u'^2} + \overline{v'^2} + \overline{w'^2}) \tag{7.30}$$

is

$$\frac{DK}{Dt} = (-\overline{u'v'})\frac{\partial \overline{u}}{\partial y} + [O.T.] = P + [O.T.] \tag{7.31}$$

Production of turbulence energy P is not explicitly dependent on Ω, but is implicitly affected by rotation through the effects Ω has on Reynolds-stress and mean shear.

For boundary layers and channel flows, peak levels of turbulence energy and stress are achieved in the regions close to the solid walls, i.e., the wall layers. In the wall layers the production and dissipation terms in Eqs. (7.26–7.29) are very large. The excess energy or stress produced locally is diffused, by the non-dissipation parts of the $[O.T]$ terms. The advection terms are usually very small and may be neglected in the wall layers. Therefore, the production terms are the only terms that can cause a local gain in the level of energy or stress. It is reasonable to assume, as a first approximation, that effects which increase (decrease) the approximate net production rates will also lead to an increase (decrease) in levels of turbulence energy and stress.

Let us apply this idea to the rotation-boundary layer case, see Fig. 7.2, where $\partial \overline{u}/\partial y$ is positive and the usual condition exist, i.e., $-\overline{u'v'} > 0$ and $\overline{u'^2} - \overline{v'^2} > 0$. Also assume, for the moment, that the rotation rate is positive, $\Omega > 0$. It is seen from the rotation production terms in Eq. (7.26) that positive rotation causes an increase in the net rate of production of turbulence stress. Consequently we expect that a layer with positive rotation

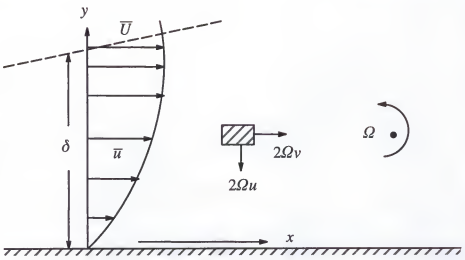

Fig. 7.2 Mean velocity for a two-dimensional boundary layer on a rotating surface. Vectors on paticle are Coriolis forces.

will have a higher level of stress $-\overline{u'v'}$ than an otherwise equivalent stationary layer. If $-\overline{u'v'}$ is increased with positive rotation then the production of turbulence energy P will be higher and consequently the level of energy K will increase. The direction of rotation is arbitrary. If it is negative, $\Omega < 0$, the same line of argument will indicate that rates of production of $-\overline{u'v'}$ and K will tend to decrease relative to conditions that would exist in equivalent stationary flows.

In summary, the examination of the production terms in Eq. (7.26–7.29) leads to conclusion that in wall layers the sign, and the magnitude, of rotation effects might be controlled by the local dimensionless parameter

$$S = -\frac{2\Omega}{(\partial\overline{u}/\partial y)} \tag{7.32}$$

so that when $S > 0$, decrease of $-\overline{u'v'}$ and K is expected, but when $S < 0$, increase of $-\overline{u'v'}$ and K is expected.

It is noted that, in the above analysis, the effect of $[O.T]$ terms is neglected. From the direct numerical simulation data (Kristoffersen and Andersson 1993), it can be seen that for the three-dimensional turbulent duct flow, $[O.T]$terms have some effects on turbulent structure, which is obvious for the correlation $\overline{w'^2}$ in the third direction. It is also clear that $-\overline{u'v'}$ and Ω affect each other. However, the result of the direct numerical simulation largely confirmed the above analysis. In the next section, the above analysis will be used to modify the K-ε equations to accommodate the system rotation effect.

7.4 The Model with Rotational Effect

From the above theoretical analyses, it can be seen how rotation affects the turbulence kinetic energy and Reynolds-stress, and the role of the Richardson number. A consistent approach with the K-ε model is to make the coefficients of the source terms in turbulent transport equations depend on the Richardson number. Except for the energy diffusion term, the turbulent kinetic energy equation is treated exactly in the K-ε model. The dissipation equation seems to be the obvious place to effect adjustments to the transport of length scales. The ε-equation itself is heuristically derived and therefore, offer some room for refinement. On the ground of seeking the simplest possible form, Launder et al. (1977) have assumed that the effects of streamline curvature on the length scale can be accommodated by making the effective value of $C_{\varepsilon 2}$ depend on the Richardson number. Howard et al. (1980), by the Bradshaw analogy (1969) between steramline curvature and system rotation, adopted model of Launder et al. (1977) for streamline curvature to rotating straight duct flow, making $C_{\varepsilon 2}$ depend on the rotational Richardson number. They used two forms of Richardson number

$$(i) \qquad R_i = \frac{-2\Omega(\partial u/\partial y - 2\Omega)}{(\partial u/\partial y)^2} \tag{7.33}$$

or

$$(ii) \qquad R_i = \frac{-2\Omega}{\partial u/\partial y} \tag{7.34}$$

Following Launder et al. (1977), the turbulent Richardson number is defined by replacing the mean flow time-scale represented by the denominator $(\partial u/\partial y)$ with a turbulent time-scale (K/ε). Thus the corresponding Richardson number is

$$(i) \qquad R_{it} = -2\Omega(\frac{K}{\varepsilon})^2(\frac{\partial u}{\partial y} - 2\Omega) \tag{7.35}$$

or

$$(ii) \qquad R_{it} = -2\Omega(\frac{K}{\varepsilon})^2\frac{\partial u}{\partial y} \tag{7.36}$$

Accordingly,

$$C_{\varepsilon 2} = 1.93(1 + C_c) \tag{7.37}$$

where

$$C_c = 0.2R_{it} \tag{7.38}$$

The coefficient of 0.2 is from Launder et al (1977). In the present work, Eq. (7.36) is adopted, because it appears to produce solutions in better agreement with the experimental result. (Howard et al. 1980). However, the formulation above is tested only for straight channel/duct flows. It is not coordinate invariant. In the present work, it is generalized to

$$R_{it} = -2\Omega(\frac{K}{\varepsilon})^2(\frac{\partial u}{\partial y} - \frac{\partial v}{\partial x}) \tag{7.39}$$

Here, $(\frac{\partial u}{\partial y} - \frac{\partial v}{\partial x})$ is the mean vorticity. For three-dimensional flow,

$$R_{it} = -2(K/\varepsilon)^2[\Omega_x(\frac{\partial v}{\partial z} - \frac{\partial w}{\partial y}) + \Omega_y(\frac{\partial w}{\partial x} - \frac{\partial u}{\partial z}) + \Omega_z(\frac{\partial u}{\partial y} - \frac{\partial v}{\partial y})] \tag{7.40}$$

or

$$R_{ii} = 2(\frac{K}{\varepsilon})^2 e_{ipj}\,\Omega_p \frac{\partial u_i}{\partial x_j} \tag{7.41}$$

The final form of modified K-ε equations are

$$\frac{\partial K}{\partial t} + \overline{u}_i \frac{\partial K}{\partial x_i} = P - \varepsilon + \frac{\partial}{\partial x_i}\left(\frac{\nu_T}{\sigma_K}\frac{\partial K}{\partial x_i}\right) \tag{7.42}$$

$$\frac{\partial \varepsilon}{\partial t} + \overline{u}_i \frac{\partial \varepsilon}{\partial x_i} = C_{\varepsilon 1}\frac{\varepsilon}{K}P - C_{\varepsilon 2}(1 + C_c)\frac{\varepsilon^2}{K} + \frac{\partial}{\partial x_i}\left(\frac{\nu_T}{\sigma_\varepsilon}\frac{\partial \varepsilon}{\partial x_i}\right) \tag{7.43}$$

7.5 Assessment of the Modified Model

7.5.1 Rotating Channel Flow

In most practical rotating turbulent flow situations, Coriolis forces associated with the rotation act directly on both the mean motion and turbulent fluctuations. Their action on the mean flow induces a secondary flow while their effect on turbulence affects the mixing process. Since secondary motions alter the turbulent stress field and modifications to the turbulence structure affects the mean velocity profiles, the two effects become inextricably entwined. However, in one case, the modification to the turbulence by Coriolis force can be looked at in isolation: that of flow between infinite rotating parallel planes, the mean Coriolis force in the direction normal to the plane being everywhere balanced by the pressure gradient. Johnston et al. (1972) conducted experiments on water flowing in a rotating channel with an aspect ratio of height to width of 7:1. This high aspect ratio channel reduced the effect of the secondary flow on the mainstream velocity profile in order to isolate other effects of rotation. In the test section of the channel, fully developed flow was indicated by the measurement. The velocity profiles ware measured at the channel center plane, where the flow was observed to be two-dimensional.

In the present study, a two-dimensional rotating channel flow simulation is conducted. The configuration is schematically shown in Fig. 7.3. It is a straight, radially

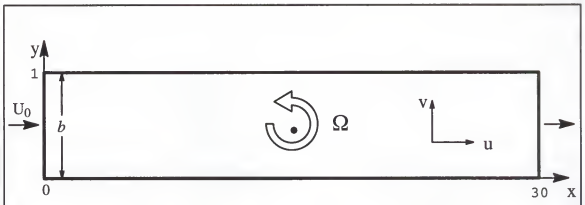

Fig. 7.3. Schematic of the rotating duct (Rotational number $R_0 = Wb/U_0$). The total channel length x/b is 30.

rotating channel with length to width ratio of 30. For this particular flow, the no-slip condition on both the top and bottom walls causes the velocity gradients in the upper and lower wall regions to be of opposite signs, which, in turn, creates opposite effects in the ε-equation. For the flow tested, the Reynolds number is 11,500 and the rotation number, as defined in Eq. (7.3) varies from 0 to 0.21. Uniform flow is specified at the entrance, and zero gradient of dependent variables is applied at the outlet. A grid system of 121x41 nodes with the second-order upwind scheme was found to be adequate. The following points are noted:

(i) Figure 7.4 shows the u-velocity, pressure, and eddy viscosity profiles near the channel exit predicted with the standard K-ε model with and without rotational modification in the ε-equation. Without the rotational modification, the velocity profile is symmetric because the rotation number is modest. However, with the rotational modification, the velocity profile is asymmetric due to the aforementioned sign reversal of the velocity gradient between the upper and lower wall regions. The velocity gradient is negative in the upper wall region, creating a smaller sink term in the ε-equation. On the other hand, the positive velocity gradient in the lower region alters the balance among different terms of the ε-equation, and the eddy viscosity in an opposite way. It should be noted that the quantitative influence of the Richardson number on ε is not straight forward to assess because the production and dissipation terms are also functions of K and ε.

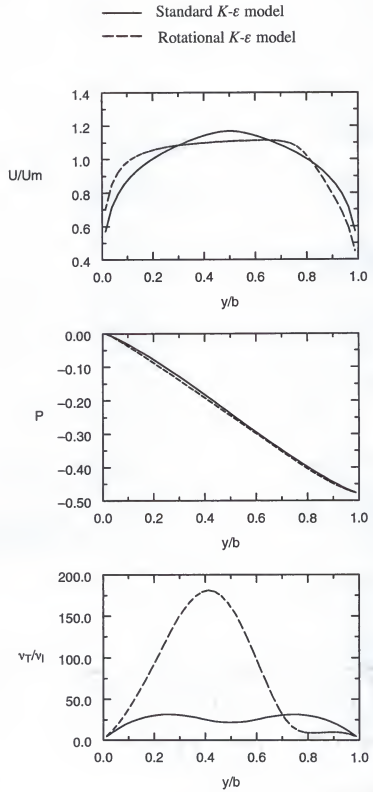

Fig. 7.4. Effects of coordinate rotation on predicted profiles of u-velocity, pressure and normalized eddy viscosity at x/b = 26. (Re = 1.15×10^4, $R_0 = 0.21$).

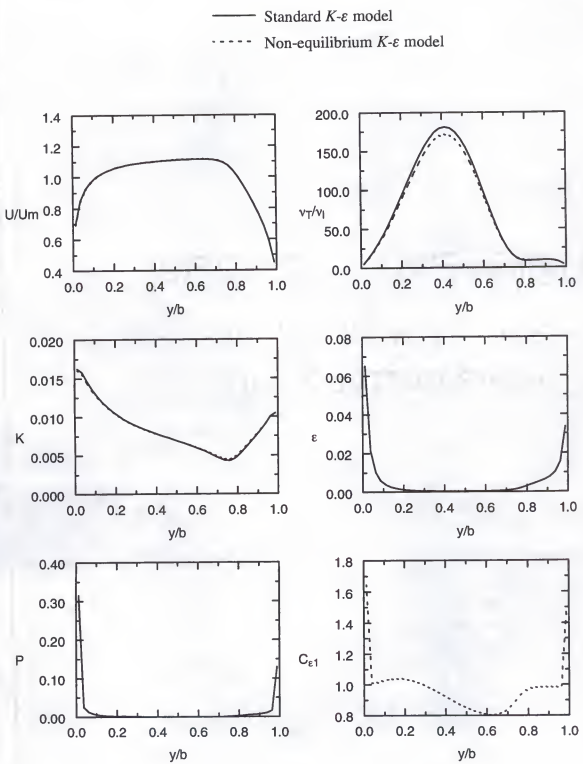

Fig. 7.5. Comparisons of predictions based on the standard and the non-equilibrium model coefficients, both with rotational modification, at x/b = 26. ($Re = 1.15x10^4$, $R_0 = 0.21$).

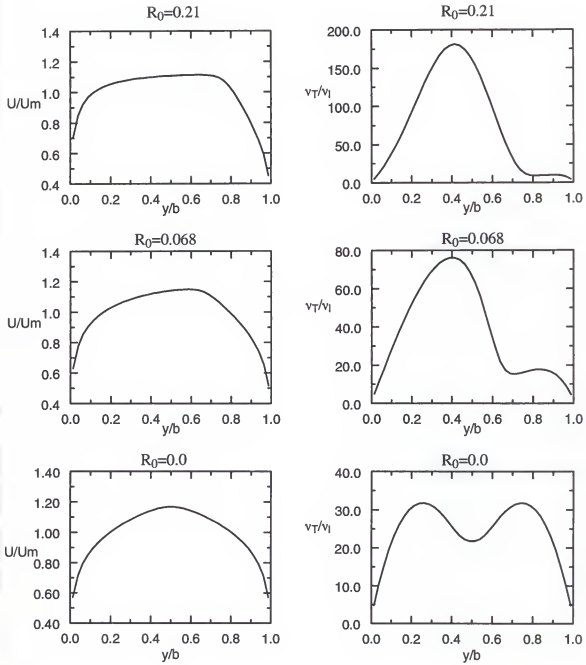

Fig. 7.6. Effects of rotation number R_0 on u-velocity and normalized viscosity at x/b = 26. (Re = 1.15×10^4).

(ii) The pressure profiles predicted with the two turbulence models are very close, again indicating that the effect of turbulent variables on pressure is small with this configuration.

(iii) Figure 7.5 compares the solutions obtained with the coefficients of the non-equilibrium and standard models with the rotational modification made to both models. The mean velocity profiles and production and dissipation terms are virtually indistinguishable between the two models, in spite of the nonuniform profile of $C_{\varepsilon 1}$ and the differences in eddy viscosity. The reason that the effect of span-wise rotation dominates over the $C_{\varepsilon 1}$ variation is that the production of K is negligible except in the wall regions. One should note that the present flow problem is a simple channel flow, and hence, is not expected to be sensitive to the non-equilibrium modification. Because of this, we can separate the influences of non-equilibrium between the production and consumption of K and ε and span-wise rotation.

(iv) Figure 7.6 presents the effect of different rotational numbers on the predicted flow structures with the rotational modifications made to the non-equilibrium model. Consistent with the results reported by Johnston et al. (1972), with no rotation, the velocity profile is symmetric; with the increasing rotational number, progressive departure from the symmetric profile is observed. Furthermore, the maximum eddy viscosity also increases as the rotational number becomes higher. However, the location of the peak eddy viscosity with both non-zero rotational numbers is unchanged. This location is also different from the location of the maximum u-velocity.

7.5.2 Rotating Backward Facing Step Flow

In this section, a two-dimensional rotating backward facing step turbulent flow is investigated. The rotation axis is perpendicular to the flow plane and is placed at the left lower corner of the flow domain. The flow field of the non-rotating backward facing step flow consists of 2 distinct region: (1) recirculating region, and (2) attached flow region. The system rotation can modify the flow structure in both regions. In this configuration, the flow

is not symmetric, and the flow direction interacts with rotational force to have different effects on the flow field. Here, a comparison of the standard K-ε model and rotational K-ε model with rotating recirculating flow will be conducted. The effect of rotational direction on different flow regions will be investigated.

The test case to be considered here is turbulent flow over a backward facing step with the expansion ratio E (step height to overall channel height) of 1/3 and the Reynolds number of 132,000 based on the inlet flow mean velocity and the channel height. The channel length is 24 times of the step height. A 121 x 91 mesh system is used. The second-order upwind scheme is used for the convection terms.

Two rotational speeds are chosen, $\Omega = 0.21$ and $\Omega = -0.21$. Here, the counter-clockwise rotation is defined as positive rotation. For each rotational speed, both standard K-ε model and rotational K-ε model will be tested. For each case, the streamline, pressure distribution, velocity, vorticity and turbulent viscosity profiles at 3 selected locations will be presented and compared. First of all, a non-rotating flow is computed. The reattachment length is x/H=5.4. According to this result, the 3 locations selected for comparison are x/H=2.0, x/H=6.0, and x/H=20.0. The first location is inside the recirculating zone of the non-rotating case. The second location is just behind the reattachment point, and the third location is far behind the reattachment point and is in attached flow zone. The purpose is to assess the rotational effect on these three different regions.

7.5.2.1 Counter-clockwise (positive) rotation, $\Omega = 0.21$

For comparison, the streamlines and pressure distributions for 3 analyses are presented, namely, the non-rotating flow, the rotating flow with standard K-ε model (SMD) and the rotating flow with rotational K-ε model (RMD). Figure 7.7 gives the streamlines for the three flows. The reattachment length for rotating flow with SMD is the same as that of the non-rotating flow, x/H=5.4. As already discussed, the standard K-ε model does not respond to body force. On the other hand, for rotating flow with RMD, the reattachment

(a) Non-rotating flow with standard K-ε model

(b) Rotating flow with standard K-ε model

(c) Rotating flow with rotational K-ε model

Fig. 7.7. Streamlines for non-rotating and rotating flows with different K-ε models. Ω=0.21 for rotating flow.

(a) Non-rotating flow with standard K-ε model

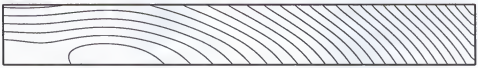

(b) Rotating flow with standard K-ε model

(c) Rotating flow with rotational K-ε model

Fig. 7.8. Pressure distributions for non-rotating and rotating flows with different K-ε models. Ω=0.21 for rotating flow.

length is x/H=3.2, which is greatly reduced. The pressure distributions are presented in Fig. 7.8. It can be seen that, for non-rotating flow and rotating flow with SMD, although there is not obvious difference in streamlines, there is a big difference in pressure distributions. This is because in the rotating flow, the Coriolis force and the centrifugal force caused by the system rotation are absorbed by the pressure field. For rotating flow with RMD, there are obvious differences in the pressure distribution compared with the rotating flow with SMD, especially in the recalculating region. This is because with RMD, the rotational effect on turbulent structure changes the velocity field as well as the pressure field.

The profile comparisons for the mean u, v velocity, vorticity $\omega = \partial v/\partial x - \partial u/\partial y$ and eddy viscosity at the 3 locations are shown in Fig. 7.9 , 7.10 and 7.11, respectively. It is noted that, for both non-rotating flow and rotating flow with SMD, the profiles are identical. The standard K-ε model can not predict the rotational effect on turbulent structure and velocity field in this configuration, as in the case of fully attached channel flow presented in the last section. Hence, only the results of rotating flow with SMD and RMD are presented.

Figure 7.9 shows the profiles at location 1 (x/H= 2.0), which is in the recirculating region. From u profile at this location, it can be seen that the flow region can be divided into two zone: (1) a recirculating zone, which is from y/b=0.0 to around 0.4, (2) an attached flow zone, which is from y/b=0.4 to 1.0. In the recirculating zone, the vorticity $\omega = \frac{\partial v}{\partial x} - \frac{\partial u}{\partial y}$ is negative, and Ω is positive. $S = \frac{\Omega}{(\partial v/\partial x - \partial u/\partial y)}$ is negative. Therefore, turbulent stress $-\overline{u'v'}$ will be increased according to the analysis and model in section 7.2 and 7.4. This can be observed from the profile of the eddy viscosity. In the recirculating zone, the peak value of eddy viscosity is approximately tripled with RMD compared with result of SMD. In the attached flow zone, ω is almost zero, there is almost no difference regarding the eddy viscosity with the two different models. With the rotational effect on eddy viscosity, both the u velocity and v velocity are changed. Near the lower wall, the u velocity is negative. With

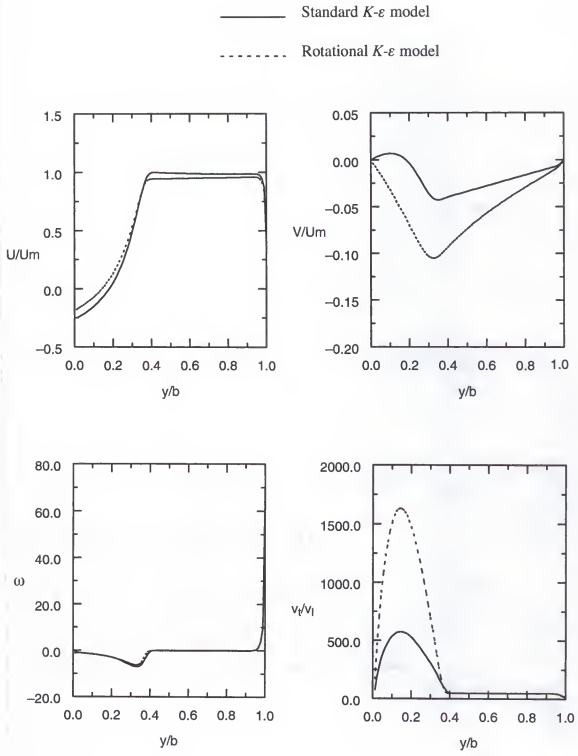

Fig. 7.9. Profile comparisons of selected quantities resulting with the different K-ε models at x/H = 2.0. $\Omega = 0.21$.

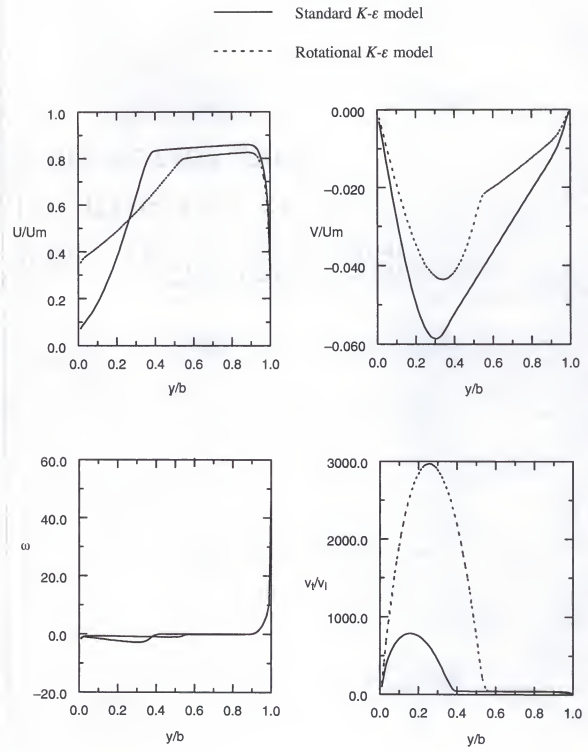

Fig. 7.10. Profile comparisons of selected quantities resulting with the different K-ε models at x/H = 6.0. $\Omega = 0.21$.

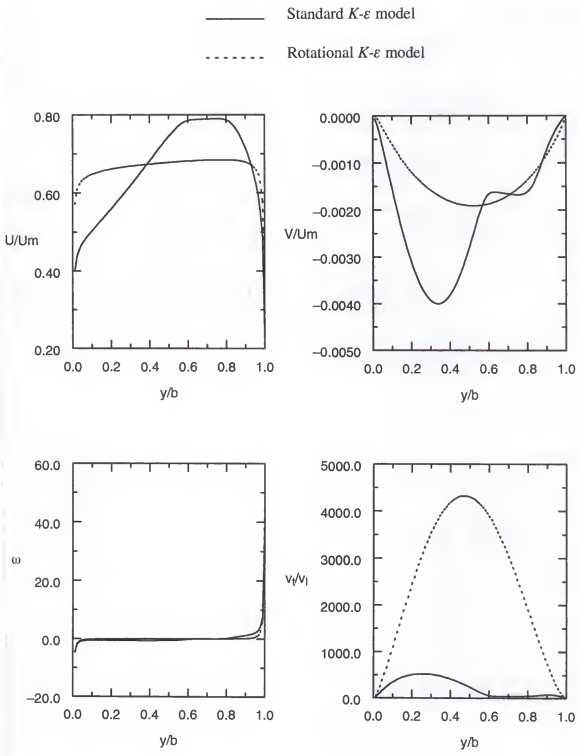

Fig. 7.11. Profile comparisons of selected quantities resulting with the different K-ε models at x/H = 20.0. $\Omega = 0.21$.

the rotational model, the magnitude of u velocity is reduced. The v velocity near the lower wall is changed from positive to negative with the rotational model.

The profiles at location 2 (x/H= 6.0), are presented in Fig. 7.10. For non-rotating flow and rotating flow with SMD, this location is just behind the simulated reattachment point and the flow is attached. At the pressure side of this location, i.e., near the lower wall, the vorticity is still negative, which is opposite the direction of rotation. With the rotational model, the eddy viscosity there is greatly enhanced compared to the result with SMD. Correspondingly the u velocity near the lower wall is increased with the increased eddy viscosity. The magnitude of velocity at this location is reduced.

Figure 7.11 shows the profiles at location 3 (x/H=20.0). At the location, the flow is more developed and closer to the fully developed channel flow compared to the previous two locations. With SMD, the u velocity has a large deficit near the lower wall. With RMD, this deficit is reduced, because of the increased eddy viscosity. Qualitatively, at this location, there are some similarities between this flow and the rotating channel flow presented in the last section regarding the rotational effect on turbulent viscosity and the u velocity profile.

Overall, it can be seen that, with the rotational model, the turbulent viscosity near the lower wall (pressure side) is increased, regardless of whether it is in the recirculating region or the attached flow region. The direction and the strength of the system rotation with respect to those of flow vorticity affect the turbulent flow structure. The increased eddy viscosity near the lower wall helps the flow reattach the lower wall and reduce the reattachment length.

7.5.2.2 Clockwise (negative) rotation, $\Omega = -0.21$

Figure 7.12 shows the streamlines of the three flows. Again, the non-rotating flow and the rotating flow with SMD have the same reattachment length. For rotating flow with RMD, the predicted reattachment length is x/H=15.6, which is greatly increased compared that of the non-rotating flow. The pressure distributions for the three simulated flows are presented in Fig. 7.13. With SMD, the pressure distribution for rotating flow is, again, quite different from that of the non-rotating flow, although the streamlines are very similar. The

(a) Non-rotating flow with standard K-ε model

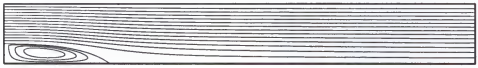

(b) Rotating flow with standard K-ε model

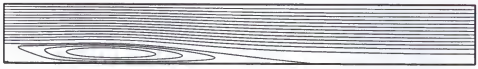

(c) Rotating flow with rotational K-ε model

Fig. 7.12. Streamlines for non-rotating and rotating flows with the different K-ε models. Ω=–0.21 for rotating flow.

(a) Non-rotating flow with standard K-ε model

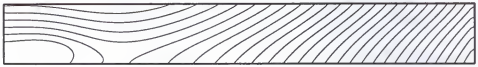

(b) Rotating flow with standard K-ε model

(c) Rotating flow with rotational K-ε model

Fig. 7.13. Pressure distributions for non-rotating and rotating flows with the different K-ε models. Ω=–0.21 for rotating flow.

Coriolis force for the momentum equations is balanced by the pressure gradient, and the velocity field is left unchanged. For rotating flow with RMD, the pressure field is different from that of the flow with SMD. The rotational effect on the velocity as well as pressure field is observed.

The profiles at the 3 locations are presented in Fig. 7.14, 7.15 and 7.16, respectively. Again, the difference between the non-rotating flow and rotating flow with SMD is indistinguishable. Only the latter ones are presented along with those of flow with RMD.

Figure 7.14 shows the result at location 1. At the suction side, i.e., the lower wall, the vorticity ω is negative, and the rotating speed Ω is also negative. $S = \frac{\Omega}{\omega}$ is positive. The Reynolds-stress $-\rho\overline{u'v'}$ or eddy viscosity is expected to decrease. This is observed in the eddy viscosity profile with the rotational model: the eddy viscosity is greatly reduced at the suction side. At the pressure side, the vorticity is very small, and close to zero. Correspondingly, there is almost no change in eddy viscosity. The u velocity profiles are observed to have obvious differences at the suction side between the two turbulence models. With RMD, the u velocity near the lower wall is closer to the stagnation state. With SMD, the v velocity is negative across the channel, except for a small region near the lower wall. With RMD, the v velocity is positive across the channel.

The profiles at location 2 are displayed in Fig. 7.15. With RMD, the peak value of the eddy viscosity on the suction side is reduced by almost a factor of 4. From the u velocity profile, it can be seen that, with RMD, the u velocity near the lower wall is negative, which implies that this location is still in the recirculating region. With SMD, this location is outside the recirculating region, and the flow is fully attached.

Figure 7.16 presents the profiles at location 3. With RMD, the eddy viscosity is greatly reduced at the suction side, and increased at the pressure side, at this location. For the u velocity profile, it is observed that, near the suction side, the u velocity deficit is increased due to the reduction of the turbulent viscosity. Near the pressure side, the u velocity

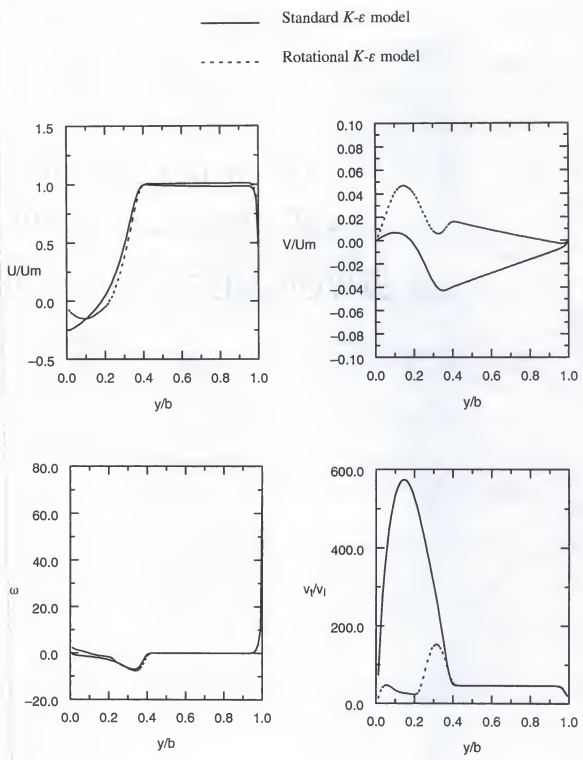

Fig. 7.14. Profile comparisons of selected quantities resulting with the different K-ε models at x/H = 2.0. $\Omega = -0.21$.

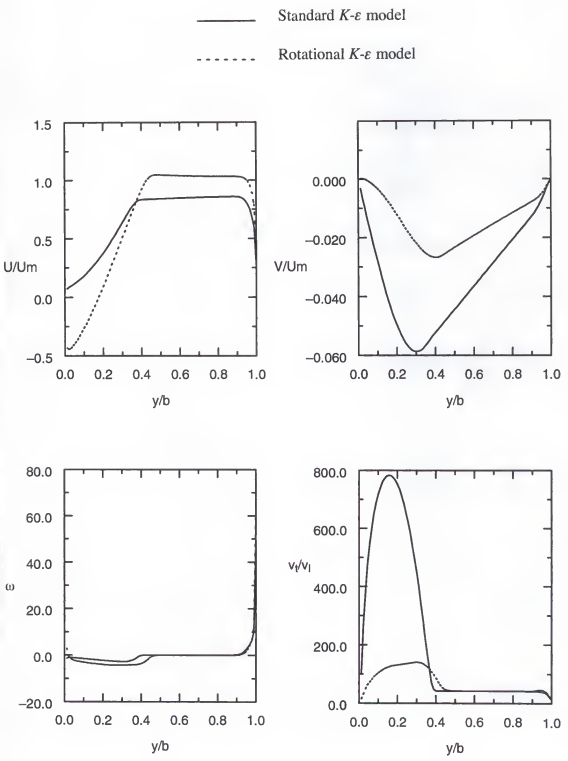

Fig. 7.15. Profile comparisons of selected quantities resulting with the different K-ε models at x/H = 6.0. $\Omega = -0.21$.

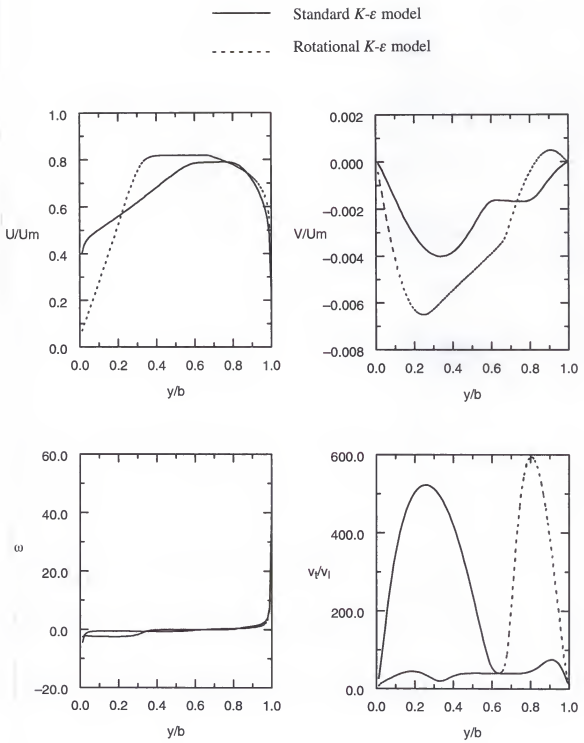

Fig. 7.16. Profile comparisons of selected quantities resulting with the different K-ε models at x/H = 20.0. $\Omega = -0.21$.

deficit is reduced due to the increase of turbulent viscosity. Overall, the negative rotation decreases the turbulent viscosity at the suction side and increases it at the pressure side. At the suction side, the reduction of turbulent viscosity increases the reattachment length of the recirculating zone .

In summary, for the backward facing step flow, the standard K-ε model can not predict the rotational effect on the velocity field. The Coriolis force is balanced by the pressure field change, and would not affect the velocity field. The rotational K-ε model can predict the rotational effect on velocity fields for both attached and recirculating flows. The system rotation can increase or decrease the reattachment length depending on the rotation direction.

7.5.3 Flow Simulation in A Torque Converter

The torque converter simulated here consists of three stages. In the present configuration, the pump stage has 31 blades, the turbine stage has 23 blades and the reactor stage has 24 blades. The pump and turbine have sheet blades of uniform thickness while the reactor has cast blades with significant thickness, camber and twist. Three different mesh sizes are used in the analysis to determine the sensitivity of the solution the the mesh resolution. The most coarse mesh consists of a total of 22,974 grid points (14x16x29,14x16x29,14x31x23 for pump, turbine and reactor respectively). At this low resolution, the true blade shape is not accurately represented. The median mesh consists of a total of 68,838 grid points (22x18x49,22x18x49,22x35x39 for pump, turbine and reactor respectively). The fine mesh consists of a total of 128,209 grid points (29x28x49,29x28x49,29x43x39 for pump, turbine and reactor respectively). The working fluid is standard transmission oil at a temperature of 110^{o} C. The fluid density is 818.94 Kg/M^{3}. and the dynamic viscosity is 0.00531 Kg/M/Sec.

The analysis of the flow in the torque converter assembly is carried out as a collaboration effort with Ford Motor Company, using the STAR–CD code. STAR–CD is a finite volume based fluid dynamic analysis program which solves the nonlinear set of

equations formed by the discretization of the conservation equations of mass and momentum. STAR–CD allows the flow problem to be posed and solved in a rotating reference frame, i.e., in a coordinate system in which the blades of a rotating component (like a pump rotor) are at rest. All the body force terms resulting from the rotation of the coordinate system to the momentum equations are handled internally to the code.

In the problem of the torque converter, there are three different components rotating at three different angular speeds. Thus no one coordinate system rotation would freeze all the motions. The code allows different parts of the model be cast in different coordinate systems. This reduces the problem to a set of three sub-problems solved in parallel. The three sub-problems are solved together by using the MULTIPLE FLUID STREAM capability of STAR–CD (Jonnavithula 1992). Thus it no longer matters that the three staged have different numbers of blades. A single repeatable sector from each stage can be modeled, with cyclic boundary conditions on the "cut" faces. The shell and core surfaces and the blade surfaces, can be modeled as stationary walls in the rotating reference frame.

The turbulence is modeled with the K-ε model with rotational modification, as presented from Eq. (7.41–7.43). This model has been incorporated in the STAR–CD code by the present authors. In the case studied, the pump speed is fixed at 1000 RPM, and the turbine speed is 0. In the following, the result from the median mesh is presented. The three-dimensional grid is presented in Fig. 7.17. The velocity vectors and pressure distributions at the blades are shown in Fig. 7.18 and 7.19. Figure 7.18 shows the suction side of the pump and reactor, and the pressure side of the turbine. It is observed that on the suction side of the pump, the rotational effect reduced the recirculation region, and modified the pressure distribution. Figure 7.19 presents the pressure side of the pump and reactor, and the suction side of the turbine. It can be seen that the rotational effect expanded the low pressure region on the suction side of the turbine. From the above results, the rotational effect on the flow structures is clearly observed.

7.6 Concluding Remarks

In this chapter, the K-ε turbulence model with rotational effect is investigated. The momentum equations and the Reynolds-stress equations in the rotational frame are firstly presented. It has been shown that the Coriolis force and the centrifugal force can explicitly affect the velocity and pressure fields through the momentum equations. The turbulent structure can be modified explicitly by the interaction between the Coriolis force and the Reynolds stresses and implicitly modified by the centrifugal force through interacting with velocity field. The analysis of K and ε equations shows that the rotation effects the turbulent quantities only indirectly through the Reynolds-stress term. This indirect effect from rotation can not be represented in the original K-ε model. The displaced particle stability analysis and the simplified Reynolds-stress analysis clearly identify the role of system rotation interacting with flow vorticity in the process of system rotation affecting turbulence structure and the corresponding nondimensional parameter. Based on the theoretical analyses, the rotational effect on the turbulence structure can be modeled through the modification of the source term of the ε equation. In the present investigation, The K-ε model with rotational effect proposed by Howard et al. (1980) has been extended to the three-dimensional coordinates. The modified K-ε model with rotational effect can predict the correct trend for the channel flow, for both the velocity profile and the turbulent viscosity. For the backward facing step flow, the rotational effect on recirculating flow structure is clearly observed. Finally, the rotational K-ε model has been applied to the three-dimensional torque converter flow simulation.

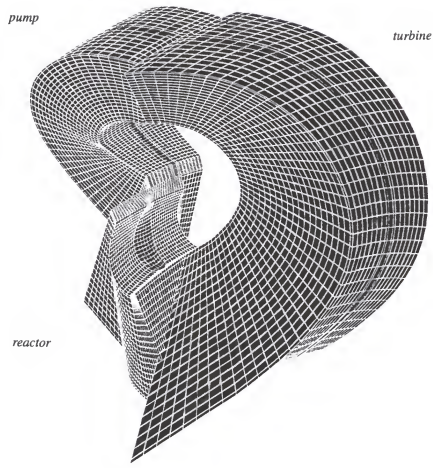

Fig. 7.17 The grid for 3-D torque converter flow domain.

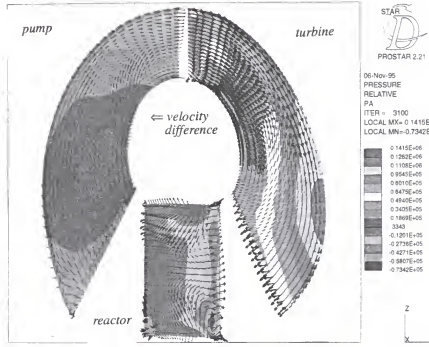

(a) standard K–ε model

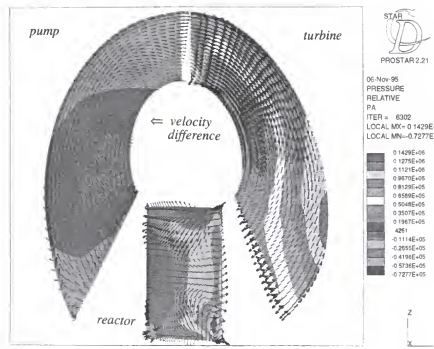

(b) rotational K–ε model

Fig. 7.18 The velocity vector and pressure distribution on the suction side of the pump and reactor, and pressure side of the turbine

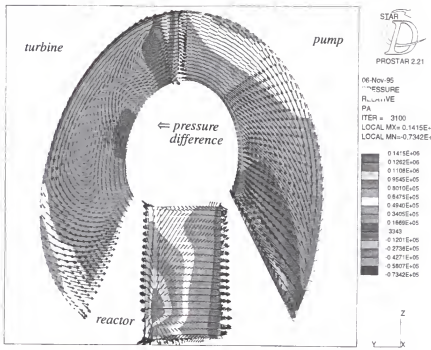

(a) standard K–ε model

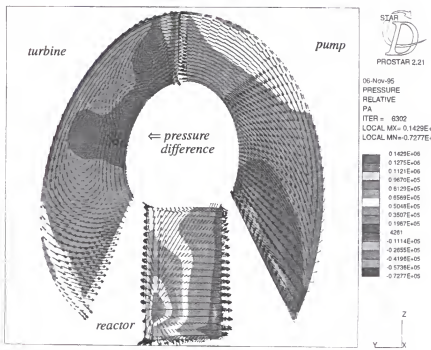

(b) rotational K–ε model

Fig. 7.19 The velocity vector and pressure distribution on the pressure side of the pump and reactor, and the suction side of the turbine.

CHAPTER 8
SUMMARY AND SUGGESTIONS FOR FUTURE WORK

A pressure-based multi-block grid method for solving incompressible viscous flows in non-orthogonal curvilinear coordinate is presented. Basically, the method employs a finite volume approach and a staggered grid, and solves the governing equations in a sequential manner. Different interface conditions for solving the model equations and Navier-Stokes equations in multi-block domain are analyzed. The effects of the grid interface treatments on the convergence, accuracy and uniqueness aspects are discussed. For the momentum equations, direct interpolation of the dependent variables between blocks can be used. For the pressure correction equation, it is found that with a locally conservative interface treatment of mass flux with second or higher order of accuracy, both the Neumann-Neumann and Neumann-Dirichlet boundary conditions can yield solutions of comparable accuracy. Compared to the Neumann-Neumann type boundary condition, the mixed Neumann-Dirichlet type boundary condition allows a better pressure coupling between grid blocks, resulting in a faster convergence.

Besides interface treatment, data structure is important issue for the multi-block computation. Tasks of information transfer across discontinuous grid interfaces can be completed by two basic operations: (1) interpolation between grid vertices or grid face centers, and (2) interpolation with conservative correction for fluxes between grid faces, which are based on the intersection test among arbitrarily oriented line segments in two-dimensional space. It is demonstrated that the connectivity among grid blocks, grid boundaries, boundary segments and control volumes at the grid interfaces can be set up automatically. The proposed data structure is incorporated with the flow solver to form a

complete multi-block flow analysis software for analyzing incompressible flows in complex configurations.

Future work should involve the extension of the method to multilevel adaptive grid method to tackle the complex problem with multiple length scales. This will involve the combination of the current interface treatment method with a posterior error estimation method and a coordinate procedure dealing with the organization of the grids at different levels. This future work, should also be combined with parallel processing to enhance the computational efficiency.

Regarding physical modeling, the closure issues of the K-ε turbulence model are discussed. A comparative study of the original and non-equilibrium K-ε models is conducted with three recirculating flow cases: (a) the backward facing step flow (where separating point is fixed), (b) the hill flow (where separation point is not fixed), and (c) the 3-D diffuser flow (3-D flow with streamline curvature). It is observed that the equilibrium condition—which is the basis of the original K-ε model, is not satisfied for some flow conditions, especially, separating flows. The non-equilibrium K-ε model treats the production term and dissipation term of the turbulent kinetic energy in a manner responsive to the local flow structure, and produces encouraging results for complex flow computations tested. However, further optimization of $C_{\varepsilon 1}$, $C_{\varepsilon 2}$, and C_{μ} will be desirable.

In order to handle turbomachinery flows, the K-ε turbulence model with rotational effects is also investigated. With the unmodeled K- and ε-equations, the effects of the system rotation on the turbulent structures appear only indirectly through the Reynolds-stress terms, which are not accounted for in the original K-ε model. The rotational effect can be modeled through the modification of the source term in the ε-equation in the form of a rotation number. A model investigated by Howard et al. (1980) is extended to three dimensional coordinates. This modified K-ε model with modified treatments for the non-equilibrium and rotational effects is employed to compute the three-dimensional torque converter flow in a practical design configuration.

Future work regarding the turbulence modeling may include several aspects. Firstly, further optimization of $C_{\varepsilon 1}$, $C_{\varepsilon 2}$, and C_{μ} terms based on a more broad experimental data base is needed. Secondly, better wall treatments beyond wall function, e.g., the low Reynolds number K-ε model, with which the momentum equations can be integrated directly to the wall, can be investigated. Furthermore, current investigation of the K-ε model partially lay the foundation for more comprehensive models, e.g., Reynolds-stress and algebraic Reynolds-stress models, which need to solve the ε-equation. These models can account for the anisotropic effect of the Reynolds-stress components, but their performance remains to be assessed.

REFERENCE

Akselvoll, K. and Moin, P. 1995 Large Eddy Simulation of Turbulent Confined Co-Annular Jets and Turbulent Flow over a Backward Facing Step, Report No. TF–63, Thermosciences Division, Dept. of Mechanical Engineering, Stanford University.

Almeida, G.P., Durao, D.F.G. and Heitor, M.V. 1993 Wake Flow Behind Two-Dimensional Model Hills, *Exp. Thermal Fluid Sci.*, 7, 87.

Baldwin, B.S. and Lomax, H. 1978 Thin-Layer Approximation and Algebraic Model for Separated Turbulent Flows, *AIAA Paper* No. 78–257.

Bardina, J., Ferziger, J.H. and Rogallo 1985 Effect of Rotation on Isotropic Turbulence: Computation and Modelling, *J. Fluid Mech.*, 154, 321–336.

Benek, J.A., Sterger, J.J. and Dougherty, F.C. 1983 A Flexible Grid Embedding Technique with Application to the Euler Equations, *AIAA–83–1944–CP.*

Berger, M.J. 1987 On Conservation at Grid Interfaces, *SIAM J. Numer. Anal.*, 24, No. 5, 967–984.

Blosch, E., Shyy, W. and Smith, R.W. 1994 The Role of Mass Conservation in Pressure-Based Algorithms, *Numer. Heat Transf.*, 24, 415–430.

Braaten, M.E. and Connell, S.D. 1996 Three-Dimensional Unstructured Adaptive Multigrid Scheme for the Navier-Stokes Eqauations, *AIAA J.*, 34, 281–290.

Braaten, M.E. and Shyy, W. 1986 A Study of Recirculating Flow Computation Using Body-Fitted Coordinates: Consistency Aspect and Mesh Skewness., *Numer. Heat Transf.*, 9, 559–574.

Bradshaw, P. 1969 The Analogy between Streamline Curvature and Buoyancy in Turbulent Shear Flow, *J. Fluid Mech.*, 36, 177–191.

Cebeci, T. and Smith, A.M.O. 1974 *Analysis of Turbulent Boundary Layers*, Academic Press, New York.

Chen, Y.S. and Kim, S.W. 1987 Computation of Turbulent Flows Using an Extended K-ε Turbulence Closure Model, *NASA CR–179204*.

Chesshire, G. and Henshaw W.D. 1990 Composite Overlapping Meshes for the Solution of Partial Differential Equations, *J. Comp. Phys.*, 90, 1–64.

Chesshire, G. and Henshaw W.D. 1994 A Scheme for Conservative Interpolation on Overlapping Grids, SIAM *J. Sci. Comput.*, 15, No. 4, 819–845.

Chorin, A.J. 1967 Numerical Solution of the Navier-Stokes Equations, *Mathematics of Computation*, 22, 745–762.

Galmes, J.M. and Lakshminarayana, B. 1984 Turbulence Modeling for Three-Dimensional Shear Flows over Curved Rotating Bodies, *AIAA J.*, 22, 1420–1428.

Ghia, U., Ghia, K.N. and Shin, C.T. 1982 High-Re Solutions for Incompressible Flow Using the Navier-Stokes Equations and a Multigrid Method, *J. Comp. Phys.*, 48, 387–411.

Gropp, W.D. and Keyes, D.E. 1992a Domain Decomposition Methods in Computational Fluid Dynamics, *Int. J. Numer. Meths. Fluids,* 14, 147–165.

Gropp, W.D. and Keyes, D.E. 1992b Domain Decomposition with Local Mesh Refinement, *SIAM J. Sci. Stat. Comput.*, 13, No. 4, 967–993.

Henshaw, W.D. 1994 A Fourth-Order Accurate Method for the Incompressible Navier-Stokes Equations on Overlapping Grids, *J. Comp. Phys.*, 113, 13–25.

Hinatsu, M. and Ferziger, J.H. 1991 Numerical Computation of Unsteady Incompressible Flow in Complex Geometry Using a Composite Multigrid Technique, *Intl. J. Numer. Meths Fluids*, 13, 971–997.

Hinze, O. 1959 *Turbulence*, McGraw Hill, New York.

Howard, J.H.G., Patankar, S.V. and Bordynuik, R.M. 1980 Flow Prediction in Rotating Ducts Using Coriolis-Modified Turbulence Models, *J. Fluids Eng.*, 102, 456–461.

Issa, R. I. 1985 Solution of the Implicitly Discretised Fluid Flow Equations by Operator Splitting, *J. Comp. Phys.*, 61, 40–65.

Johnston, J.P., Halleen, R.M. and Lezius, D.K. 1972 Effects of Spanwise Rotation on the Structure of Two–Dimensional Fully Developed Turbulent Channel Flow, *J. Fluid Mech.*, 56, 533–557.

Jones, W.P. and Launder, B.E. 1972 The Prediction of Laminarization with a Two-Equation Model of Turbulence, *Int. J. Heat Mass Trans.*, 15, 301–314.

Jonnavithula, S. 1992 Steady State Simulation of the Flow in a Torque Converter, *adapco Report 12–51–002.*

Kallinderis, Y. 1992 Numerical Treatment of Grid Interfaces for Viscous Flows, *J. Comp. Phys.*, 98, 129–144.

Kallinderis, Y., Khawaja, A. and McMorris, H. 1996 Hybrid Prismatic/Tetrahedral Grid Generation for Viscous Flow around Complex Geometries, *AIAA J.*, 34, 291–298.

Kim, J. 1983 The Effect of Rotation on Turbulence Structure, *Proc. 4th Symp. on Turbulent Shear Flows, Karlsruhe*, 6.14–6.19.

Kim, J., Kline, S.J. and Johnston, J.P., 1978 Investigation of Separation and Reattachment of a Turbulent Shear Layer: Flow over a Backward-Facing Step, Report No. MD–37, Thermosciences Division, Dept. of Mechanical Engineering, Stanford University.

Kristoffersen, R. and Andersson H.I. 1993 Direct Simulation of Low-Reynolds-Number Turbulent flow in a Rotating Channel, *J. Fluid Mech.*, 256, 163–197.

Lai, Y.G., Jiang, Y. and Przekwas, A. J. 1993 An Implicit Multi-Domain Approach for the Solution of Navier-Stokes Equations in Body-Fitted-Coordinate Grids, *AIAA–93–0541.*

Launder, B.E. 1989 Second-Moment Closure and Its Use in Modelling Turbulent Industrial Flows, *Int. J. Numer. Methods Fluids,* 9, 963–985.

Launder, B.E., Priddin, C.H. and Sharma, B.I. 1977 The Calculation of Turbulent Boundary Layers on Spinning and Curved Surfaces, *J. Fluids Eng.*, 102, 231–239.

Launder, B.E. and Sharma, B.I. 1974 Application of the Energy Dissipation Model of Turbulence to the Calculation of Flow near a Spinning Disc, *Lett. Heat Mass Transf.*, 1, 1112–1128.

Launder, B.E and Spalding, D.B. 1974 The Numerical Computation of Turbulent Flows, *Comp. Meth. Appl. Mech Engg.*, 3, 269–289.

Launder, B.E., Reece, G. and Rodi, W. 1973 Progress in the Development of a Reynolds-Stress Turbulence Closure, *J. Fluid Mech.*, 68, 537–566.

Launder, B.E., Tselepidakis, D.P. and Younis, B.A. 1987 A Second-Moment Closure Study of Rotation Channel Flow, *J. Fluid Mech.*, 183, 63–75.

Lien, F.S. and Leschziner, M.A. 1994 Assessment of Turbulence-Transport Models Including Non-Linear RNG Eddy-Viscosity Formulation and Second-Moment Closure for Flows over a Backward-Facing Step, *Comp. Fluids.*, 23, No. 8, 983–1004.

Löhner, R. and Parikh, P. 1988 Generation of Three-Dimensional Unstructured Grids by the Advancing-Front Method, *Int. J. Numer. Methods Fluids*, 8, 1135–1149

Lumley, J.L. 1978 Computational Modeling of Turbulent Flows, in C.S. Yih (ed.), *Advances in Applied Mechanics* 18, Academic Press, New York, 123.

Meakin, R.L. 1994 On the Spatial and Temporal Accuracy of Overset Grid Methods for Moving Body Problems, *AIAA–94–1925.*

Meakin, R.L. and Street, R.L. 1988 Simulation of Environmental Flow Problems in Geometrically Complex Domain, Part 2: A Domain-Splitting Method, *Computer. Meths. Appl. Mech. Eng.*, 68, 311–331.

Mohammadi, B. and Pironneau, O. 1994 *Analysis of the K-Epsilon Turbulence Model*, John Wiley & Sons, New York.

Moon, Y. and Liou, M.–S. 1989 Conservative Treatment of Boundary Interfaces for Overlaid Grids and Multi-Level Grid Adaptations, *AIAA–89–1980.*

Morgan, K., Peraire, J., Perio, J. and Hassan, O. 1991 The Computation of Three-Dimensional Flows Using Unstructured Grids, *Comp. Methods Appl, Mech. Eng.*, 87, 335–352.

Orszag, S.A., Yakhot, V., Flannery, W.S., Boysan, F., Choudhury, D., Maruzewski, J. and Patel, B. 1993 Renormalization Group Modeling and Turbulence Simulations, in R.M.C. So, C.G. Speziale and B.E. Launder, eds., *Near-Wall Turbulent Flows*, 1031–1047 Elsevier, Amsterdam, The Netherlands.

Part-Enander, E. and Sjogreen, B. 1994 Conservative and Non-Conservative Interpolation between Overlapping Grids for Finite Volume Solutions of Hyperbolic Problems, *Comp. Fluids*, 23, 551–574

Patankar, S. V. 1980 *Numerical Heat Transfer and Fluid Flow*, Hemispere, Washington D.C.

Patel, V.C., Rodi, W. and Scheuerer, G. 1985 Turbulence Models for Near-Wall and Low Reynolds Number Flows, *AIAA J.*, 23, 1308–1319.

Perng, C.Y. and Street, R.L. 1991 A Coupled Multigrid-Domain-Splitting Technique for Simulating Incompressible Flow in Geometrically Complex Domains, *Int. J. Numer. Meths. Fluids,* 13, 269–286.

Rai, M.M. 1984 A Conservative Treatment of Zonal Boundary for Euler Equation Calculations, *AIAA–84–0164.*

Rai, M.M. 1985 A Implicit, Conservative, Zonal-Boundary Scheme for Euler Equation Calculations, *AIAA–85–0488.*

Rodrigue, G. and Shah, S. 1989 Pseudo-Boundary Conditions to Accelerate Parallel Schwarz Methods, G. Carey eds., *Parallel Supercomputing Methods, Algorithms and Applications*, Wiley, Chichester, England.

Sani, R.L. and Gresho, P.M. 1994 Resume and Remarks on the Open Boundary Condition Mini Symposium, *Int. J. Numer. Meths. Fluids*, 18, 983–1008.

Schlichting, H 1979 *Boundary-Layer Theory,* McGraw–Hill, Inc., New York.

Shih, T., Liou, W.W., Shabbir, A., Yang, Z. and Zhu, J. 1995 A New K-ε Eddy Viscosity Model for High Reynolds Number Turbulent Flows, *Comp. Fluids.*, 24, No. 3, 227–238.

Shimomura, Y, 1993 Turbulence Modeling Suggested by System Rotation, in R.M.C. So, C.G. Speziale and B.E. Launder (eds.), *Near-Wall Turbulence,*, 115–123, Elsevier, Amsterdam, The Netherlands.

Shyy, W. 1987 Effects of Open Boundary Condition on Incompressible Navier-Stokes Flow Computation: Numerical Experiments, *Numer. Heat Transf.*, 12, 157–178.

Shyy, W. *1994 Computational Modeling for Fluid Flow and Interfacial* Transport, Elsevier, Amsterdam, The Nertherlands.

Shyy, W., Liu, J. and Wright, J. 1994 Pressure-Based Viscous Flow Computation Using Multiblock Overlapped Curvilinear Grid, *Numer. Heat Transf.*, 25, 39–59.

Shyy, W., Thakur, S. and Wright, J. 1992 Second-Order Upwind and Central Difference Schemes for Recirculating Flow Computation., *AIAA J.*, 30, 923–932.

Shyy, W., Tong, S.S. and Correa, S.M. 1985 Numerical Recirculating Flow Calculation Using a Body-Fitted Coordinate System., *Numer. Heat Transf.*, 8. 99–113.

Shyy, W., Pang, Y., Hunter, G.B., Wei, D.Y. and Chen, M.–H. 1992 Modeling Turbulent Transport and Solidification during Continuous Ingot Casting, *Int. J. Heat Mass Transf.*, 35, 1229–1245.

Shyy, W. and Vu, T.C. 1993 Modeling and Computation of Flow in a Passage with 360 Degree Turning and Multiple Airfoils, *J. Fluids Eng.*, 115, 103–108.

Speziale, C.G. 1995 A Review of Reynolds Stress Models for Turbulent Shear Flows, *NASA CR–195054.*

Speziale, C.G and Thangam, S. 1992 Analysis of a RNG Based Turbulence Model for Separated Flows, *Int. J. Engng. Sci.*, 30, 1379–1388.

Steger, J.L. 1991 Thoughts on the Chimera Method of Simulation of Three-Dimensional Viscous Flow, in Proceedings, *Computational Fluid Dymnamics Symposium on Aeropropulsion*, Cleveland, Ohio, *NASA CP–3078*, 1–10.

Strikwerda, J.C. and Scarbnick, C.D. 1993 A Domain Decomposition Method for Incompressible Viscous Flow, *SIAM J. Sci. Comput.*, 14, No. 1, 49–67.

Thakur, S., Wright, J., Shyy, W., Liu, J., Ouyang, H., and Vu, T. 1995 Development of Pressure-Based Composite Multigrid Method for Complex Fluid Flows, to appear *in Progress in Aerospace Sciences.*

Tritton, D.J. 1992 Stabilization and Destabilization of Turbulent Shear Flow in a Rotating Fluid, *J. Fluid Mech.*, 241, 503–523.

Tu, J.Y. and Fuch, L. 1992 Overlapping Grids and Multigrid Methods for Three-Dimensional Unsteady Flow Calculations in IC Engines, *Int. J. Numer. Meths. Fluids*, 15, 693–714.

Tucker, P.K. and Shyy, W. 1993 A Numerical Analysis of Supersonic Flow over an Axisymmetric Afterbody, *AIAA Paper* No. 93–2347.

Viegas, J.R., Rubesin, M.W. and Horstman, C.C. 1985 On the Use of Wall Functions as Boundary Conditions for Two-Dimensional Separated Compressible Flows, *AIAA Paper* 85–0180.

Vu, T.C. and Shyy, W. 1988 Navier-Stokes Computation of Radial Inflow Turbine Distributor, *J. Fluids Eng.*, 110, 29–32.

Vu, T.C. and Shyy, W. 1990 Navier-Stokes Flow Analysis for Hydraulic Turbine Draft Tubes, *J. Fluid Eng.*, 112, 199–204.

Wang, Z.J., Buning, P. and Benek, J. 1995 Critical Evaluation of Conservative and Non-Conservative Interface Treatment for Chimera Grids, *AIAA–95–0077.*

Warfield, M.J. and Lakshminarayana, B. 1987 Computation of Rotating Turbulent Flow with an Algebraic Reynolds Stress Model, *AIAA J.*, 25, 957–964.

Wilcox, D.C. 1993 *Turbulence Modeling for CFD*, DCW Industries, Inc., La Canada, CA.

Wright, J. and Shyy, W. 1993 A Pressure-Based Composite Grid Method for the Incompressible Navier–Stokes Equations, *J. Comp. Phys.*, 107, 225–238.

Wright, J. and Shyy, W. 1996 Numerical Simulation of Unsteady Convective Intrusions in a Thermohaline Stratification, *Int. J. Heat Mass Transfer*, 37, 1183–1201.

Yakhot, V. and Orszag, S.A. 1986 Renormalization Group Analysis of Turbulence, I: Basic Theory, *J. Sci. Comput.*, 1, 3–51.

Yakhot, V., Orszag, S.A., Thangam, S., Gatski, T.B. and Speziale, C.G. 1992 Development of Turbulence Models for Shear Flows by a Double Expansion Technique, *Phys. Fluids.* A, 4, No. 7, 1510–1520.

Yakhot, V. and Smith, L.M. 1992 The Renormalization Group, the ε-Expansion and Derivation of Turbulence Models, *J. Sci. Comput.*, 3.

Younnis. B.A. 1993 Prediction of Turbulent Flows in Rotating Rectangular Ducts, *J. Fluids Eng.*, 115, 646–652.

Yung, C., Keith, JR.T.G. and De Witt, K.J. 1989 Numerical Simulation of Axisymmetric Turbulent Flow in Combustors and Diffusers, *Int. J. Numer. Meths. Fluids*, 9, 167–183.

BIOGRAPHICAL SKETCH

Jian Liu was born on May 28, 1964 in Dalian, Liaoning province, P.R. China. He earned his bachelor's degree and master's degree in applied mechanics from Beijing University of Aeronautics & Astronautics, Beijing, China, in 1985 and 1988, respectively. During the period of studying for his master's degree, he worked in the fields of experimental fluid mechanics and aeroacoustics. From 1988 to 1990, he worked as a research associate in the Institute of Engineering Mechanics, Dalian University of Technology, Dalian, China. Since fall 1990, he has been pursuing a Ph.D degree in the Department of Aerospace Engineering, Mechanics and Engineering Science, University of Florida, with specialization in computational fluid mechanics.

I certify that I have read this study and that in my opinion it conforms to acceptable standards of scholarly presentation and is fully adequate, in scope and quality, as a dissertation for the degree of Doctor of Philosophy.

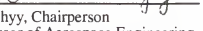

Wei Shyy, Chairperson
Professor of Aerospace Engineering,
Mechanics and Engineering Science

I certify that I have read this study and that in my opinion it conforms to acceptable standards of scholarly presentation and is fully adequate, in scope and quality, as a dissertation for the degree of Doctor of Philosophy.

Chen-Chi Hsu
Professor of Aerospace Engineering,
Mechanics and Engineering Science

I certify that I have read this study and that in my opinion it conforms to acceptable standards of scholarly presentation and is fully adequate, in scope and quality, as a dissertation for the degree of Doctor of Philosophy.

Ulrich H. Kurzweg
Professor of Aerospace Engineering,
Mechanics and Engineering Science

I certify that I have read this study and that in my opinion it conforms to acceptable standards of scholarly presentation and is fully adequate, in scope and quality, as a dissertation for the degree of Doctor of Philosophy.

Bernard M. Leadon
Professor of Aerospace Engineering,
Mechanics and Engineering Science

I certify that I have read this study and that in my opinion it conforms to acceptable standards of scholarly presentation and is fully adequate, in scope and quality, as a dissertation for the degree of Doctor of Philosophy.

Kermit N. Sigmon
Associate Professor of Mathematics

This dissertation was submitted to the Graduate Faculty of the College of Engineering and to the Graduate School and was accepted as partial fulfillment of the requirements for the degree of Doctor of Philosophy.

May 1996

Winfred M. Phillips
Dean, College of Engineering

Karen A. Holbrook
Dean, Graduate School